2012-03-06

Optical and Mass Spectrometric Studies of a Helium Dielectric-Barrier Atmospheric-Pressure Plasma Jet Used as an Ambient Desorption Ionization Source

Matthew Spencer Heywood
Brigham Young University - Provo

Optical and Mass Spectrometric Studies of a Helium Dielectric-Barrier Atmospheric-Pressure Plasma Jet Used as an Ambient Desorption Ionization Source

Matthew S. Heywood

A dissertation submitted to the faculty of
Brigham Young University
in partial fulfillment of the requirements for the degree of

Doctor of Philosophy

Paul B. Farnsworth
Jaron C. Hansen
Milton L. Lee
Paul B. Savage
Adam T. Woolley

Department of Chemistry and Biochemistry

Brigham Young University

April 2012

ABSTRACT

Optical and Mass Spectrometric Studies of a Helium Dielectric-Barrier Atmospheric-Pressure

Plasma Jet Used as an Ambient Desorption Ionization Source

Matthew S. Heywood
Department of Chemistry and Biochemistry, BYU
Doctor of Philosophy

Recently there has been a surge in the field of mass spectrometry centered around the concept of rapid analysis of target analytes with minimal or no sample preparation. The target analyte undergoes desorption from its surface of origin and is subsequently ionized under ambient conditions. The technique is termed ambient desorption/ionization mass spectrometry (ADI-MS). Since the introduction of ADI-MS in 2004, there has been an explosion of research based around the development of novel ambient desorption/ionization (ADI) sources with the capability of desorbing and ionizing a variety of target analytes from various sampling surfaces. One type of ADI source uses the properties of an electrical discharge, typically a helium gas plasma, for desorption and ionization. For electrical-discharge-based sources, ionization is the result of an atmospheric pressure chemical ionization (APCI) process. The initiation of the APCI process it generally attributed to the Penning ionization of atmospheric nitrogen (N_2) by highly energetic helium metastable species (He_m). In this work, I describe the direct imaging of the densities of helium metastable atoms in atmospheric pressure plasma jet (APPJ) of a helium-based dielectric-barrier discharge (DBD) using collisionally-assisted laser-induced fluorescence. Axial He_m distributions are compared to the emission of excited helium (He^*) and nitrogen ion (N_2^{+*}) species in the plasma. A correlation is found between He_m densities and the performance of the ionization source in ADI-MS. Fluorescence images also show that He_m densities increase substantially when a glass slide is placed 10 mm from the discharge capillary in a geometry typical for desorption/ionization experiments. Advantage is taken of the time-varying nature of the plasma to produce axial profiles of temporally and spectrally resolved fluorescence images of He_m atoms and ground state nitrogen ions in the plasma jet. The axial distribution and similarities in the temporal behavior of the helium metastable and ground state nitrogen ion species give strong evidence that nitrogen ion species are created via Penning ionization by helium metastable atoms. Although axial distributions of He^*,N_2^{+*}, and N_2^* emission support the fluorescence data, temporally-resolved emission measurements show that emission from key plasma species is almost entirely the result of excitation by a temporal energy wave. The effect that hydrogen (H_2) has on the helium metastable atom densities is also presented. The addition of hydrogen to the discharge gas severely quenches the metastable state, leaving it virtually undetectable. The addition of 0.9% H_2 to the helium in the source provides an order of magnitude increase in ADI-MS signal for target analytes despite the quenching of the He_m population.

Keywords: Helium Dielectric-Barrier Discharge, Atmospheric Pressure Plasma Jet, Ambient Desorption/Ionization Mass Spectrometry, Helium Metastable Imaging

ACKNOWLEDGEMENTS

This dissertation represents the dedication, support, and sacrifice of many people. To my advisor, Dr. Paul Farnsworth, I am grateful for the opportunity to work in his research group. His example of patience and scientific excellence will always be a model to follow. I thank my many friends and colleagues from Dr. Farnsworth's group for their encouragement and support. I am thankful to my family for their support, especially that of my parents, whose prayers in my behalf have been a force for good in my life. I am most grateful to my wife, who has been a constant source of strength and encouragement. Thank you, Marin, for your endless sacrifice and support. I dedicate this dissertation to you and to our beautiful children, Emma, Spencer, and Lindsay.

Table of Contents

List of Tables

List of Figures

1 Introduction

1.1 Ambient Desorption Ionization Mass Spectrometry

Recently there has been a surge in the field of mass spectrometry centered around the concept of rapid analysis of target analytes with minimal or no sample preparation. Analysis begins with desorption of target analyte from its surface of origin, followed by ionization. The analyte desorption and (for most techniques) ionization take place outside any compartment of the mass spectrometer, under ambient conditions. The ionized analyte is then carried to the inlet of the mass spectrometer to undergo mass analysis. Analyte desorption and ionization is accomplished by using an ambient desorption/ionization (ADI) source and the technique is termed ambient desorption/ionization mass spectrometry (ADI-MS). Along with ambient ionization mass spectrometry, ADI-MS is a subset of ambient mass spectrometry.

1.1.1 Background

The explosion of research in the field of mass spectrometry known as ADI-MS was brought about by the introduction of two different ADI sources to the scientific community. The desorption electrospray ionization (DESI) source was introduced first in 2004 by Takats et al. as a solvent-based ADI source, which essentially utilized a pneumatically assisted ESI source by pointing it not at the orifice of the mass spectrometer, but at the sample which was placed just outside the orifice of the mass spectrometer. Desorption and ionization by the new source allowed for ambient analysis of various compounds, generating spectra similar to those observed when using electrospray ionization.[1]

Shortly after the emergence of DESI, the Direct Analysis in Real Time or DART, an electrical discharge type ionization source, was introduced. First published by Cody et al., the

DART showed a great versatility of application using the hot gas from an electrical discharge to generate mass spectra of hundreds of chemicals from a variety of surfaces under ambient conditions.[2]

Since their introduction, DESI and DART sources have been commercialized, and their initial reports have seen over 1000 citations in the literature combined. Furthermore, following these publications, more than 30 new ionization sources have been reported with the capability of detecting analytes under ambient conditions.[3, 4] The field has become muddled with variants, which are given new names and acronyms. Sometimes, new names are given to already existing techniques to make them more marketable or to suggest novelty. Many authors have called for a revision in nomenclature,[3, 5-8] and a few have given suggestions to simplify the "acronym zoo", although they do not agree on how this is to be done.[5-7] A simplification in nomenclature seems impossible as many researchers feel their sources are significantly different from other variants. One way to distinguish and combine techniques would be to classify them based on the fundamental processes by which each source functions. Then, sources that are fundamentally the same could be combined into one technique, having one name and one acronym. Although some of the more recent publications have looked into the fundamental processes that cause desorption and ionization, the bulk of the literature focuses on the analytical merit and application of these sources.

1.1.2 Accomplishments

ADI sources are clearly versatile in their application as they can be used to detect a wide variety of compounds from various surfaces. Examples of target analytes in the literature include, pharmaceutical compounds,[1, 2, 9-14] illicit drugs and drug metabolites,[2, 15-23] explosives and chemical warfare agents,[10, 24-29] plants and natural products,[30-35] food compounds,[36-41] food

contaminants and agricultural chemicals,[42-46] and biomolecules.[47-51] Sample surfaces include concrete, metal, glass, paper, plastic, textiles, food, skin,[2, 24] TLC plates,[2, 52-55] and even bulk liquids.[2, 54, 55]

The ability to rapidly analyze multiple samples has been demonstrated, typically in the detection of active ingredients in pharmaceutical tablets. Sampling rates have been reported at speeds as fast as 10 samples/s.[11, 21] Detection with portable mass spectrometers has also been demonstrated with several ADI sources.[41, 56] Another significant and exciting application of ADI-MS is imaging mass spectrometry, where ADI-MS is used to chemically image biological tissue samples.[8, 19, 57-60]

1.2 ADI Sources

The examples above are the result of a variety of ADI sources that have been introduced in the scientific literature. ADI sources are accompanied by several other types of ambient ionization sources in the inclusive field of ambient mass spectrometry. The existing sources in the field of ambient mass spectrometry can be categorized in several ways, particularly by desorption or ionization mechanism.[6, 7, 61] However, it is convenient to first separate ambient ionization sources into three categories, direct ionization, direct desorption/ionization, and two-step desorption/ionization.[4]

Direct ionization sources are ambient ionization sources with no desorption or sampling step required for analysis. Although direct ionization sources, like remote analyte sampling, transport, and ionization relay (RASTIR); and paper spray ionization (PSI) provide interesting and even exciting research of their own, I will exclude them from the immediate discussion, allowing for focus on ADI sources.

Sources that fall under the direct desorption and ionization category, are ADI sources that accomplish both desorption and ionization. Those techniques that have a separate desorption or sample step followed by ionization can be classified as two-step ionization techniques. Although some techniques require sample preparation, they fall under the umbrella of ambient ionization mass spectrometry. Although two-step desorption/ionization techniques have novel aspects to them, they are typically combinations and variations of direct desorption/ionization ADI sources, and their corresponding desorption and ionization mechanisms are based on the fundamental mechanisms of their simpler versions. My interest, with a few exceptions, is in those techniques that accomplish both desorption and ionization using a single ADI source. This simplifies research with a focus on fundamental processes. I will further separate ADI sources of interest into two categories, solvent-based and electrical discharge-based ionization sources. There are several sources that use laser radiation. However, most are coupled to solvent- or plasma-based techniques in a two-step ionization process.

1.2.1 Solvent-Based Sources

Solvent-based ambient ionization sources are variations of electrospray ionization. Most sources can be produced by making slight alterations to commercial electrospray sources. As a result, solvent-based ADI sources generate ions by an electrospray mechanism, and the resultant mass spectra are comparable to ESI spectra. Like ESI, solvent-based methods have the advantage of being able to ionize analytes with a wide range of masses. ADI-MS analysis of bovine serum albumin, among other proteins, with a mass of 66 kDa has been accomplished with DESI.[50] Conversely, sensitivity in detecting low molecular weight molecules is decreased by a

Direct Ionization	
Direct Electrospray Probe	DEP
Probe Electrospray Ionization	PESI
Paper Spray Ionization	PSI
Droplet Electrospray Ionization	Droplet ESI
Field Induced Droplet Ionization	FIDI
Ultrasound Ionization	USI
Remote Analyte Sampling, Transport, and Ionization Relay	RASTIR
Direct Desorption/Ionization	
Desorption Electrospray Ionization	**DESI**
Direct Analysis in Real Time	**DART**
Electrode-assisted Desorption Electrospray Ionization	EADESI
Easy Ambient Sonic Spray Ionization	EASI
Desorption Atmospheric Pressure Chemical Ionization	**DAPCI**
Dielectric Barrier Discharge Ionization	**DBDI**
Low Temperature Plasma	**LTP**
Plasma-assisted Desorption Ionization	**PADI**
Atmospheric Glow Discharge Ionization	APGDI
Desorption Corona Beam Ionization	**DCBI**
Laser Spray Ionization	LSI
Flowing Atmospheric Pressure Afterglow	**FAPA**
Atmospheric Pressure Thermal Desorption Ionization	APTDI
Two-Step Desorption and Ionization	
Gas Chromatography Electrospray Ionization	GC-ESI
Secondary Electrospray Ionization	SESI
Fused Droplet Electrospray Ionization	FD-ESI
Extractive Electrospray Ionization	EESI
Liquid Surface Penning Ionization	LPI
Jet Desorption Electrospray Ionization	JeDI
Atmospheric Pressure Penning Ionization	APPeI
Electrospray Laser Desorption Ionization	ELDI
Matrix-assisted Laser Desorption Electrospray Ionization	MALDESI
Laser Ablation Electrospray Ionization	AESI
Infrared Laser-assisted Desorption Electrospray Ionization	IR-LADESI
Laser Electrospray Mass Spectrometry	LEMS
Laser Desorption Spray Post-Ionization	LDSPI
Laser-Induced Acoustic Desorption Electrospray Ionization	LIAD-ESI
Laser Desorption/Atmospheric Pressure Chemical Ionization	LD-APCI
Laser Diode Thermal Desorption	LDTD
Electrospray-Assisted Pyrolysis Ionization	ESA-Py
Atmospheric Pressure Thermal Desorption/Electrospray Ionization	AP-TD/ESI
Thermal Desorption-Based Ambient Mass Spectrometry	TDAMS
Atmospheric Pressure Solids Analysis Probe	ASAP
Desorption Atmospheric Pressure Photoionization	DAPPI
Laser-Ablation Flowing Atmospheric Pressure Afterglow	LA-FAPA
Neutral Desorption Extractive Electrospray Ionization	ND-EESI
Liquid Micro-Junction Surface Sampling Probe/Electrospray Ionization	LMJ-SSP/ESI
Desorption Electrospray Metastable-Induced Ionization	DEMI
Surface Activated Chemical Ionization	SACI
Single Particle Aerosol Mass Spectrometry	SPAMS

Figure 1.1: Summary of ambient ionization techniques. ADI sources of interest for this dissertation are highlighted in red.

low signal-to-noise because of a high background due to charged solvent. Regardless, solvent-based methods for ADI-MS are very popular because of their versatility in detecting a variety of compounds with a large range of molecular weights and because of their similarities to ESI.

1.2.1.1 DESI

DESI remains the most widely used and published solvent-based ADI source. The versatility and application of this ADI technique has been adequately summarized in several reviews.[3, 7, 62] Despite its extensive use in a variety of applications, DESI remains on the cutting edge of ADI-MS with improvements made in detection of saturated hydrocarbons, cholesterols, anabolic steroids, cis-diols, and counterfeit antimalarial drugs using a technique called Reactive DESI.[18, 63-66] DESI is also the most advanced source for ADI-MS chemical imaging. Images are generated by rastering a sample underneath the DESI spray, and collecting a mass spectrum for each position. Imaging with DESI-MS has been shown to have a lateral imaging resolution of less than 200 µm.[57] Applications have included the mapping of target analyte distributions in fingerprints,[67]and biological tissues.[19, 57, 58, 64]

DESI related research has also included fundamental studies on the solvent-based desorption mechanism. A single-stage droplet pick-up mechanism was initially suggested,[68] however, current literature favors a more recently-proposed splash droplet pick-up mechanism where the surface is first wetted by the spray solvent, creating a thin film wherein the analyte is dissolved. It is proposed that subsequent droplets from the spray splash into the thin film, generating droplets containing analyte into the air. These secondary droplets can be progeny droplets or larger droplets that then undergo evaporation and fission processes to generate progeny droplets.[69, 70] Work by Wood et al. cast a large shadow of doubt on this mechanism, showing a persistent analyte signal long after analyte had been removed from the splash region.

Further evidence against the splash droplet pick-up mechanism was shown when signal was obtained after placing a splash guard between the DESI needle tip and the MS inlet. Experiments also indicated that ions are produced at the ends of spray-generated solvent rivulets.[71] Despite the challenges that Wood's findings pose to the prevailing DESI models, they have been largely ignored in the literature, and additional research is needed to confirm either mechanism.

1.2.1.2 Other Solvent-Based ADI Sources

Following the report of DESI, over a half dozen new electrospray-based desorption ionization sources were introduced in the scientific literature in only a few years. There are two ADI sources: desorption sonic spray ionization (DeSSI),[72] later termed easy ambient sonic spray ionization (EASI),[73] and electrode assisted desorption electrospray ionization (EADESI),[74] that are variants of DESI, using ESI-like sources for both desorption and ionization. Most solvent-based ADI sources use electrospray as an ionization source, subsequent to a desorption or sampling step. A number of solvent-based two-step ionization sources are included in Figure 1.1 for reference.

1.2.2 Electrical Discharge-Based Sources

1.2.2.1 Background

The popularity of electrical discharges as ADI sources began with the introduction of the DART source. However, other corona-based electrical discharge sources had been used previously and were being used as ionization sources at the time that DART was introduced.[2, 24] Unlike solvent-based sources, electrical discharge ionization sources are limited in their ability to detect compounds with a wide range of molecular weights. Compounds with molecular weights

<1000 Da are typically desorbed and ionized.[23] This is most likely the result of the nonvolatile nature of larger molecular weight compounds. An increase in temperature can improve volatility to a point, after which, molecules undergo thermal decomposition rather than desorption. Despite the limit in detectable mass range compared to solvent-based sources, discharge sources have inherently cleaner background spectra. Spectra typically consist of the protonated molecular ion $[M+H]^+$ peak with little or no fragmentation. These simple spectra are said to be APCI-like and the ionization processes for these sources are reportedly related to APCI processes. The mechanisms responsible for ionization by electrical discharge also allow for the detection of molecules with a large range of polarities.[4]

1.2.2.2 Electrical Discharge ADI Sources of Interest

1.2.2.2.1 Desorption Atmospheric Pressure Chemical Ionization (DAPCI)

The DAPCI is one of the earliest electrical discharge sources, having been introduced slightly ahead of DART by being slipped into a DESI paper in the beginning of 2005.[24] The new source is said to be a variation on DESI in which the solvent needle is replaced by a tapered stainless steel pin. A high voltage of 3-5 kV DC is applied to the pin forming a corona discharge. Gaseous solvent vapors, which are added to the annular gas flow, are ionized by the discharge, forming a beam of gaseous excited molecules. Toluene and methanol have been used as well as acetic acid, trifluoroacetic acid or dichloromethane. Resulting desorption and ionization mass spectra obtained by this technique are compared to DESI ADI-MS spectra, and it has been determined that the resulting analyte ions are the result of electron or proton transfer. No anion adduction was seen when first compared to DESI. The desorption mechanism for this source is attributed to a buildup of surface charge and the subsequent ionization and ion transport to the mass spectrometer.

Since the rather informal introduction of the DAPCI, it has been used to detect nitro-aromatic, and peroxide explosive compounds,[25, 28] and tea products.[30] Nitrogen is typically the carrier gas with gaseous vapors being added in from various solvents including, acetonitrile, water, and ammonia.[25, 28, 30]

Other two-step corona discharge-based ADI sources have been used and documented. They include the atmospheric pressure surface analysis probe (ASAP), and laser diode thermal desorption (LDTD) which uses a corona discharge for ionization. Like DAPCI, these ionization techniques rely on corona discharge APCI processes for ionization.

1.2.2.2.2 Direct Corona Beam Ionization (DCBI)

Similar to DAPCI and ASAP, the DCBI uses a low current and high DC voltage. Other than this and the usage of corona in the name, there are few similarities between DCBI and other corona discharge sources. Although certain features of the DCBI seem unique, it is very similar to the DART and FAPA sources.

In the DCBI source, a helium discharge is formed between a high voltage needle and a plate counter electrode. The discharge protrudes 8-12 mm from an orifice in the counter electrode. The protrusion of the discharge from the orifice is assisted by the 1 L/min flow rate of helium applied to the discharge. The thin plasma beam is oriented vertically and allowed to come in contact with the sample in front of the mass spectrometer inlet. The helium gas is heated prior to plasma formation. Temperatures up to 450^{o}C were used for thermal desorption of pesticides, veterinary additives, OTC drugs and explosives. Compounds over 600 Da were not observed. The lack of high-mass compounds was attributed to the non-volatile nature of larger compounds, which were more likely to undergo decomposition rather than desorption at high temperatures.[10]

1.2.2.2.3 Direct Analysis in Real Time (DART)

The DART source consists of several chambers where alterations can be made to the plasma/gas stream. Helium or nitrogen is used to generate a plasma in the discharge chamber between a high-voltage needle (1-5 kV) and a perforated electrode, creating ions, electrons, and atomic or molecular species. Shelley et al. have classified the DART plasma as a corona-glow transition type discharge with a temperature of about 55^{o}C.[75] The ions generated in the plasma can be removed in the second chamber by a second perforated electrode. In the third chamber, the gas is optionally heated up to 500^{o}C. Finally, the gas passes through a third grid electrode that repels ions and helps prevent ion-ion recombination. The resulting gas stream is directed to the orifice of the mass spectrometer (0^{o} angle) or at a sampling surface (45^{o} angle). The orientation of the source with respect to the analyte and MS inlet is not critical to analyte detection. Because ions have been removed from the gas stream, and because there is no plasma surface interaction, desorption is most likely due to thermal processes. Ionization by DART is said to be initiated by Penning ionization via excited nitrogen or helium species. Ionization of many molecules is not favored when using nitrogen due to the low energy of excited nitrogen. The use of helium gas, however, produces energetic helium metastable atoms, which are said to initiate the production of protonated water clusters. These water clusters, are then responsible for the protonation of the desorbed analyte. The formation of water clusters is confirmed by their appearance in background mass spectra.[2, 75] Although proton addition is the major ionization mechanism, it can be hindered by solvent matrix affects.[76] Detection in negative ion mode has also been studied and results suggest electron capture, dissociative electron capture, proton transfer, and anion attachment as possible ionization mechanisms.[77]

The DART is by far the most well known plasma-based ADI source seeing, on average, 16 publications per year between 2005 and 2010.[3] Most of these publications focus on the application of DART as an analytical tool for detection of various compounds.[2, 9, 14-16, 20, 22, 33, 34, 36-38, 42, 78-86] Most impressive was the initial introduction of DART in 2005 with the detection of a variety of compounds from a variety of surfaces with no sample pretreatment.[2] Its popularity has inspired the creation of several new ADI sources.

1.2.2.2.4 Flowing Atmospheric Pressure Afterglow (FAPA)

The FAPA was introduced to the field in 2008 as an ambient version of glow discharge mass spectrometry, then termed the flowing afterglow atmospheric pressure glow discharge (FA-APGD).[87] Its construction consists of a 1.5-mm-diameter tungsten pin and brass plate with a 1-mm-diameter orifice, housed in a Teflon or ceramic discharge chamber. Helium, at flow rates from 1 -1.5 L/min, is used as the discharge gas. The FAPA is typically operated at 500 V and 25 mA with a flow rate of 0.8 L/min. The FAPA has been used to detect a variety of polar and nonpolar compounds,[75, 87-89] and has been used with laser ablation for sample depth profiling and imaging mass spectrometry,[90] and for elemental analysis.[91]

The FAPA seems very much like the DART. However, in order to distinguish the FAPA from the DART, Shelley et al. did a comparison study of DART and FAPA, characterizing the electrical, optical and mass spectrometric properties of each source. In their research, the FAPA was run at "DART-like" settings, without a heat tube or grid electrode. The FAPA was found to produce a much hotter plasma (~235^{o}C) than the DART and the discharge was classified as an glow-arc transition type discharge. Differences in the background mass spectra were also noted.[75]

The FAPA is said to have an advantage over corona discharge-based ionization sources due to higher currents, giving it the ability to generate a larger variety of reagent ions. Because of this effect, background mass spectra for FAPA contain not only protonated water peaks, typical of an APCI mechanism, but also NO^+ peaks along with H_2O^+ and O_2^+ peaks.[75, 87, 88] The generation of various oxygen species poses a problem for FAPA, however, due to the addition of oxygen to aromatic hydrocarbon compounds. This compromises the detection of various organics, like explosives, which contain aromatic hydrocarbons. To solve this problem, the FAPA has been redesigned to have a pin-to-capillary configuration. The addition of a stainless-steel capillary distances the analyte from the discharge region and prohibits the mixing of atmospheric oxygen with the afterglow region of the discharge, simplifying the background spectra and eliminating unwanted oxidation of analyte.[92]

1.2.2.2.5 Plasma Assisted Desorption Ionization (PADI)

Although the PADI source has seen only one publication, that publication is frequently cited. The source consists of a 190-mm long stainless steel wire within a ceramic tube. The needle and ceramic tube are placed coaxially within a quartz capillary (5 mm i.d.). The ceramic and quartz tubes have independent gas feeds allowing for the usage of mixed gas plasmas. The stainless-steel wire protrudes from the ceramic and quartz tubes. An rf voltage of 200-500 V is applied to the wire at a frequency of 13.56 MHz. The plasma that is generated is a "cold", nonthermal plasma that extends about 10 mm from the needle tip. The plasma was used as an ADI source for detection of pharmaceuticals, creams, and plant alkaloids. Mass spectra were compared to those obtained by DESI and were said to be cleaner, having higher sensitivity and less fragmentation for the compounds tested.[93] No significant insight was given about desorption

or ionization mechanisms. Only those mechanisms that had already been proposed for DART were included in the text.

1.2.2.2.6 Dielectric-Barrier Discharge (DBD) Sources

Although the DBDs have only recently been added to the list of discharges suitable for ADI-MS, they have long been used in the analytical world for detection of various atomic and molecular species. They have been combined with hydride generation for the detection of various atomic species,[94-96] and have been used as ionization sources for GC, HPLC, and IMS.[97-100] DBDs are popular because they are simple to construct, making them a cost effective source for excitation and ionization. Furthermore, DBDs use alternating currents at radio frequencies, making them less dangerous than DC sources.

The discharge is created between two electrodes that are separated by a dielectric material such as glass or ceramic. The dielectric material is an insulator, preventing the passing of a direct current. Therefore, alternating voltages with high electric fields are used to transport current across the barrier, into the discharge gap. The discharge is formed when the gas breakdown potential is reached. DBDs can be configured with a variety of electrode spacings and orientations, and have a range of powers, and frequencies.[101] An illustration of some configurations is shown in Figure 1.2. Although a planar configuration is more traditional, DBDs can also be formed in a ring-capillary-needle configuration. In this configuration, the high voltage is applied to the outer ring, and the discharge is formed in the capillary, grounded by the needle. One such configuration allows the flow of the carrier gas to carry the plasma out of the capillary forming a plasma jet, also known as an atmospheric pressure plasma jet (APPJ). The length of the plasma jet depends on the flow rate of the carrier gas and the dimensions of the capillary.

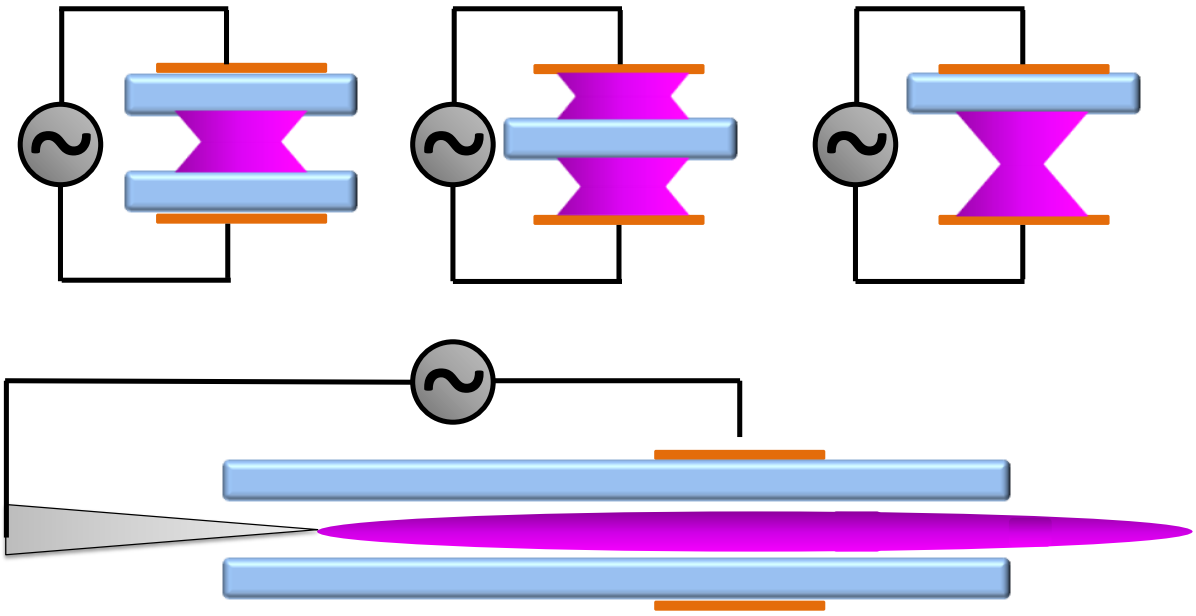

Figure 1.2: Various configurations of DBDs, including the APPJ.

The APPJ has been extensively researched, particularly by those in the field of plasma physics.[102-107] Lately, research in this field has focused on the time-dependent nature of the discharge.[107-115] This temporal dependence is the result of the alternating current of the high voltage power supply used to form the discharge. In the APPJ configuration, the time-dependent nature is observed in the form of a wave of emission termed a "plasma bullet".[108] Although the term "bullet" suggests material transport and speeds comparable to the linear velocity of the carrier gas, the hypersonic wave of emission is said to be the result of an ionization wave.[109] The wave of ionization is not necessarily the result of the high electric field generated at the electrode, but rather an induced local electric field that travels at the head of the bullet.[111] This time-dependent nature is a useful tool to aid in the understanding of plasma processes.

Although the field of plasma physics has some insight into the fundamental workings of the APPJ, physicists have not addressed its use in the field of ADI-MS. The major difference between DC and RF plasma-based ADI sources, apart from the time-dependent nature of the RF

source, is the interaction of the plasma with the analyte and the analyte surface. This interaction introduces new ideas concerning desorption and ionization processes that will be discussed later. Despite plasma interactions, users of DBD-based ADI sources also report a soft ionization technique, providing mass spectra with $[M+H]^+$ peaks and having little or no fragmentation. These results are evidence that DBD-based discharges work similarly to the DC discharges discussed above.

Of the three DBD-based ADI sources that I will discuss, two are APPJ, the low temperature plasma (LTP) and a simply constructed, unnamed APPJ, made in the Farnsworth lab. These two sources, the fundamental processes that make them useful ADI sources, and the application of the understanding of those fundamental processes to other plasma-based ADI sources has been the focus of my research over the past two years.

1.2.2.2.6.1 Dielectric-Barrier Discharge Ionization (DBDI)

The coupling of DBD-based sources to ADI-MS began, not with an APPJ, but with a DBD with a unique design. Because the plasma used for ionization was formed via a dielectric barrier, the name given the technique was dielectric-barrier discharge ionization (DBDI). Although other sources use DBDs, they are given other names. This represents another area in which nomenclature could be simplified.

The unique design of the discharge consists of a hollow stainless-steel needle electrode and a 10 x 10-mm copper sheet. The dielectric material that separates the two electrodes is a 30 x 30 x 1-mm glass plate that also serves as the sample surface. The discharge gas flows through the hollow needle electrode at flow rates of 0.05-0.2 L/min. Helium, argon, nitrogen and air have been tested as discharge gases. The needle is positioned vertically (80-90^o) above the glass plate with a distance of 5-10 mm between the needle and the glass plate. An AC voltage of 3.4-

3.5 kV is applied between the two electrodes, having a frequency of 18-25 kHz. The discharge is formed between the needle and the glass plate. The copper sheet and glass plate are placed on an x-y-z stage which allows for the positioning of the sample in the plasma. Other sampling surfaces include filter paper, plastic and TLC plates. The distance from the needle to the mass spectrometer inlet is 20-30 mm. ADI-MS using this source has been performed on various explosives and 20 different amino acids.[116, 117]

1.2.2.2.6.2 Low Temperature Plasma (LTP)

The LTP is an APPJ formed in a glass capillary (o.d. 6.35 mm and i.d. 3.75 mm) between an outer copper tape electrode and an inner grounded needle electrode. In this APPJ, the electrodes overlap axially. Voltages of 3-14.8 kV_{pp} are applied at 1.2-5 kHz. Discharge gases run at flow rates from 0.4-1.6 L/min and include helium, argon, nitrogen and air. The configuration is held together by a Teflon Swagelok T. The plasma that is produced is close to room temperature (~30^{o}C), and protrudes over a cm beyond the tip of the capillary.[54, 118]

The LTP is the most popular DBD-based ADI source in the literature. For that reason, it has been distinguished from other APPJ sources. Since it was first introduced, the LTP probe has been used for detection of a number of compounds including explosives, [27, 29], pharmaceutical active ingredients,[21] drugs of abuse in biofluids,[23] agrochemicals,[44] and food compounds.[36, 40, 41] It has also been found suitable for use with a portable mass spectrometer,[119] and hand held versions have been engineered.

Unlike many other plasma-based ADI sources, several fundamental studies have been done to further understand desorption and ionization mechanisms of the LTP. Initially, it was used in a comparative study with DART and FAPA to determine susceptibility to matrix effects. Results of that study suggest that the LTP is more susceptible to matrix effects than DART and

FAPA when the matrix has a higher proton affinity than the target analyte.[120] A significant increase in signal sensitivity has been documented for multiple compounds when a heat gun is used to aid thermal desorption.[23] The addition of heat to the sample surface is likely necessary due to the low temperature nature of the plasma and its inability to remove analyte by thermal desorption. Most recently, several spectroscopic studies have been done to show axial distributions of key reaction species in the plasma, giving insight into ionization processes in the plasma.[118, 121] The results of these studies will be reviewed in the upcoming discussion.

1.2.2.2.6.3 Atmospheric Pressure Plasma Jets (APPJ)

Many APPJ have been used in mass spectrometry and ion mobility spectrometry as ionization sources, but they do not fit the definition for ambient mass spectrometry.[99, 100, 122, 123] The studies that have been conducted on APPJ as ionization sources, however, give us insight into the fundamental ionization mechanisms by which these sources generate ions. Typically, these sources are characterized spectroscopically, by observing emission from key plasma species such as excited helium (He^*), excited nitrogen ion (N_2^{+*}), excited nitrogen (N_2^*), and excited oxygen (O^*).

My colleagues and I have constructed a DBD APPJ ADI source in our lab for the purpose of understanding the desorption and ionization mechanisms of plasma-based ADI sources. Various alterations were made with respect to capillary length, electrode spacing, applied power, carrier/discharge gas flow rate, and frequency of the applied voltage. The changes in these parameters necessitated altering the position of the DBD with respect to the sample surface and mass spectrometer inlet. The components of the DBD source were brought together by a 1/8 in. stainless steel Swagelok T that was positioned in close proximity to the sampling surface, just

outside the mass spectrometer inlet. The finalized settings and parameters will be discussed in the following chapters.

1.2.2.3 Comparison of Popular Helium-Based ADI Sources

Although it is generally accepted that electrical discharge-based ADI sources work by thermal desorption and an APCI mechanism, each discharge is formed by a unique set of parameters. Below is a table comparing the APPJ constructed in the Farnsworth lab to the He-based ADI sources that are most prevalent in the literature. In the case of the FAPA, only the pin-to-capillary configuration is considered. The table shows that a range of powers, voltages and flow rates can be selected for DC discharges. Despite the differences in discharge settings, the DART and FAPA share a commonality in that both produce a hot gas of excited species that is responsible for desorption and ionization. For these two sources, there is no plasma-sample interaction. The absence of a visible plasma also makes it difficult to obtain spectroscopic measurements. Furthermore, the DART and FAPA sources are made from parts that require special machining. The appeal of the APPJ arises because it is simple and inexpensive to construct. Also, the protruding jet is convenient when performing spectroscopic experiments. The APPJ presented in this work is similar to the LTP. The LTP is also a DBD APPJ, therefore, fundamental studies of the APPJ should also provide insight into the desorption and ionization processes of the LTP.

Table 1.1: *Operation parameters for the DART, FAPA, LTP and APPJ.*

	DART [2,75]	**FAPA** [75, 95]	**LTP** [54, 118]	**APPJ**
Power (W)	-	3 - 20	3 - 14.8	10 - 35
Discharge Type	DC	DC	AC, 1 - 5 kHz	AC, 325 - 350 kHz
Voltage (kV)	1 - 5	0.5	2.5 - 14.8	6 - 8
Current (mA)	~ 3	25	-	-
Gas Flow Rate (L/min)	1	0.1 - 1.5	0.4 - 1.6	0.9 - 2
Gas Temperature (°C)	55 – 500	235	~ 30	-
Plasma-Surface Interaction	No	No	Yes	Yes

1.3 Fundamental Studies of a Helium-Based Dielectric-Barrier Discharge Atmospheric-Pressure Plasma Jet Used as an Ambient Desorption/Ionization Source

A great variety of ADI sources continue to be introduced to the analytical field of ambient mass spectrometry. However, it is important that, after researchers have created every version of an ADI source, a decision can be made as to which sources are suitable for the future of ambient mass spectrometry. It is also important that ADI sources are categorized, organized, and named without further adding to the "acronym zoo" that has already been created. Most importantly, researchers must continue to compare ADI sources with a goal for improvement in ADI performance. Comparison studies are one way to simplify the field by combining like techniques, and comparing analytical performance of fundamentally different techniques. Multiple studies have been published comparing DART and DESI;[13, 16, 45, 56, 124] DART and DAPCI;[13, 35] DART and FAPA;[125] DART, FAPA, and LTP;[120] and LTP, ESSI, and DAPCI.[6] Although these studies have only been accomplished for select analytes, their results point out the complementary nature of each technique.

Another way to make improvements in the field of ambient mass spectrometry is by having a fundamental understanding of desorption and ionization processes. Understanding fundamental processes helps us to simplify the field by combining like sources, but also allows us to make improvements to the field. Fundamental research of ADI processes has been taking place in the Farnsworth lab over the past five years, with studies being done with DESI, and now APPJ as ambient ionization sources. The work described here is the result of two years of study of fundamental ionization processes of a He-based DBD APPJ used as an ADI source for ADI-MS.

1.3.1 Fundamental Processes of Plasma-Based ADI Sources

1.3.1.1 Desorption

The desorption mechanism for all electrical discharge-based sources is thought to rely mainly on thermal processes. Several studies show an improvement in ADI signal by increasing the carrier gas temperature, or by externally heating the analyte surface.[2, 10, 23] This is most likely the only mechanism for desorption for sources like DART, and in the new FAPA design, where the analyte is physically separated from the discharge. For those sources where the plasma comes in contact with the analyte surface, other mechanisms can be considered, including electron, ion, and metastable impact as well as surface charge build up.[24, 116]

1.3.1.2 Ionization

For all of the above discharge-based ADI sources, except DAPCI, helium is the carrier and discharge gas of choice. Although some sources are versatile and can be used with argon, nitrogen, or even air, helium is preferred because of increased analyte signal and reduced fragmentation.[2, 54, 87, 88, 117] I will, therefore, focus my discussion on helium-based ADI sources and the ionization processes associated with them. My current work is also limited to positive ion detection, specifically, proton addition and the formation of the $[M+H]^+$ complex. However, an understanding of the formation of negative ions is important in understanding the overall ambient ionization process and how it relates to the APCI mechanism. Studies of negative ion formation will be the focus of future work.

It is generally accepted that the $[M+H]^+$ mass spectra typically seen with He-based ADI sources are the result of proton addition from protonated water clusters. Evidence of these species in background spectra are reported in several studies.[2, 75, 87, 88] How the protonated water clusters are formed is more of a debate. The initiation of the ionization process is generally

attributed to the helium metastable species (He_m) in the $^3S_1$ and $^1S_0$ states with internal energies of 19.82 and 20.61 eV, respectively. Atoms with these internal energies are capable of ionizing most analytes (A) via Penning ionization.

$$He_m + A \rightarrow He + A^+ + e^- \quad 1.1$$

This mechanism does not, however, explain proton addition by protonated water clusters. Furthermore, He_m are not likely to survive long under ambient conditions, being quickly quenched by atmospheric moieties like nitrogen (N_2) and water (H_2O), forming their respective molecular ions, also via Penning ionization.[88, 118]

$$He_m + N_2 \rightarrow N_2^+ + He + e^- \quad 1.2$$

$$He_m + H_2O \rightarrow H_2O^+ + He + e^- \quad 1.3$$

The Penning cross sections for He_m ($^3S_1$) with these species are 5×10^{-20}, and 105×10^{-20} m^2, respectively.[126, 127] Of these two reactions, it is most certain that quenching of He_m by nitrogen dominates due to its high abundance in the air.

It has also been suggested that the He_m could interact directly with atmospheric water clusters to generate the protonated water clusters.

$$He_m + (H_2O)_n \rightarrow [(H_2O)_{n-1}H]^+ + OH^- + He \quad 1.4$$

This is the first step in the ionization mechanism proposed for the DART ion source,[2, 80] which was later adopted by those who reported on the PADI source.[93] Although it has not been challenged, this mechanism also seems less likely due to the rapid quenching of the He_m by atmospheric nitrogen.

It has been proposed, however, that the formation of water clusters is the result of an APCI mechanism involving atmospheric nitrogen.[128, 129]

$$N_2^+ + 2N_2 \rightarrow N_4^+ + N_2 \quad 1.5$$

$$N_4^+ + H_2O \rightarrow H_2O^+ + 2N_2 \quad 1.6$$

$$H_2O^+ + H_2O \rightarrow H_3O^+ + OH \quad 1.7$$

$$H_3O^+ + H_2O + N_2 \rightarrow H^+(H_2O)_2 + N_2 \quad 1.8$$

$$H^+(H_2O)_{n-1} + H_2O + N_2 \rightarrow H^+(H_2O)_n + N_2 \quad 1.9$$

Protonated water clusters can then donate a proton to gaseous analyte having a higher proton affinity than the water cluster. This mechanism has been accepted for DBD-based ADI sources.[54, 117, 120, 130] What is less certain is the role of He_m in this reaction. Two areas of thought have emerged regarding the role of He_m species in the ambient ionization process. It is clear that this APCI process can be initiated by Penning ionization of atmospheric nitrogen (1.2). However, recently it has also been suggested that a charge transfer mechanism plays a major role in the ionization of atmospheric nitrogen.[118] I will consider these two mechanisms in the current discussion.

1.3.1.2.1 Formation of Nitrogen Ion via Charge Transfer from Ionic Helium Species

The charge transfer mechanism has most often been considered in theoretical simulations of atmospheric and reduced pressure plasmas.[131-134] In these simulations, charge transfer from helium ion (He^+) and helium dimer ion (He_2^+) are considered.

$$He^+ + N_2 \rightarrow N_2^+ + He \quad 1.10$$

$$He_2^+ + N_2 \rightarrow N_2^+ + 2He \quad 1.11$$

However, in most studies supporting the charge transfer mechanism, the reaction of nitrogen with He^+ is thought to make little contribution.[118, 133] Therefore, major consideration of the charge transfer mechanism is dependent on the formation of He_2^+. According to theoretical models, there are three ways by which He_2^+ is created;[131, 133]

(1) Three body association reaction

$$He^+ + 2He \rightarrow He_2^+ + He \qquad 1.12$$

(2) Metastable conversion

$$He_m + He_m \rightarrow He_2^+ + e^- \qquad 1.13$$

(3) Hornbeck-Molnar process

$$He^* (n \geq 3) + He \rightarrow He_2^+ + e^- \qquad 1.14$$

The charged species can then interact with atmospheric nitrogen and initiate reactions 5-9. Although these charge transfer-related mechanisms are given some emphasis in the literature, there seems to be little experimental evidence that demonstrates contributions by these reactions. This is in part due to the inability to monitor helium ion species spectroscopically.

1.3.1.2.2 Penning Ionization of Atmospheric Nitrogen via Metastable Helium

In Helium-based atmospheric pressure plasmas, the creation of N_2^+ is typically attributed to Penning ionization by He_m,[100, 105, 135-137] and much of the literature on APPJ similarly ascribes the most N_2^+ production to Penning ionization by He_m.[100, 111, 113, 138] Attempts at monitoring this process initially included observations of emissive plasma species like He^* (typically observed at 587.582, 667.815, and 706.519 nm), and N_2^{+*} (typically observed at 391.44, 427.81, 470.92 nm, and 423.65 nm). An energy level diagram of neutral helium and nitrogen ion, with transitions typically observed by emission spectroscopy is displayed in Figure 1.3.

It is known that APPJs are not in local thermodynamic equilibrium. For helium, this means plasma emission can only give information about the excited state population, and not the state into which the atom is decaying. Nitrogen ion emission is typically associated with the creation of the nitrogen ion as it is excited from the nitrogen neutral ground state ($X^1\Sigma_g^+$) to an excited nitrogen ion state ($B^2\Sigma_u^+$). Emission then occurs from the first negative system to the

ground ion state ($X^2\Sigma_g^+$). Anderson et al. used two-dimensional emission spectroscopy to monitor N_2^+ emission in an atmospheric-pressure helium glow discharge, implying that the N_2^+ emission was a good indicator of He_m densities.[137] This assumption not only neglects other processes that can cause ion formation, like electron impact, but also does not take other He_m reactions into account. Unfortunately, plasma emission gives no information about He_m population, and little research has been done to correlate He_m densities with the performance of a helium-based ADI source.

One way to obtain direct information about the relative densities of atoms in a selected state is by laser-induced fluorescence (LIF). LIF has been used to monitor He_m densities in glow discharges, DBDs and rf plasmas under reduced pressure conditions.[139-143] LIF, in this case, is the result of a collisional coupling that takes place between excited levels that are close in energy. In most cases, He_m densities were measured for the purpose of determining electron number densities and electron temperatures in the various helium plasmas.[139-142] Planar LIF has been used as a means to image spatial distributions of He_m in a reduced pressure rf plasma, again for the determination of electron number densities and electron temperatures.[142] Likewise, observation of nitrogen ion species need not be limited by emission measurements. Relative ground state populations of N_2^+ can also be determined by LIF.

In my work, I used planar LIF to image density distributions of He_m ($^3S_1$) and ground state N_2^+ in a helium-based dielectric-barrier discharge (He-DBD) under ambient conditions as an important step to understanding the ADI mechanism for helium-based electrical discharge ADI sources. In Chapter 2, the concept of collisionally-assisted LIF is introduced as a diagnostic tool to determine relative distributions of He_m populations in a DBD APPJ used as an ADI source. Axial distributions of He_m in the plasma are presented for a variety of power, frequency

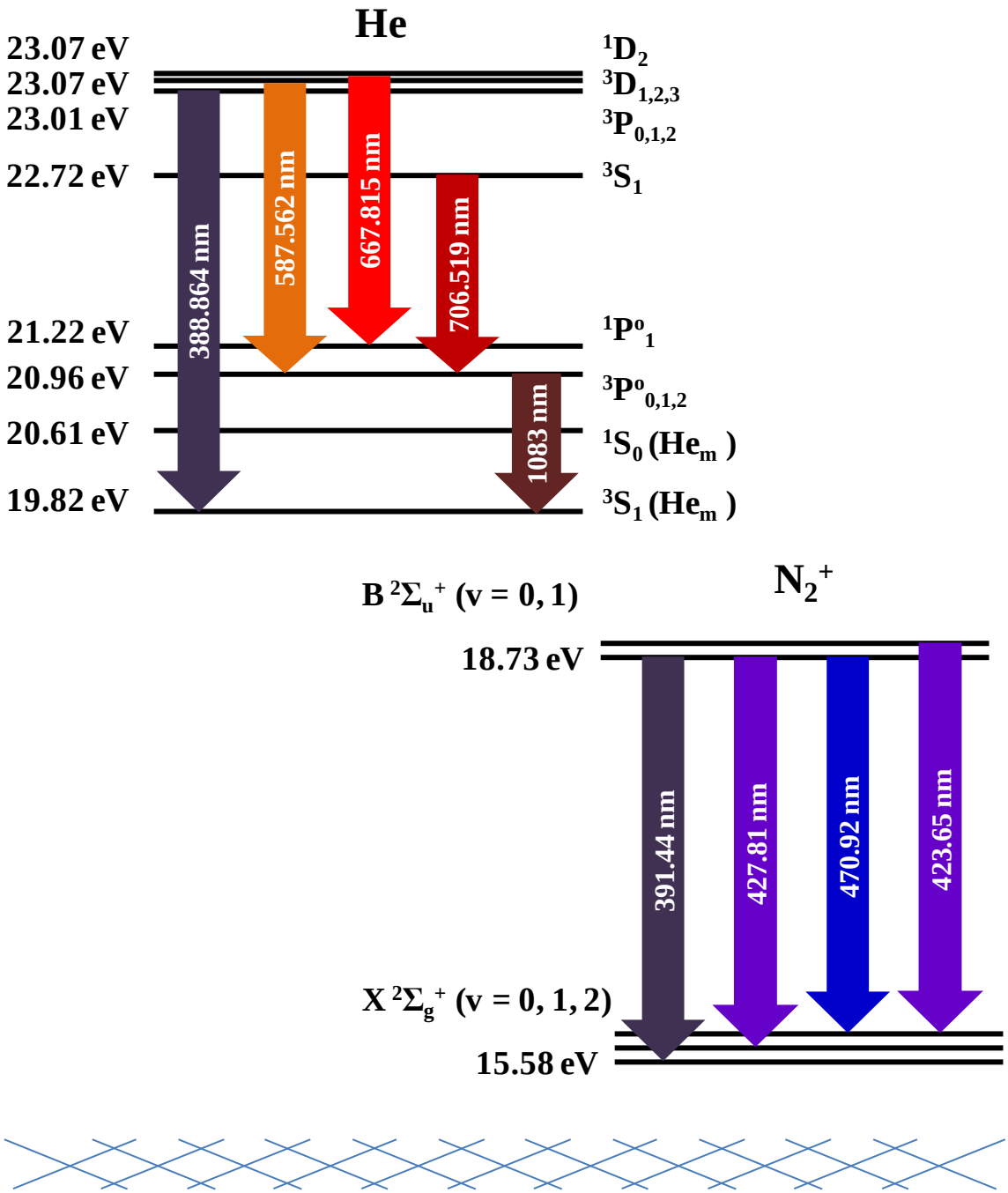

Figure 1.3: Energy level diagram of helium and nitrogen ion depicting typically observed emission transitions (not to scale).

and discharge gas flow rate settings. Axial profiles of He_m populations are compared to typically observed He^* and N_2^{+*} emission, and a correlation is made between He_m and N_2^{+*} states. Also, radial distributions of He_m are presented for 1, 4, and 7 mm downstream from the tip of the capillary. The effect of a glass slide on the He_m population is also discussed and the idea of plasma-surface matrix effects is presented. In Chapter 3, the time-dependent nature of the DBD APPJ is discussed and temporally and spectrally resolved axial distributions of key plasma species are presented. LIF is used to obtain temporally and spectrally resolved axial profiles of He_m and ground state N_2^+ fluorescence. A strong spatial and temporal correlation is observed between the two species, suggesting Penning ionization. Temporally and spectrally resolved profiles of He^*, N_2^{+*}, and N_2^* emission are also presented. The effects of hydrogen (H_2) on a helium DBD APPJ are presented in Chapter 4. The addition of 1% H_2 to the discharge gas results in a quenching of excited plasma species including a severe quenching of the He_m state. Despite the quenching of the He_m state, an improvement in ambient desorption and ionization is observed when using a He/1%H_2 discharge gas. Experiments for determining the ratio of H_2 that provides the best ADI-MS signal are also explained. Continuing work with He/H_2 plasma-based ADI sources is discussed in Chapter 5. Future spectroscopic studies of the DBD APPJ including tunable diode laser absorption spectroscopy, and mass spectrometric studies involving negative ion mode MS are also discussed in that chapter.

1.4 Future Studies with ADI-MS

Although the literature continues to include research on the creation and recreation of ADI sources and tests of their viability as sources for detection of specific target analytes, the novelty of ADI sources will eventually fade away. It is important, if the field of ambient mass spectrometry is to reach its full potential, that research must continue in the areas of fundamental

understanding, application, and implementation. The commercialization of DART and DESI by IonSense and Prosolia, respectively, has led to their continued use and development. The usefulness of these and other sources has been demonstrated and will likely allow the field to thrive as more applications are discovered and ADI sources are implemented in commercial use. While ADI-MS will be continually used, research will continue to work toward improvement in the performance of ADI sources.

One of the fundamental challenges facing the field of ADI-MS is that of quantification. The ability to determine the amount of a detectable analyte is dependent on desorption and ionization processes. Consider the detection of illegal drugs. There are a number of surfaces that could be sampled including cloth (clothes, upholstery), paper (money, cardboard), wood, ceramic, medal, plastic, etc. If the desorption of the analyte depends on thermal desorption processes, as with electrical discharge-type ADI sources, it not only depends on the volatility of the sample, but also on the thermal conductivity of the sampling surface. This is just one example of matrix effects that hinder quantitative analysis of drugs. Other matrix effects, like the presence of solvent or analytes with competing proton affinities, have been studied.[76, 77, 80, 120] Understanding of fundamental plasma processes and matrix effects will help define the improvement that can be made to ADI sources. Therefore, fundamental studies are extremely important for the growth and development of the field.

1.5 References

1. Takats, Z.; Wiseman, J. M.; Gologan, B.; Cooks, R. G., Mass Spectrometry Sampling under Ambient Conditions with Desorption Electrospray Ionization. *Science* **2004,** *306* (5695), 471-473.
2. Cody, R. B.; Laramee, J. A.; Durst, H. D., Versatile New Ion Source for the Analysis of Materials in Open Air under Ambient Conditions. *Anal. Chem.* **2005,** *77* (8), 2297-2302.
3. Weston, D. J., Ambient Ionization Mass Spectrometry: Current Understanding of Mechanistic Theory; Analytical Performance and Application Areas. *Analyst* **2010,** *135* (4), 661-668.

4. Huang, M. Z.; Cheng, S. C.; Cho, Y. T.; Shiea, J., Ambient Ionization Mass Spectrometry: A Tutorial. *Anal. Chim. Acta* **2011,** *702* (1), 1-15.
5. Venter, A.; Nefliu, M.; Graham Cooks, R., Ambient Desorption Ionization Mass Spectrometry. *TrAC-Trend. Anal. Chem.* **2008,** *27* (4), 284-290.
6. Chen, H. W.; Gamez, G.; Zenobi, R., What Can We Learn from Ambient Ionization Techniques? *J. Am. Soc. Mass Spectr.* **2009,** *20* (11), 1947-1963.
7. Alberici, R.; Simas, R.; Sanvido, G.; Romão, W.; Lalli, P.; Benassi, M.; Cunha, I.; Eberlin, M., Ambient Mass Spectrometry: Bringing MS into the "Real World". *Anal. Bioanal. Chem.* **2010,** *398* (1), 265-294.
8. Ifa, D. R.; Wu, C. P.; Ouyang, Z.; Cooks, R. G., Desorption Electrospray Ionization and Other Ambient Ionization Methods: Current Progress and Preview. *Analyst* **2010,** *135* (4), 669-681.
9. Helmy, R.; Schafer, W.; Buhler, L.; Marcinko, S.; Musselman, B.; Guidry, E.; Jenkins, H.; Fleitz, F.; Welch, C. J., Ambient Pressure Desorption Ionization Mass Spectrometry in Support of Preclinical Pharmaceutical Development. *Org. Process Res. Dev.* **2010,** *14* (2), 386-392.
10. Wang, H.; Sun, W. J.; Zhang, J. S.; Yang, X. H.; Lin, T.; Ding, L., Desorption Corona Beam Ionization Source for Mass Spectrometry. *Analyst* **2010,** *135* (4), 688-695.
11. Chen, H.; Talaty, N. N.; Takats, Z.; Cooks, R. G., Desorption Electrospray Ionization Mass Spectrometry for High-Throughput Analysis of Pharmaceutical Samples in the Ambient Environment. *Anal. Chem.* **2005,** *77* (21), 6915-6927.
12. Weston, D. J.; Bateman, R.; Wilson, I. D.; Wood, T. R.; Creaser, C. S., Direct Analysis of Pharmaceutical Drug Formulations Using Ion Mobility Spectrometry/Quadrupole-Time-of-Flight Mass Spectrometry Combined with Desorption Electrospray Ionization. *Anal. Chem.* **2005,** *77* (23), 7572-7580.
13. Williams, J. P.; Patel, V. J.; Holland, R.; Scrivens, J. H., The Use of Recently Described Ionisation Techniques for the Rapid Analysis of Some Common Drugs and Samples of Biological Origin. *Rapid Commun. Mass Sp.* **2006,** *20* (9), 1447-1456.
14. Petucci, C.; Diffendal, J.; Kaufman, D.; Mekonnen, B.; Terefenko, G.; Musselman, B., Direct Analysis in Real Time for Reaction Monitoring in Drug Discovery. *Anal. Chem.* **2007,** *79* (13), 5064-5070.
15. Steiner, R. R.; Larson, R. L., Validation of the Direct Analysis in Real Time Source for Use in Forensic Drug Screening. *J. Forensic Sci.* **2009,** *54* (3), 617-622.
16. Fernández, F. M.; Cody, R. B.; Green, M. D.; Hampton, C. Y.; McGready, R.; Sengaloundeth, S.; White, Nicholas J.; Newton, P. N., Characterization of Solid Counterfeit Drug Samples by Desorption Electrospray Ionization and Direct-Analysis-in-Real-Time Coupled to Time-of-Flight Mass Spectrometry. *ChemMedChem* **2006,** *1* (7), 702-705.
17. Leuthold, L. A.; Mandscheff, J.-F.; Fathi, M.; Giroud, C.; Augsburger, M.; Varesio, E.; Hopfgartner, G., Desorption Electrospray Ionization Mass Spectrometry: Direct Toxicological Screening and Analysis of Illicit Ecstasy Tablets. *Rapid Commun. Mass Sp.* **2006,** *20* (2), 103-110.
18. Huang, G.; Chen, H.; Zhang, X.; Cooks, R. G.; Ouyang, Z., Rapid Screening of Anabolic Steroids in Urine by Reactive Desorption Electrospray Ionization. *Anal. Chem.* **2007,** *79* (21), 8327-8332.

19. Kertesz, V.; Van Berkel, G. J.; Vavrek, M.; Koeplinger, K. A.; Schneider, B. B.; Covey, T. R., Comparison of Drug Distribution Images from Whole-Body Thin Tissue Sections Obtained Using Desorption Electrospray Ionization Tandem Mass Spectrometry and Autoradiography. *Anal. Chem.* **2008,** *80* (13), 5168-5177.
20. Zhao, Y.; Lam, M.; Wu, D.; Mak, R., Quantification of Small Molecules in Plasma with Direct Analysis in Real Time Tandem Mass Spectrometry, without Sample Preparation and Liquid Chromatographic Separation. *Rapid Commun. Mass Sp.* **2008,** *22* (20), 3217-3224.
21. Liu, Y.; Lin, Z.; Zhang, S.; Yang, C.; Zhang, X., Rapid Screening of Active Ingredients in Drugs by Mass Spectrometry with Low-Temperature Plasma Probe. *Anal. Bioanal. Chem.* **2009,** *395* (3), 591-599.
22. Jagerdeo, E.; Abdel-Rehim, M., Screening of Cocaine and Its Metabolites in Human Urine Samples by Direct Analysis in Real-Time Source Coupled to Time-of-Flight Mass Spectrometry after Online Preconcentration Utilizing Microextraction by Packed Sorbent. *J. Am. Soc. Mass Spectr.* **2009,** *20* (5), 891-899.
23. Jackson, A. U.; Garcia-Reyes, J. F.; Harper, J. D.; Wiley, J. S.; Molina-Diaz, A.; Ouyang, Z.; Graham Cooks, R., Analysis of Drugs of Abuse in Biofluids by Low Temperature Plasma (LTP) Ionization Mass Spectrometry. *Analyst* **2010,** *135* (5), 927-933.
24. Takáts, Z.; Cotte-Rodriguez, I.; Talaty, N.; Chen, H.; Cooks, R. G., Direct, Trace Level Detection of Explosives on Ambient Surfacaes by Desorption Electrospray Ionization Mass Spectrometry. *Chem. Commun.* **2005**, 1950-1952.
25. Cotte-Rodriguez, I.; Hernandez-Soto, H.; Chen, H.; Cooks, R. G., In Situ Trace Detection of Peroxide Explosives by Desorption Electrospray Ionization and Desorption Atmospheric Pressure Chemical Ionization. *Anal. Chem.* **2008,** *80* (5), 1512-1519.
26. Nilles, J. M.; Connell, T. R.; Durst, H. D., Quantitation of Chemical Warfare Agents Using the Direct Analysis in Real Time (DART) Technique. *Anal. Chem.* **2009,** *81* (16), 6744-6749.
27. Zhang, Y.; Ma, X.; Zhang, S.; Yang, C.; Ouyang, Z.; Zhang, X., Direct Detection of Explosives on Solid Surfaces by Low Temperature Plasma Desorption Mass Spectrometry. *Analyst* **2009,** *134* (1), 176-181.
28. Song, Y.; Cooks, R. G., Atmospheric Pressure Ion/Molecule Reactions for the Selective Detection of Nitroaromatic Explosives Using Acetonitrile and Air as Reagents. *Rapid Commun. Mass Sp.* **2006,** *20* (20), 3130-3138.
29. Garcia-Reyes, J. F.; Harper, J. D.; Salazar, G. A.; Charipar, N. A.; Ouyang, Z.; Cooks, R. G., Detection of Explosives and Related Compounds by Low-Temperature Plasma Ambient Ionization Mass Spectrometry. *Anal. Chem.* **2011,** *83* (3), 1084-1092.
30. Chen, H.; Liang, H.; Ding, J.; Lai, J.; Huan, Y.; Qiao, X., Rapid Differentiation of Tea Products by Surface Desorption Atmospheric Pressure Chemical Ionization Mass Spectrometry. *J. Agr. Food Chem.* **2007,** *55* (25), 10093-10100.
31. Talaty, N.; Takáts, Z.; Cooks, R. G., Rapid in Situe Detection of Alkaloids in Plant Tissue under Ambient Conditions Using Desorption Electrospray Ionization. *Analyst* **2005,** *130*, 1624-1633.
32. Jackson, A. U.; Tata, A.; Wu, C.; Perry, R. H.; Haas, G.; West, L.; Cooks, R. G., Direct Analysis of Stevia Leaves for Diterpene Glycosides by Desorption Electrospray Ionization Mass Spectrometry. *Analyst* **2009,** *134*, 867-874.

33. Kim, H. J.; Jang, Y. P., Direct Analysis of Curcumin in Turmeric by DART-MS. *Phytochem. Analysis* **2009,** *20* (5), 372-377.
34. Maleknia, S. D.; Vail, T. M.; Cody, R. B.; Sparkman, D. O.; Bell, T. L.; Adams, M. A., Temperature-Dependent Release of Volatile Organic Compounds of Eucalypts by Direct Analysis in Real Time (DART) Mass Spectrometry. *Rapid Commun. Mass Sp.* **2009,** *23* (15), 2241-2246.
35. McEwen, C. N.; Larsen, B. S., Ionization Mechanisms Related to Negative Ion APPI, APCI, and DART. 2009; Vol. 20, pp 1518-1521.
36. Huang, G.; Ouyang, Z.; Cooks, R. G., High-Throughput Trace Melamine Analysis in Complex Mixtures. *Chem. Commun.* **2009**, 556-558.
37. Vaclavik, L.; Cajka, T.; Hrbek, V.; Hajslova, J., Ambient Mass Spectrometry Employing Direct Analysis in Real Time (DART) Ion Source for Olive Oil Quality and Authenticity Assessment. *Anal. Chim. Acta* **2009,** *645* (1-2), 56-63.
38. Dane, A. J.; Cody, R. B., Selective Ionization of Melamine in Powdered Milk by Using Argon Direct Analysis in Real Time (DART) Mass Spectrometry. *Analyst* **2010,** *135* (4), 696-699.
39. Chen, H.; Yang, S.; Wortmann, A.; Zenobi, R., Neutral Desorption Sampling of Living Objects for Rapid Analysis by Extractive Electrospray Ionization Mass Spectrometry13. *Angewandte Chemie International Edition* **2007,** *46* (40), 7591-7594.
40. Garcia-Reyes, J. F.; Mazzoti, F.; Harper, J. D.; Charipar, N. A.; Oradu, S.; Ouyang, Z.; Sindona, G.; Cooks, R. G., Direct Olive Oil Analysis by Low-Temperature Plasma (LTP) Ambient Ionization Mass Spectrometry. *Rapid Commun. Mass Sp.* **2009,** *23* (19), 3057-3062.
41. Huang, G. M.; Xu, W.; Visbal-Onufrak, M. A.; Ouyang, Z.; Cooks, R. G., Direct Analysis of Melamine in Complex Matrices Using a Handheld Mass Spectrometer. *Analyst* **2010,** *135* (4), 705-711.
42. Perez, J. J.; Harris, G. A.; Chipuk, J. E.; Brodbelt, J. S.; Green, M. D.; Hampton, C. Y.; Fernandez, F. M., Transmission-Mode Direct Analysis in Real Time and Desorption Electrospray Ionization Mass Spectrometry of Insecticide-Treated Bednets for Malaria Control. *Analyst* **2010,** *135* (4), 712-719.
43. Nielen, M. W. F.; Hooijerink, H.; Zomer, P.; Mol, J. G. J., Desorption Electrospray Ionization Mass Spectrometry in the Analysis of Chemical Food Contaminants in Food. *TrAC-Trend. Anal. Chem.* **2011,** *30* (2), 165-180.
44. Wiley, J. S.; Garcia-Reyes, J. F.; Harper, J. D.; Charipar, N. A.; Zheng, O.; Cooks, R. G., Screening of Agrochemicals in Foodstuffs Using Low-Temperature Plasma (LTP) Ambient Ionization Mass Spectrometry. *Analyst* **2010,** *135*, 971-979.
45. Cajka, T.; Riddellova, K.; Zomer, P.; Mol, H.; Hajslova, J., Direct Analysis of Dithiocarbamate Fungicides in Fruit by Ambient Mass Spectrometry. *Food Addit. Contam. Part A-Chem.* **2011,** *28* (10), 1372-1382.
46. Edison, S. E.; Lin, L. A.; Parrales, L., Practical Considerations for the Rapid Screening for Pesticides Using Ambient Pressure Desorption Ionisation with High-Resolution Mass Spectrometry. *Food Addit. Contam. Part A-Chem.* **2011,** *28* (10), 1393-1404.
47. Chen, H.; Pan, Z.; Talaty, N.; Raftery, D.; Cooks, R. G., Combining Desorption Electrospray Ionization Mass Spectrometry and Nuclear Magnetic Resonance for Differential Metabolomics without Sample Preparation. *Rapid Commun. Mass Sp.* **2006,** *20* (10), 1577-1584.

48. Myung, S.; Wiseman, J. M.; Valentine, S. J.; TakÃ¡ts, Z. n.; Cooks, R. G.; Clemmer, D. E., Coupling Desorption Electrospray Ionization with Ion Mobility/Mass Spectrometry for Analysis of Protein Structure:Â€‰ Evidence for Desorption of Folded and Denatured States. *J. Phys. Chem. B* **2006,** *110* (10), 5045-5051.
49. Valentine, S. J.; Plasencia, M. D.; Liu, X.; Krishnan, M.; Naylor, S.; Udseth, H. R.; Smith, R. D.; Clemmer, D. E., Toward Plasma Proteome Profiling with Ion Mobility-Mass Spectrometry. *J. Proteome Res.* **2006,** *5* (11), 2977-2984.
50. Shin, Y.-S.; Drolet, B.; Mayer, R.; Dolence, K.; Basile, F., Desorption Electrospray Ionization-Mass Spectrometry of Proteins. *Anal. Chem.* **2007,** *79* (9), 3514-3518.
51. Pasilis, S. P.; Kertesz, V.; Van Berkel, G. J.; Schulz, M.; Schorcht, S., HPTLC/DESI-MS Imaging of Tryptic Protein Digests Separated in Two Dimensions. *J. Mass Spectrom.* **2008,** *43* (12), 1627-1635.
52. Van Berkel, G. J.; Ford, M. J.; Deibel, M. A., Thin-Layer Chromatography and Mass Spectrometry Coupled Using Desorption Electrospray Ionization. *Anal. Chem.* **2005,** *77* (5), 1207-1215.
53. Kauppila, T. J.; Talaty, N.; Salo, P. K.; Kotiaho, T.; Kostiainen, R.; Cooks, R. G., New Surfaces for Desorption Electrospray Ionization Mass Spectrometry: Porous Silicon and Ultra-Thin Layer Chromatography Plates. *Rapid Commun. Mass Sp.* **2006,** *20* (14), 2143-2150.
54. Harper, J. D.; Charipar, N. A.; Mulligan, C. C.; Zhang, X.; Cooks, R. G.; Ouyang, Z., Low-Temperature Plasma Probe for Ambient Desorption Ionization. *Anal. Chem.* **2008,** *80* (23), 9097-9104.
55. Miao, Z.; Chen, H., Direct Analysis of Liquid Samples by Desorption Electrospray Ionization-Mass Spectrometry (DESI-MS). *J. Am. Soc. Mass Spectr.* **2009,** *20* (1), 10-19.
56. Wells, J. M.; Roth, M. J.; Keil, A. D.; Grossenbacher, J. W.; Justes, D. R.; Patterson, G. E.; Barket Jr, D. J., Implementation of DART and DESI Ionization on a Fieldable Mass Spectrometer. *J. Am. Soc. Mass Spectr.* **2008,** *19* (10), 1419-1424.
57. Ifa, D. R.; Wiseman, J. M.; Song, Q.; Cooks, R. G., Development of Capabilities for Imaging Mass Spectrometry under Ambient Conditions with Desorption Electrospray Ionization (DESI). *Int. J. Mass Spectrom.* **2007,** *259* (1-3), 8-15.
58. Esquenazi, E.; Yang, Y.-L.; Watrous, J.; Gerwick, W. H.; Dorrestein, P. C., Imagin Mass Spectrometry of Natural Products. *Nat. Prod. Rep.* **2009,** *26*, 1521-1534.
59. Lane, A. L.; Nyadong, L.; Galhena, A. S.; Shearer, T. L.; Stout, E. P.; Parry, R. M.; Kwasnik, M.; Wang, M. D.; Hay, M. E.; Fernandez, F. M.; Kubanek, J., Desorption Electrospray Ionization Mass Spectrometry Reveals Surface-Mediated Antifungal Chemical Defense of a Tropical Seaweed. *Proceedings of the National Academy of Sciences* **2009,** *106* (18), 7314-7319.
60. Nemes, P.; Barton, A. A.; Vertes, A., Three-Dimensional Imaging of Metabolites in Tissues under Ambient Conditions by Laser Ablation Electrospray Ionization Mass Spectrometry. *Anal. Chem.* **2009,** *81* (16), 6668-6675.
61. Van Berkel, G. J.; Pasilis, S. P.; Ovchinnikova, O., Established and Emerging Atmospheric Pressure Surface Sampling/Ionization Techniques for Mass Spectrometry. *J. Mass Spectrom.* **2008,** *43* (9), 1161-1180.
62. Harris, G. A.; Nyadong, L.; Fernandez, F. M., Recent Developments in Ambient Ionization Techniques for Analytical Mass Spectrometry. *Analyst* **2008,** *133*, 1297-1301.

63. Nyadong, L.; Green, M. D.; De Jesus, V. R.; Newton, P. N.; FernÃ¡ndez, F. M., Reactive Desorption Electrospray Ionization Linear Ion Trap Mass Spectrometry of Latest-Generation Counterfeit Antimalarials Via Noncovalent Complex Formation. *Anal. Chem.* **2007,** *79* (5), 2150-2157.
64. Wu, C.; Ifa, D. R.; Manicke, N. E.; Cooks, R. G., Rapid, Direct Analysis of Cholesterol by Charge Labeling in Reactive Desorption Electrospray Ionization. *Anal. Chem.* **2009,** *81* (18), 7618-7624.
65. Wu, C.; Qian, K.; Nefliu, M.; Cooks, R. G., Ambient Analysis of Saturated Hydrocarbons Using Discharge-Induced Oxidation in Desorption Electrospray Ionization. *J. Am. Soc. Mass Spectr.* **2010,** *21* (2), 261-267.
66. Chen, H.; Cotte-Rodríguez, I.; Cooks, R. G., Cis-Diol Functional Group Recognition by Reactive Desorption Electrospray Ionization (DESI). *Chem. Commun.* **2006**, 597-599.
67. Ifa, D. R.; Manicke, N. E.; Dill, A. L.; Cooks, R. G., Latent Fingerprint Chemical Imaging by Mass Spectrometry. *Science* **2008,** *321* (5890), 805.
68. Takáts, Z.; Wiseman, J. M.; Cooks, R. G., Ambient Mass Spectrometry Using Desorption Electrospray Ionization (DESI): Instrumentation, Mechanisms and Applications in Forensics, Chemistry, and Biology. *J. Mass Spectrom.* **2005,** *40* (10), 1261-1275.
69. Costa, A. B.; Cooks, R. G., Simulation of Atmospheric Transport and Droplet-Thin Film Collisions in Desorption Electrospray Ionization. *Chem. Commun.* **2007**, 3915-3917.
70. Costa, A. B.; Cooks, R. G., Simulated Splashes: Elucidating the Mechanism of Desorption Electrospray Ionization Mass Spectrometry. *Chem. Phys. Lett.* **2008,** *464*, 1-8.
71. Wood, M. C.; Busby, D. K.; Farnsworth, P. B., Microscopic Imaging of Glass Surfaces under the Effects of Desorption Electrospray Ionization. *Anal. Chem.* **2009,** *81* (15), 6407-6415.
72. Haddad, R.; Sparrapan, R.; Eberlin, M. N., Desorption Sonic Spray Ionization for (High) Voltage-Free Ambient Mass Spectrometry. *Rapid Commun. Mass Sp.* **2006,** *20* (19), 2901-2905.
73. Haddad, R.; Sparrapan, R.; Kotiaho, T.; Eberlin, M. N., Easy Ambient Sonic-Spray Ionization-Membrane Interface Mass Spectrometry for Direct Analysis of Solution Constituents. *Anal. Chem.* **2008,** *80* (3), 898-903.
74. Özdemir, A.; Chen, C.-H., Electrode-Assisted Desorption Electrospray Ionization Mass Spectrometry. *J. Mass Spectrom.* **2010,** *45* (10), 1203-1211.
75. Shelley, J. T.; Wiley, J. S.; Chan, G. C. Y.; Schilling, G. D.; Ray, S. J.; Hieftje, G. M., Characterization of Direct-Current Atmospheric-Pressure Discharges Useful for Ambient Desorption/Ionization Mass Spectrometry. *J. Am. Soc. Mass Spectr.* **2009,** *20* (5), 837-844.
76. Song, L.; Gibson, S. C.; Bhandari, D.; Cook, K. D.; Bartmess, J. E., Ionization Mechanism of Positive-Ion Direct Analysis in Real Time: A Transient Microenvironment Concept. *Anal. Chem.* **2009,** *81* (24), 10080-10088.
77. Song, L.; Dykstra, A. B.; Yao, H.; Bartmess, J. E., Ionization Mechanism of Negative Ion-Direct Analysis in Real Time: A Comparative Study with Negative Ion-Atmospheric Pressure Photoionization. *J. Am. Soc. Mass Spectr.* **2009,** *20* (1), 42-50.
78. Jones, R. W.; Cody, R. B.; McClelland, J. F., Differentiating Writing Inks Using Direct Analysis in Real Time Mass Spectrometry. *J. Forensic Sci.* **2006,** *51* (4), 915-918.
79. Morlock, G.; Ueda, Y., New Coupling of Planar Chromatography with Direct Analysis in Real Time Mass Spectrometry. *J. Chromatogr. A* **2007,** *1143* (1-2), 243-251.

80. Cody, R. B., Observation of Molecular Ions and Analysis of Nonpolar Compounds with the Direct Analysis in Real Time Ion Source. *Anal. Chem.* **2008,** *81* (3), 1101-1107.
81. Yu, S.; Crawford, E.; Tice, J.; Musselman, B.; Wu, J.-T., Bioanalysis without Sample Cleanup or Chromatography: The Evaluation and Initial Implementation of Direct Analysis in Real Time Ionization Mass Spectrometry for the Quantification of Drugs in Biological Matrixes. *Anal. Chem.* **2008,** *81* (1), 193-202.
82. Domin, M. A.; Steinberg, B. D.; Quimby, J. M.; Smith, N. J.; Greene, A. K.; Scott, L. T., Routine Analysis and Characterization of Highly Insoluble Polycyclic Aromatic Compounds by Direct Analysis in Real Time Mass Spectrometry (DART). *Analyst* **2010,** *135* (4), 700-704.
83. Jeckelmann, N.; Haefliger, O. P., Release Kinetics of Actives from Chewing Gums into Saliva Monitored by Direct Analysis in Real Time Mass Spectrometry. *Rapid Commun. Mass Sp.* **2010,** *24* (8), 1165-1171.
84. Zhou, M.; McDonald, J. F.; Fernandez, F. M., Optimization of a Direct Analysis in Real Time/Time-of-Flight Mass Spectrometry Method for Rapid Serum Metabolomic Fingerprinting. *J. Am. Soc. Mass Spectr.* **2010,** *21* (1), 68-75.
85. Harris, G. A.; Kwasnik, M.; Fernandez, F. M., Direct Analysis in Real Time Coupled to Multiplexed Drift Tube Ion Mobility Spectrometry for Detecting Toxic Chemicals. *Anal. Chem.* **2011,** *83* (6), 1908-1915.
86. Pfaff, A. M.; Steiner, R. R., Development and Validation of AccuTOF-DART(TM) as a Screening Method for Analysis of Bank Security Device and Pepper Spray Components. *Forensic Sci. Int.* **2011,** *206* (1-3), 62-70.
87. Andrade, F. J.; Shelley, J. T.; Wetzel, W. C.; Webb, M. R.; Gamez, G.; Ray, S. J.; Hieftje, G. M., Atmospheric Pressure Chemical Ionization Source. 2. Desorption Ionization for the Direct Analysis of Solid Compounds. *Anal. Chem.* **2008,** *80* (8), 2654-2663.
88. Andrade, F. J.; Shelley, J. T.; Wetzel, W. C.; Webb, M. R.; Gamez, G.; Ray, S. J.; Hieftje, G. M., Atmospheric Pressure Chemical Ionization Source. 1. Ionization of Compounds in the Gas Phase. *Anal. Chem.* **2008,** *80* (8), 2646-2653.
89. Shelley, J. T.; Hieftje, G. M., Fast Transient Analysis and First-Stage Collision-Induced Dissociation with the Flowing Atmospheric-Pressure Afterglow Ionization Source to Improve Analyte Detection and Identification. *Analyst* **2010,** *135* (4), 682-687.
90. Shelley, J. T.; Ray, S. J.; Hieftje, G. M., Laser Ablation Coupled to a Flowing Atmospheric Pressure Afterglow for Ambient Mass Spectral Imaging. *Anal. Chem.* **2008,** *80* (21), 8308-8313.
91. Schilling, G. D.; Shelley, J. T.; Broekaert, J. A. C.; Sperline, R. P.; Denton, M. B.; Barinaga, C. J.; Koppenaal, D. W.; Hieftje, G. M., Use of an Ambient Ionization Flowing Atmospheric-Pressure Afterglow Source for Elemental Analysis through Hydride Generation. *J. Anal. At. Spectrom.* **2009,** *24* (1), 34-40.
92. Shelley, J. T.; Wiley, J. S.; Hieftje, G. M., Ultrasensitive Ambient Mass Spectrometric Analysis with a Pin-to-Capillary Flowing Atmospheric-Pressure Afterglow Source. *Anal. Chem.* **2011,** *83* (14), 5741-5748.
93. Ratcliffe, L. V.; Rutten, F. J. M.; Barrett, D. A.; Whitmore, T.; Seymour, D.; Greenwood, C.; Aranda-Gonzalvo, Y.; Robinson, S.; McCoustra, M., Surface Analysis under Ambient Conditions Using Plasma-Assisted Desorption/Ionization Mass Spectrometry. *Anal. Chem.* **2007,** *79* (16), 6094-6101.

94. Zhu, Z.; Zhang, S.; Lv, Y.; Zhang, X., Atomization of Hydride with a Low-Temperature, Atmospheric Pressure Dielectric Barrier Discharge and Its Application to Arsenic Speciation with Atomic Absorption Spectrometry. *Anal. Chem.* **2006,** *78* (3), 865-872.
95. Zhu, Z.; Zhang, S.; Xue, J.; Zhang, X., Application of Atmospheric Pressure Dielectric Barrier Discharge Plasma for the Determination of Se, Sb and Sn with Atomic Absorption Spectrometry. *Spectrochim. Acta B* **2006,** *61* (8), 916-921.
96. Zhu, Z.; Chan, G. C. Y.; Ray, S. J.; Zhang, X.; Hieftje, G. M., Microplasma Source Based on a Dielectric Barrier Discharge for the Determination of Mercury by Atomic Emission Spectrometry. *Anal. Chem.* **2008,** *80* (22), 8622-8627.
97. Rice, G. W.; D'Silva, A. P.; Fassel, V. A., A New He Discharge-Afterglow and Its Application as a Gas Chromatographic Detector. *Spectrochim. Acta B* **1985,** *40* (10-12), 1573-1584.
98. Kunze, K.; Miclea, M.; Franzke, J.; Niemax, K., The Dielectric Barrier Discharge as a Detector for Gas Chromatography. *Spectrochim. Acta B* **2003,** *58* (8), 1435-1443.
99. Vautz, W.; Michels, A.; Franzke, J., Micro-Plasma: A Novel Ionisation Source for Ion Mobility Spectrometry. *Anal. Bioanal. Chem.* **2008,** *391* (7), 2609-2615.
100. Hayen, H.; Michels, A.; Franzke, J., Dielectric Barrier Discharge Ionization for Liquid Chromatography/Mass Spectrometry. *Anal. Chem.* **2009,** *81* (24), 10239-10245.
101. Kogelschatz, U., Dielectric-Barrier Discharges: Their History, Discharge Physics, and Industrial Applications. *Plasma Chem. Plasma P.* **2003,** *23* (1), 1-46.
102. Schutze, A.; Jeong, J. Y.; Babayan, S. E.; Jaeyoung, P.; Selwyn, G. S.; Hicks, R. F., The Atmospheric-Pressure Plasma Jet: A Review and Comparison to Other Plasma Sources. *IEEE Transactions on Plasma Science* **1998,** *26* (6), 1685-1694.
103. Walsh, J. L.; Shi, J. J.; Kong, M. G., Contrasting Characteristics of Pulsed and Sinusoidal Cold Atmospheric Plasma Jets. *Appl. Phys. Lett.* **2006,** *88* (17), 171501-3.
104. Jiang, N.; Ji, A.; Cao, Z., Atmospheric Pressure Plasma Jet: Effect of Electrode Configuration, Discharge Behavior, and Its Formation Mechanism. *J. Appl. Phys.* **2009,** *106* (1), 013308-7.
105. Zhu, W. C.; Li, Q.; Zhu, X.-M.; Pu, Y. K., Characteristics of Atmospheric Pressure Plasma Jets Emerging into Ambient Air and Helium. *J. Phys. Appl. Phys.* **2009,** *42* (20), 202002.
106. Park, H. S.; Kim, S. J.; Joh, H. M.; Chung, T. H.; Bae, S. H.; Leem, S. H., Optical and Electrical Characterization of an Atmospheric Pressure Microplasma Jet with a Capillary Electrode. *Phys. Plamsas* **2010,** *17* (3), 033502-10.
107. Niemi, K.; Waskoenig, J.; Sadeghi, N.; Gans, T.; O'Connell, D., The Role of Helium Metastable States in Radio-Frequency Driven Heliumâ€“Oxygen Atmospheric Pressure Plasma Jets: Measurement and Numerical Simulation. *Plasma Sources Sci. T.* **2011,** *20* (5), 055005.
108. Teschke, M.; Kedzierski, J.; Finantu-Dinu, E. G.; Korzec, D.; Engemann, J., High-Speed Photographs of a Dielectric Barrier Atmospheric Pressure Plasma Jet. *IEEE Transactions on Plasma Science* **2005,** *33* (2), 310-311.
109. Shi, J.; Zhong, F.; Zhang, J.; Liu, D. W.; Kong, M. G., A Hypersonic Plasma Bullet Train Traveling in an Atmospheric Dielectric-Barrier Discharge Jet. *Phys. Plamsas* **2008,** *15* (1), 013504-5.
110. Ye, R.; Zheng, W., Temporal-Spatial-Resolved Spectroscopic Study on the Formation of an Atmospheric Pressure Microplasma Jet. *Appl. Phys. Lett.* **2008,** *93* (7), 071502-3.

111. Xiong, Q.; Lu, X.; Liu, J.; Xian, Y.; Xiong, Z.; Zou, F.; Zou, C.; Gong, W.; Hu, J.; Chen, K.; Pei, X.; Jiang, Z.; Pan, Y., Temporal and Spatial Resolved Optical Emission Behaviors of a Cold Atmospheric Pressure Plasma Jet. *J. Appl. Phys.* **2009,** *106* (8), 083302-6.
112. Li, Q.; Zhu, X.-M.; Li, J.-T.; Pu, Y.-K., Role of Metastable Atoms in the Propagation of Atmospheric Pressure Dielectric Barrier Discharge Jets. *J. Appl. Phys.* **2010,** *107* (4), 043304-7.
113. Urabe, K.; Morita, T.; Tachibana, K.; Ganguly, B. N., Investigation of Discharge Mechanisms in Helium Plasma Jet at Atmospheric Pressure by Laser Spectroscopic Measurements. *J. Phys. Appl. Phys.* **2010,** *43* (9), 095201.
114. Algwari, Q. T.; O'Connell, D., Electron Dynamics and Plasma Jet Formation in a Helium Atmospheric Pressure Dielectric Barrier Discharge Jet. *Appl. Phys. Lett.* **2011,** *99* (12), 121501-3.
115. Sretenovic, G. B.; Krstic, I. B.; KovaCevic, V. V.; Obradovic, B. M.; Kuraica, M. M., Spectroscopic Measurement of Electric Field in Atmospheric-Pressure Plasma Jet Operating in Bullet Mode. *Appl. Phys. Lett.* **2011,** *99* (16), 161502-3.
116. Na, N.; Zhang, C.; Zhao, M.; Zhang, S.; Yang, C.; Fang, X.; Zhang, X., Direct Detection of Explosives on Solid Surfaces by Mass Spectrometry with an Ambient Ion Source Based on Dielectric Barrier Discharge. John Wiley & Sons, Ltd.: 2007; Vol. 42, pp 1079-1085.
117. Na, N.; Zhao, M.; Zhang, S.; Yang, C.; Zhang, X., Development of a Dielectric Barrier Discharge Ion Source for Ambient Mass Spectrometry. *J. Am. Soc. Mass Spectr.* **2007,** *18* (10), 1859-1862.
118. Chan, G. C. Y.; Shelley, J. T.; Wiley, J. S.; Engelhard, C.; Jackson, A. U.; Cooks, R. G.; Hieftje, G. M., Elucidation of Reaction Mechanisms Responsible for Afterglow and Reagent-Ion Formation in the Low-Temperature Plasma Probe Ambient Ionization Source. *Anal. Chem.* **2011,** *83* (10), 3675-3686.
119. Hou, K.; Xu, W.; Xu, J.; Cooks, R. G.; Ouyang, Z., Sampling Wand for an Ion Trap Mass Spectrometer. *Anal. Chem.* **2011,** *83* (5), 1857-1861.
120. Shelley, J. T.; Hieftje, G. M., Ionization Matrix Effects in Plasma-Based Ambient Mass Spectrometry Sources. *J. Anal. At. Spectrom.* **2010,** *25* (3), 345-350.
121. Chan, G. C. Y.; Shelley, J. T.; Jackson, A. U.; Wiley, J. S.; Engelhard, C.; Cooks, R. G.; Hieftje, G. M., Spectroscopic Plasma Diagnostics on a Low-Temperature Plasma Probe for Ambient Mass Spectrometry. *J. Anal. At. Spectrom.* **2011,** *26* (7), 1434-1444.
122. Michels, A.; Tombrink, S.; Vautz, W.; Miclea, M.; Franzke, J., Spectroscopic Characterization of a Microplasma Used as Ionization Source for Ion Mobility Spectrometry. *Spectrochim. Acta B* **2007,** *62* (11), 1208-1215.
123. Olenici-Craciunescu, S. B.; Michels, A.; Meyer, C.; Heming, R.; Tombrink, S.; Vautz, W.; Franzke, J., Characterization of a Capillary Dielectric Barrier Plasma Jet for Use as a Soft Ionization Source by Optical Emission and Ion Mobility Spectrometry. *Spectroc. Acta Pt. B-Atom. Spectr.* **2009,** *64* (11-12), 1253-1258.
124. Nyadong, L.; Harris, G. A.; Balayssac, S. p.; Galhena, A. S.; Malet-Martino, M.; Martino, R.; Parry, R. M.; Wang, M. D.; FernaÌ • ndez, F. M.; Gilard, V. r., Combining Two-Dimensional Diffusion-Ordered Nuclear Magnetic Resonance Spectroscopy, Imaging Desorption Electrospray Ionization Mass Spectrometry, and Direct Analysis in Real-Time Mass Spectrometry for the Integral Investigation of Counterfeit Pharmaceuticals. *Anal. Chem.* **2009,** *81* (12), 4803-4812.

125. Cajka, T.; Vaclavik, L.; Riddellova, K.; Hajslova, J., GC-TOF-MS and DART-TOF-MS: Challenges in the Analysis of Soft Drinks. In *LC-GC Europe*, Advanstar Communications: 2008; Vol. 21, pp 250-256.
126. Bolden, R. C.; Twiddy, N. D., A Flowing Afterglow Study of Water Vapour. *Faraday Discuss. Chem. S.* **1972,** *53*, 192-200.
127. Raju, G. G., *Gaeous Electronics*. CRC Press, Taylor & Francis Group, LLC: 2006.
128. Dzidic, I.; Carroll, D. I.; Stillwell, R. N.; Horning, E. C., Comparison of Positive Ions Formed in Nickel-63 and Corona Discharge Ion Sources Using Nitrogen, Argon, Isobutane, Ammonia and Nitric Oxide as Reagents in Atmospheric Pressure Ionization Mass Spectrometry. *Anal. Chem.* **1976,** *48* (12), 1763-1768.
129. Kambara, H.; Mitsui, Y.; Kanomata, I., Identification of Clusters Produced in an Atmospheric Pressure Ionization Process by a Collisional Dissociation Method. *Anal. Chem.* **1979,** *51* (9), 1447-1452.
130. Heywood, M. S.; Taylor, N.; Farnsworth, P. B., Measurement of Helium Metastable Atom Densities in a Plasma-Based Ambient Ionization Source. *Anal. Chem.* **2011,** *83* (17), 6493-6499.
131. Alves, L. L.; Gousset, G.; Ferreira, C. M., A Collisional-Radiative Model for Microwave Discharges in Helium at Low and Intermediate Pressures. *J. Phys. Appl. Phys.* **1992,** *25* (12), 1713.
132. Golubovskii, Y. B.; Maiorov, V. A.; Behnke, J.; Behnke, J. F., Modelling of the Homogeneous Barrier Discharge in Helium at Atmospheric Pressure. *J. Phys. Appl. Phys.* **2003,** *36* (1), 39.
133. Martens, T.; Mihailova, D.; van Dijk, J.; Bogaerts, A., Theoretical Characterization of an Atmospheric Pressure Glow Discharge Used for Analytical Spectrometry. *Anal. Chem.* **2009,** *81* (21), 9096-9108.
134. Bogaerts, A.; Gijbels, R., Hybrid Modeling Network for a Helium--Argon--Copper Hollow Cathode Discharge Used for Laser Applications. *J. Appl. Phys.* **2002,** *92* (11), 6408-6422.
135. Ricard, A.; Décomps, P.; Massines, F., Kinetics of Radiative Species in Helium Pulsed Discharge at Atmospheric Pressure. *Surf. Coat. Tech.* **1999,** *112* (1-3), 1-4.
136. Massines, F.; Ségur, P.; Gherardi, N.; Khamphan, C.; Ricard, A., Physics and Chemistry in a Glow Dielectric Barrier Discharge at Atmospheric Pressure: Diagnostics and Modelling. *Surf. Coat. Tech.* **2003,** *174-175*, 8-14.
137. Anderson, C.; Hur, M.; Zhang, P.; Mangolini, L.; Kortshagen, U., Two-Dimensional Space-Time-Resolved Emission Spectroscopy on Atmospheric Pressure Glows in Helium with Impurities. *J. Appl. Phys.* **2004,** *96* (4), 1835-1839.
138. Olenici-Craciunescu, S. B.; MÃ¼ller, S.; Michels, A.; Horvatic, V.; Vadla, C.; Franzke, J., Spatially Resolved Spectroscopic Measurements of a Dielectric Barrier Discharge Plasma Jet Applicable for Soft Ionization. *Spectrochim. Acta B* **2011,** *66* (3-4), 268-273.
139. Tsuchida, K., Density Measurement of Helium Metastable Atoms in a Plasma by the Laser-Induced Fluorescence Method. *Jpn. J. Appl. Phys.* **1984,** *23*, 338-345.
140. Den Hartog, E. A.; Doughty, D. A.; Lawler, J. E., Laser Optogalvanic and Fluorescence Studies of the Cathode Region of a Glow Discharge. *Phys. Rev. A* **1988,** *38* (5), 2471.
141. Dzierzega, K.; Musiol, K.; Benck, E. C.; Roberts, J. R., Electron Density Measurement in a Rf Helium Plasma by Laser-Collision Induced Fluorescence Method. *J. Appl. Phys.* **1996,** *80* (6), 3196-3201.

142. Barnat, E. V.; Frederickson, K., Two-Dimensional Mapping of Electron Densities and Temperatures Using Laser-Collisional Induced Fluorescence. *Plasma Sources Sci. T.* **2010,** *19* (5), 055015.
143. Nersisyan, G.; Morrow, T.; Graham, W. G., Measurements of Helium Metastable Density in an Atmospheric Pressure Glow Discharge. *Appl. Phys. Lett.* **2004,** *85* (9), 1487-1489.

2 Imaging of He_m Distributions in a Helium Dielectric-Barrier Discharge Ionization Ambient Desorption Ionization Source by Collisionally-Assisted Laser-Induced Fluorescence

2.1 He_m Imaging via Collisionally-Assisted Laser-Induced Fluorescence

The idea that He_m are important in the characterization of a helium plasma-based ADI source was first introduced to me at an American Society for Mass Spectrometry conference in Salt Lake City in May, 2010. At that time, spectroscopic characterization of an LTP probe was presented. The helium emission at 706.519 nm was said to be a radiative transition to a metastable state. Further investigation revealed this to be untrue. The source of the error was also quickly found in an article published by Olenici-Craciunescu et al. in which they claimed prominent helium emission lines represent transitions from different excited states ending on metastable states.[1] Figure 2.1 clearly shows that only one of the typically observed emission lines (1083 nm) ends in a He_m state. However, even emission from this transition gives no good evidence of He_m activity, as discussed in Chapter 1. Although the source of the error may have simply been a misunderstanding or miscommunication in the literature, it is important that clarification be given and the difference between He_m activity and He^* emission be demonstrated for ambient plasma jets. Typically, helium has been favored as the discharge gas for discharge-based ADI sources because of the increase in analyte signal and decreased fragmentation compared to sources that use argon, nitrogen or air as the discharge gas.[2-5]

Although the functionality of helium-based ADI sources is typically attributed to the existence of the He_m species, no work has been done to correlate He_m populations with ADI performance. In the following work, typically observed He^* and N_2^{+*} emission is compared and correlated with He_m fluorescence. The difference between He^* emission and He_m fluorescence is noted and a correlation is made between He_m populations and the performance of the helium dielectric-barrier discharge (He-DBD) as an ADI source.

2.1.1 Collisionally-Assisted LIF Imaging

The ability to image He_m via collisionally-assisted LIF was first brought to my attention by Nick Taylor. Previously, Taylor et al. had demonstrated that, for low-pressure discharge systems containing an inert gas, laser excitation could be efficiently coupled by collisions to levels separated from the upper level in the laser-induced transition by as much as 0.119 eV.[6] This phenomenon has been observed in helium plasmas and used for detection of He_m in past studies.[7-11] In an atmospheric-pressure discharge at elevated temperature, it is expected that the transfer of excitation from a laser-excited level to nearby levels is rapid, and nonresonance laser excitation schemes are particularly efficient. For helium, the difference between the upper ^3P_J and ^3D_J states shown in Figure 2.1 is only 0.067 eV. The small spacing between these levels means that when the $^3S_1$ metastable level is pumped with laser radiation at 388.864 nm, excitation is efficiently transferred from the ^3P_J levels to the ^3D_J levels, and fluorescence can be observed at 587.6 nm. In this process, collisional coupling is efficient enough to produce fluorescence signals comparable to those produced by direct line fluorescence.

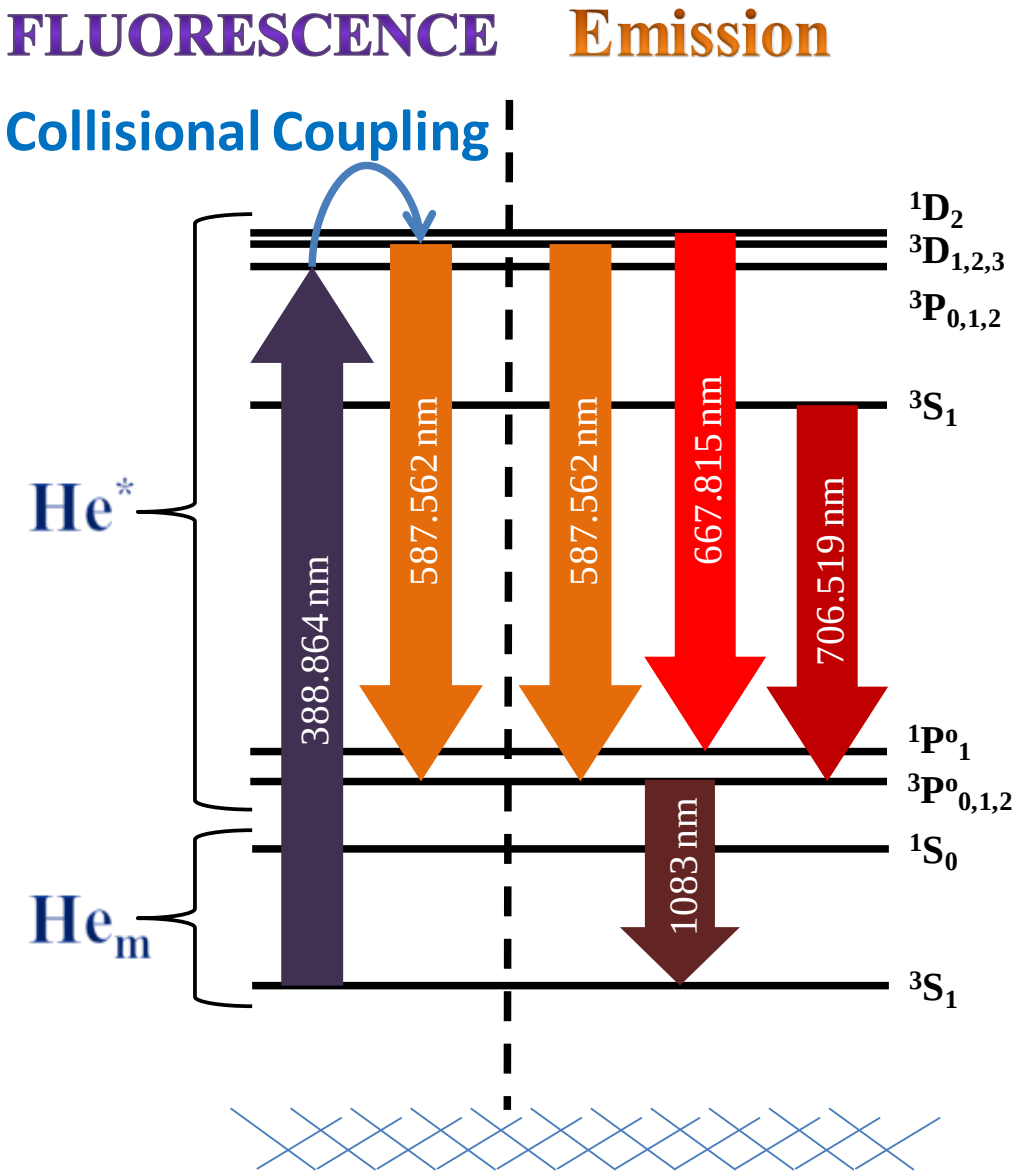

Figure 2.1: Energy level diagram of typically observed helium emission transitions and the collisionally-assisted LIF scheme.

2.2 Experimental Conditions

2.2.1 The Dielectric-Barrier Discharge Atmospheric Pressure Plasma Jet

There are a number of parameters to consider when constructing a DBD APPJ. In order to form a plasma jet, you need an outer electrode, a capillary (through which the discharge gas can flow and in which the discharge can be formed), and a ground electrode. Many combinations of electrode spacing, capillary lengths, and power and frequency settings may be used to form a discharge. The discharge used in my studies was generated in a capillary (3 mm o.d., 1 mm i.d., 80 mm long), between an internal grounded needle electrode and an outer copper electrode (7.3 mm o.d., 3 mm i.d., and 3 mm long). The capillary length that was chosen for the source was mainly a factor of the aluminum mount that was available at the time for mounting the APPJ. Images of the 0^o and 45^o angle mounts are shown in Figure 2.2. The high-voltage ring electrode was placed 10 mm from the tip of the capillary and several mm from the aluminum block. This spacing prevented any arcing of the voltage from the ring electrode to the plasma or to the aluminum mount. The ring electrode was secured to the capillary by a screw, easily seen in Figure 2.2 (a). This screw was also used to attach the high voltage cable by means of an alligator clip as seen in Figure 2.2 (b). The needle electrode was soldered into the back of a 1/8 in. Swagelok cap and the distance between the tip of the needle and the ring electrode was 58 mm. A 1/8 in. Swagelok-T was used to connect the needle, capillary, and helium gas source. A drawing of the discharge is shown in Figure 2.2 (c). Ultrahigh purity helium (99.999%) (Airgas, Radnor, PA, USA.) was used for the discharge, at flow rates up to 2.0 L/min. The flow rate of the helium was controlled by a Brooks 5850C mass flow controller and Brooks 5876 power supply/readout (Brooks Instruments, Hatfield, PA, USA.) or a MKS 1170A mass flow controller and MKS 246C power supply/readout (MKS Instruments, Andover, MA, USA.). Power was

supplied to the discharge with an ENI HPG-2 rf power supply (MKS Instruments, Andover, MA, USA.). The amount of power being applied and the amount of power being coupled into the DBD were read out on the power supply. The difference between the two readings was minimized to select an optimum operating frequency. The frequencies and powers applied to the discharge were monitored with a 500 MHz digital oscilloscope (LeCroy, Chestnut Ridge, NY, USA.)

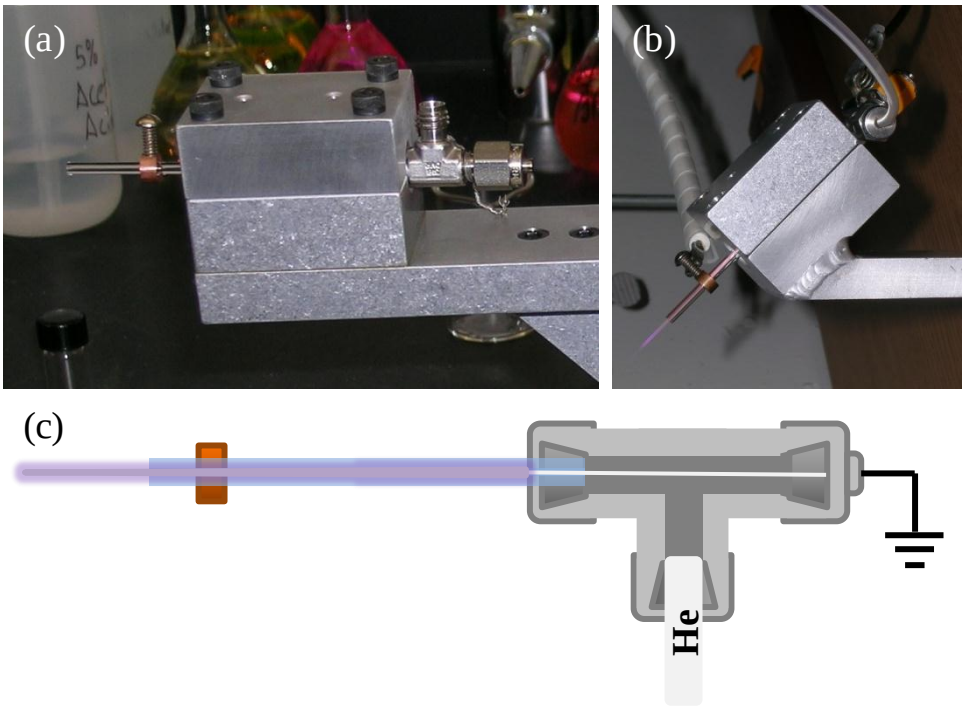

Figure 2.2: Representative images of (a) 0° and (b) 45° angle discharge mounts and a (c) representative cross section drawing of the short-needle DBD APPJ.

Under these conditions, the plasma that was formed filled the entire length of the capillary, from the grounded needle electrode to the downstream end of the capillary and then extended up to 20 mm past the tip of the capillary. An alternative, "long needle" version of the

DBD was also constructed. For the long-needle version of the ionization source, the needle extended the length of the capillary up to the ring electrode, which was placed 7 mm from the tip of the capillary. The plasma that was formed was a smaller discharge in the capillary around the ring electrode. The plasma jet was short, only protruding several millimeters past the tip of the capillary. The smaller power plasma used only about 5 W at a frequency of 300 kHz. The discharge gas flow rate was also decreased to about 200 mL/min. Despite the decrease in power and helium flow rate, the long-needle discharge provided comparable signal with test analytes when used in ADI-MS. The long-needle version also was capable of producing a nitrogen plasma jet that was capable of desorption and ionization of test analytes, but the ADI-MS signal was poor compared to the helium plasma. Although the long-needle version of the discharge had advantages in low power and decreased discharge gas consumption, it was not used in our research for two reasons. Due to the small size of the plasma jet, it was necessary for the plasma to be placed within several millimeters of the sample and MS orifice. Placement farther away than a few millimeters resulted in a loss of signal. Also, because the plasma jet was small it was not convenient for making spectroscopic measurements. In contrast, the short-needle DBD was able to desorb and ionize samples up to several centimeters away, allowing for fewer spatial constrains, and provided a substantial plasma jet more suitable for spectroscopic characterization. For these reasons, the following experiments were performed using the short-needle version of the DBD. Having selected a specific configuration, it was still necessary to determine the power, frequency and flow rate settings that would give us the optimal ADI-MS signal.

2.2.2 ADI-MS

2.2.2.1 Setup

For the determination of optimal parameters for ADI-MS, the APPJ was used for desorption and ionization of coumarin 47 dye solution that was deposited on a glass microscope slide. The slides were held in place in front of the inlet of a Finnigan LCQ Classic mass spectrometer (Thermo Scientific, West Palm Beach, FL, USA.) by means of a custom-built slide mount shown in Figure 2.3. The custom mount allowed for the easy insertion and removal of slides. The plasma was placed at a 41° angle to the glass slide with a distance of 9.5 mm from the capillary tip to the glass surface and 22.5 mm to the MS inlet by means of an x,y,z,θ stage. The signal was monitored by Xcaliber version 2.0 software (Thermo Scientific, West Palm Beach, FL, USA.). Optimal plasma conditions were determined to be those that produced the best ADI-MS signal of coumarin 47 ($[M + H]^+$ = 232 m/z) while allowing for the most efficient coupling of power into the plasma. Optimal power, frequency, and gas flow rate were determined to be 31 W, 350 kHz, and 2 L/min, respectively. For determination of a minimum detectable concentration, slides were spotted with 3 μL of 0.0033 ppm (9.9 pg) coumarin 47 in methanol at 6.5 mm from the MS inlet, with a scanning range of 2 mass units around the $[M + H]^+$ peak. Signals were integrated over a 1 min period.

2.2.2.2 Slide Dipping

While performing multiple ADI-MS experiments, it was necessary to create a method of sample deposition that would allow me to obtain reproducible signal and results. Although spotting the slide with sample via micropipette is an acceptable method of sample deposition, spot placement can lead to variability in the ADI-MS signal. This variability can be overcome by using small sample spots that will be completely removed by desorption. However, when

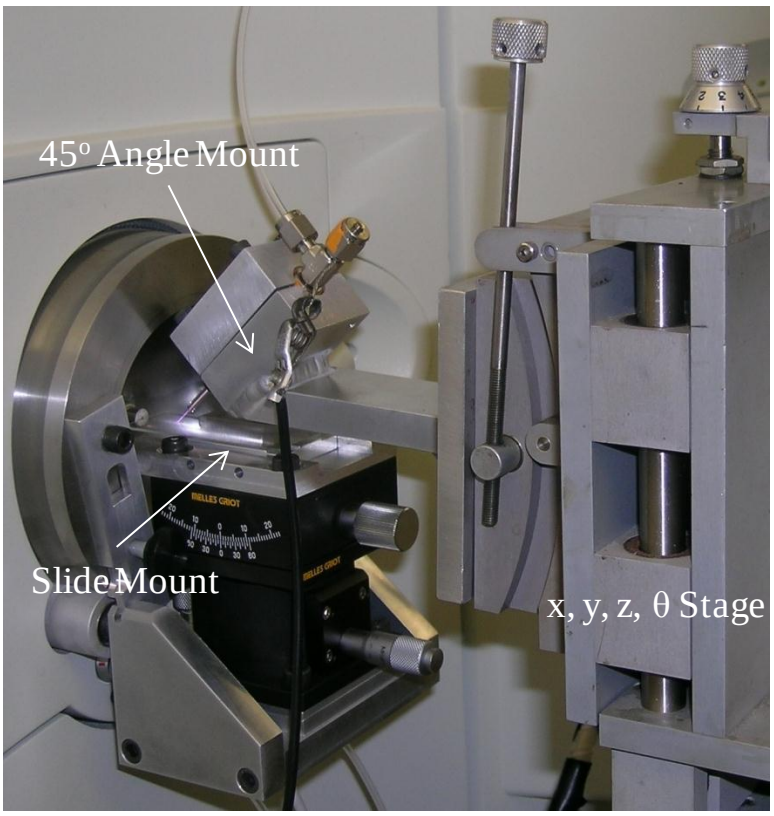

Figure 2.3: ADI-MS setup.

Figure 2.4: Slide dipper and controller software interface.

small sample spots are used, sample is quickly removed and MS signals can be small. For larger spots, analyte tends to build up on the outside of the deposited droplet, creating an inhomogeneous sample spot.

Another way to deposit a sample is by dipping the slide into a solution containing the analyte of choice. If the dipping mechanism happens in a fluid motion, then a homogeneous layer of analyte is deposited over a large region of the slide. This type of sample deposition allows for a more reproducible analyte signal over a period of several minutes, depending on solution concentration. The removal of analyte from a homogeneous deposition, in some cases, also allows for the observation and study of sample desorption. This type of reproducible deposition is only accomplished by automation.

For ADI-MS experiments, slides were dipped using an in-house-constructed slide dipping apparatus. The apparatus consists of a one-dimensional motorized stage and a slide mount. The motorized dipping mechanism is controlled by a National Instruments LabVIEW program. Pictures of the dipper and controller interface are shown in Figure 2.4.

2.2.3 Laser Excitation for Fluorescence Imaging

A XeCl excimer laser (Lambda Physik LPX 210i) operating at 25 Hz was used to pump a dye laser (Lambda Physik Scanmate 2) containing BBQ dye (Exciton, Dayton, OH, USA.) in dioxane. The dye laser was tuned to 388.865 nm for excitation of the He_m–He* transition, as illustrated in Figure 2.1. An excess of 1 mJ/pulse was used, resulting in a complete saturation of the excitation transition. The bandwidth of the laser was approximately 6–10 pm.[12] The dye-laser radiation was focused into a 400-μm-diameter fiber-optic/delay line. The optical delay line was necessary in order to match electronic delays in the iCCD. The laser radiation from the fiber was collimated with a 25.4-mm-diameter spherical lens (f = 50.8 mm) and then focused with a

25.4-mm-diameter cylindrical lens (f = 76.2 mm), which generated a plane of radiation that contained the plasma jet region of the discharge. The discharge was mounted vertically using the 0^o angle mount. The planar radiation was perpendicular to the axis of the imaging optics. A diagram of the experimental setup for obtaining He_m images is shown in Figure 2.5. Background images of plasma emission and laser scatter, collected with the laser detuned to 390 nm, were subtracted from the raw fluorescence images to produce the images presented in this work.

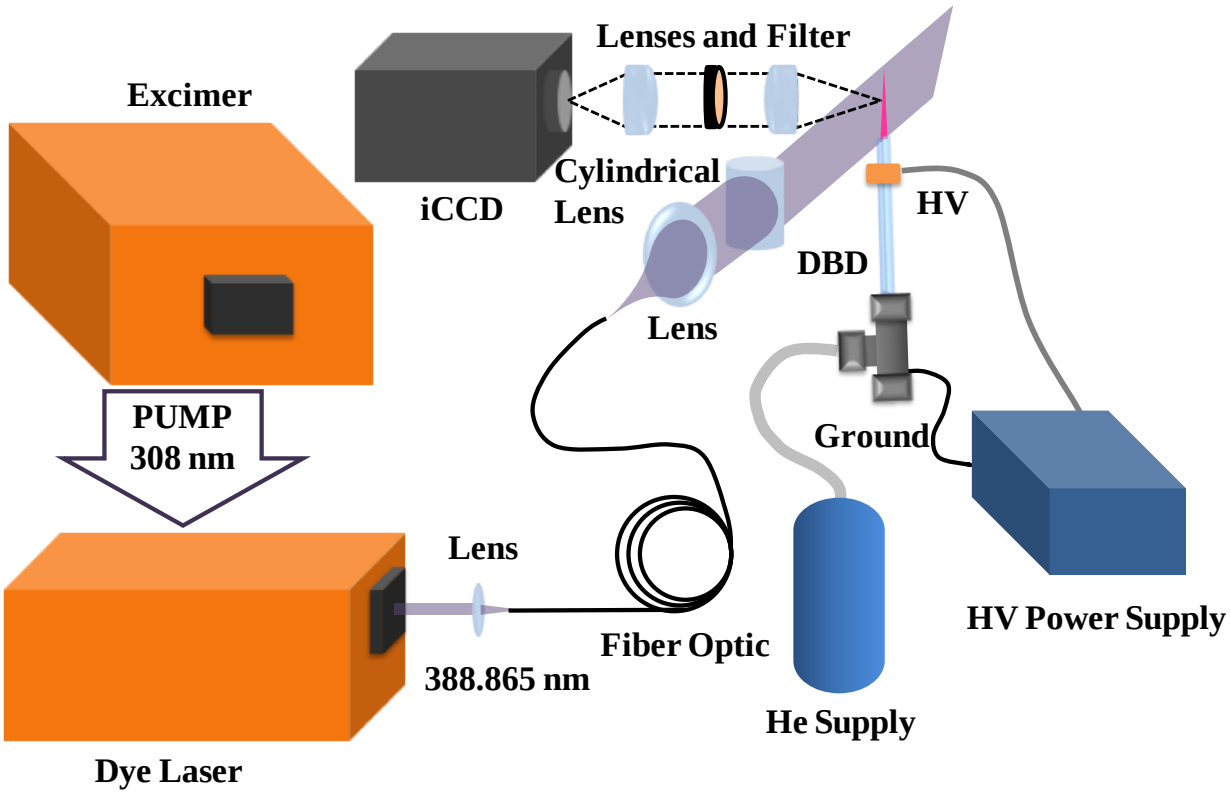

Figure 2.5: Setup for imaging He_m fluorescence and He^* emission.

2.2.4 Collection Optics and iCCD

For side-on imaging of the plasma jet, emission and fluorescence were collected with a pair of matched achromatic doublets having focal lengths of 100 mm and providing unit

magnification. End-on fluorescence imaging was also accomplished by replacing the objective lens with an achromatic doublet with a focal length of 300 mm to create a 3:1 magnified radial image of the discharge. Before imaging, the magnification and scale were determined by taking an image of a reference card. Sample images of the reference card are shown in Figure 2.6. This card gives an accurate reference for conversion of pixels to millimeters.

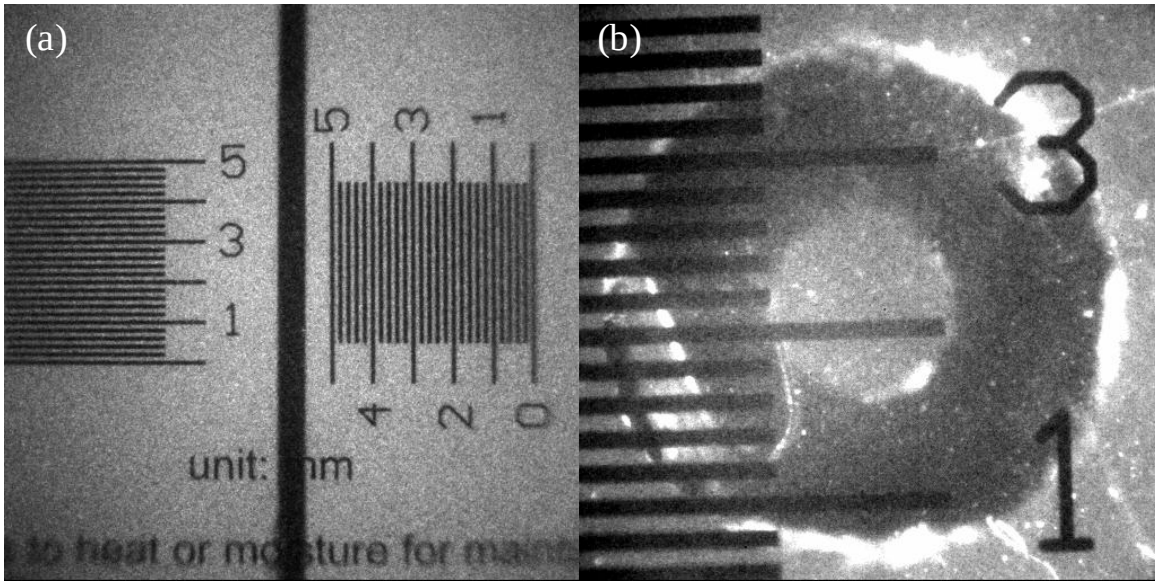

Figure 2.6: Magnification and scale calibration reference images for (a) side-on and (b) end-on imaging.

A Semrock FF01-588/21-25 band-pass filter (Semrock, Rochester, NY, USA.) was placed between the two achromatic doublets for spectral filtering of the emission and fluorescence. The emission and fluorescence were focused onto a PI-MAX intensified charge coupled device (iCCD) (Princeton Instruments, Trenton, NJ, USA.). The iCCD was run at a temperature of -20^{o} C. A diagram of the setup is shown in Figure 2.5. Emission images were collected in shutter mode with images consisting of 250 exposures at 500 μs/exposure. Fluorescence images were taken in gate mode with the gate set to 20 ns and triggered by the laser with a photodiode. Each

fluorescence image was an accumulation of 50 exposures with 100 gates/exposure. All imaging data were collected and processed using Winview 32 software (Princeton Instruments, Trenton, NJ, USA.).

2.2.5 Spectral Imaging of Plasma Jet Emission

Although imaging the plasma jet through a bandpass filter allowed me to obtain spatial distribution images of He_m and He^* species, I did not have a bandpass filter that would allow me to image the spatial distributions of N_2^{+*} in the plasma jet. Therefore, spectral images were taken of the plasma jet at optimal parameters to observe the axial distribution of N_2^{+*}. The plasma emission was collected using a combination of achromatic doublets to produce a 1:3 image of the plasma. The emission was focused on the entrance slit of a Shamrock SR-303i spectrograph (Andor Technology, Belfast, Northern Ireland). A slit width of 25 μm was used to capture the emission from the central 75 μm of the plasma. Emission was dispersed by the grating (1200 lines/mm, 300 nm blaze wavelength) and onto an iDus CCD (Andor Technology, Belfast, Northern Ireland). The CCD was run at a temperature of -80^o C to minimize dark current contributions. Spectral images were taken with an exposure time of 1 s. The images were viewed and recorded using Solis (s) Software (Andor Technology, Belfast, Northern Ireland).

Prior to obtaining spectral images, it was necessary to determine the vertical response of the system. This was accomplished by homogeneously illuminating the entrance slit of the spectrograph with a cuvette full of glow stick solution. Blue, green and red solutions were used to determine the vertical response of the optical system, and generate vertical correction factors for nitrogen ion and helium emission wavelengths. Vertical correction factors were applied to the spectral images to produce the axial cross sections presented in the results below.

2.3 Imaging Results

2.3.1 Images

Side-on He* emission and side-on and end-on He_m fluorescence images were taken at various power, frequency and discharge gas flow rate settings. Representative images, taken of the plasma jet at settings that gave the best ADI-MS signal, and their associated cross sections are shown in Figure 2.7. The position of the capillary tip is indicated by the white dashed line in Figure 2.7 (a) and (b). Some laser scatter is visible off the capillary tip in Figure 2.7 (b). For easy comparison and interpretation of the data provided by the images, cross sections were taken from the central portions of the plasma images. These cross section data will be used for the present discussion.

It should be noted that the data reported here are time averages of a time-varying plasma. In a typical DBD, the discharge is ignited on each cycle of the voltage waveform, and key plasma parameters vary at the frequency of the voltage waveform. However, at 350 kHz, the discharge is quasi-continuous. For my initial measurements, the detection was not synchronized with the voltage waveform that generated the plasma, and the data presented in the figures are averaged in time. To ensure that the assumptions about the temporal character of the plasma were correct, I recorded one set of emission data that were synchronized with the driving voltage. The time-resolved data confirm that the duty cycle of the discharge is high and that reasonable conclusions can be drawn from the averaged data. They also reveal interesting features of the plasma that will be discussed in the next chapter.

Emission images reveal some interesting characteristics of the plasma jet. In Figure 2.8, the effects of the position of the alligator clip on a low power plasma jet are demonstrated. This plasma jet was generated using the long-needle configuration. The long-needle configuration

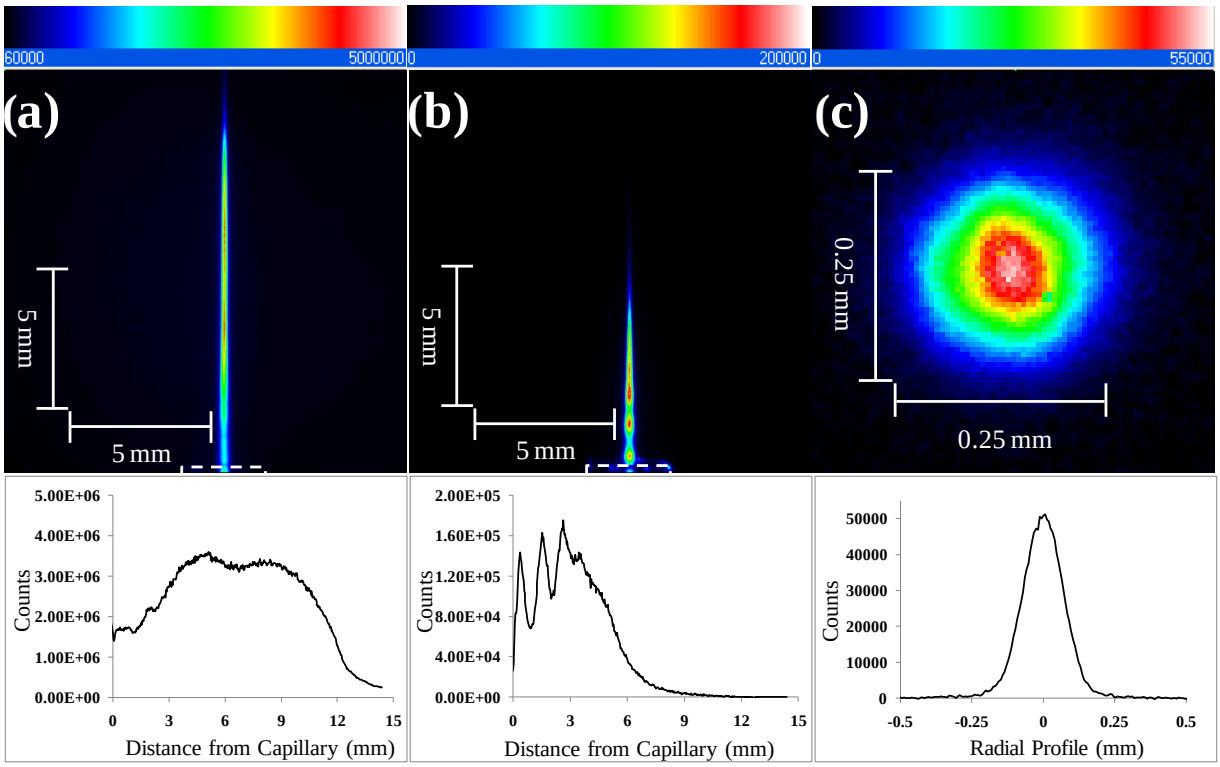

Figure 2.7: Side-on images of (a) He^* emission, and (b) He_m fluorescence, and (c) end-on image of He_m fluorescence at 4 mm downstream from the capillary tip and their associated cross sections. The above images were taken at optimal parameters.

was dramatically more susceptible to the nearby electric field of the electrode as seen in Figure 2.8. This is another reason why the short needle version of the APPJ was preferred.

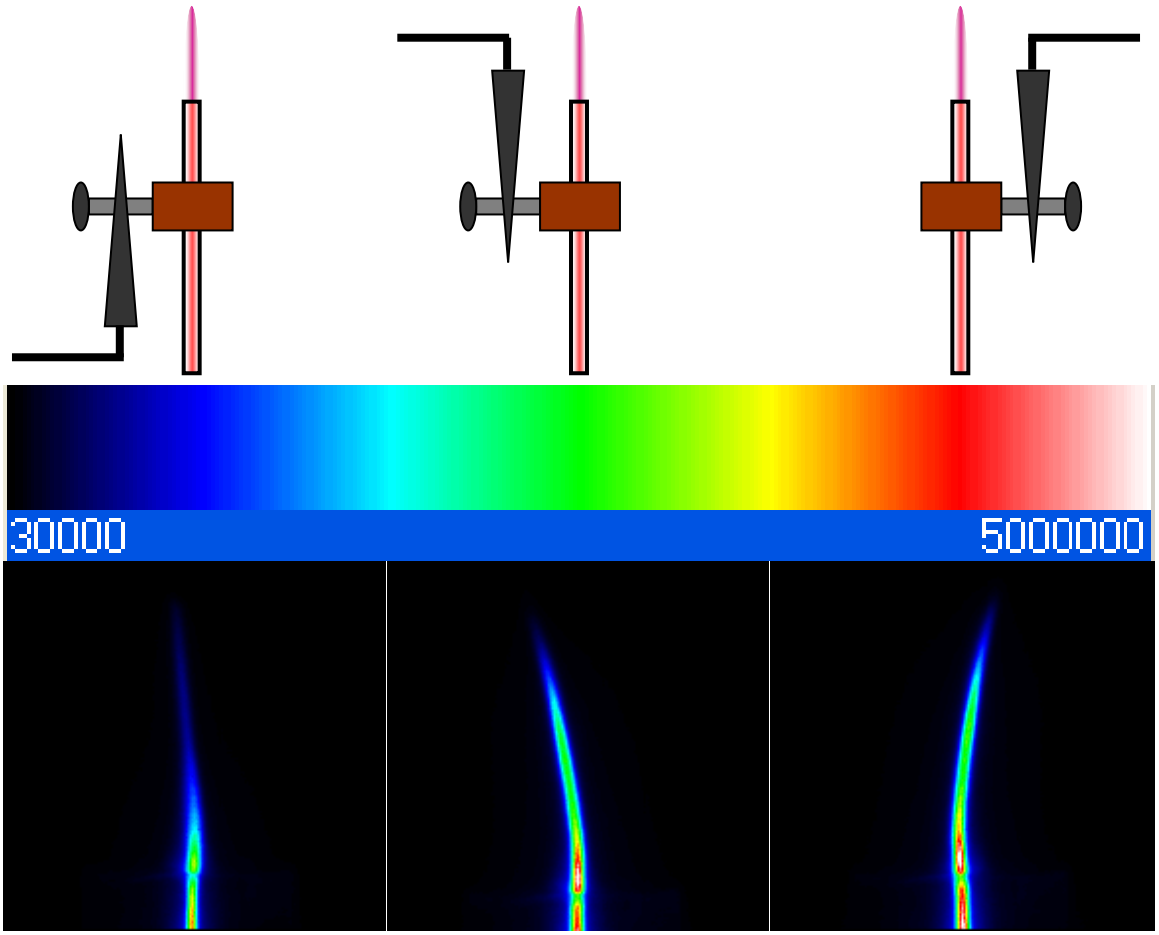

Figure 2.8: Effect of the alligator clip position on a low power, low flow rate plasma jet. Representative schematics of the plasma and alligator clip position are shown above. The resulting He^* emission images are shown beneath.

Other interesting features include the fluctuations in the first 3 mm downstream from the capillary tip seen in Figure 2.7 (b) and in the emission and fluorescence cross sections in Figure 2.9. These fluctuations are stable over the course of a single measurement but are not reproducible from day to day. They are visible by the eye in both the capillary and plasma jet

regions of the discharge. They are most noticeable when the discharge source is being held by the aluminum mount. This observation suggests that the fluctuations are a result of the grounding environment surrounding the discharge. Although they have been mostly eliminated in other work, the nature of these fluctuations has not been fully explored. All other aspects of our data are highly reproducible.

2.3.2 He_m Density Dependence on Power, Frequency, and Flow Rate

The effects of changes in applied power, generator frequency, and He flow rate on emission and fluorescence intensities are illustrated in Figure 2.9. Three parameters were varied individually, with the other two set at the values that gave the best mass spectrometer sensitivity.

There are notable differences between the responses of the fluorescence and emission data to changes in all three parameters. Increases in power result in an unsurprising rise in the overall emission intensity and an extension of the emission farther downstream into the atmosphere. As I will discuss in detail below, the He emission is associated with the recombination of ionic He species, and the rise in emission with increasing power reflects an increase in the ion density. In contrast to the emission data, the fluorescence intensities show little response to changes in plasma power, all falling sharply beyond 4 mm from the tip of the discharge capillary. It is assumed that the gain in excitation of the metastable levels with increasing temperature is offset by increasing losses to ionization. The responses of both the emission and fluorescence intensities to changes in source frequency reflect the fact that the efficiency with which power is coupled into the discharge is a strong function of generator frequency. Coupling of power to the plasma was optimal at a frequency of 350 kHz.

The responses of both emission and fluorescence intensities to changes in He flow rate provide strong evidence that the shapes of both sets of curves are dictated by the interactions of

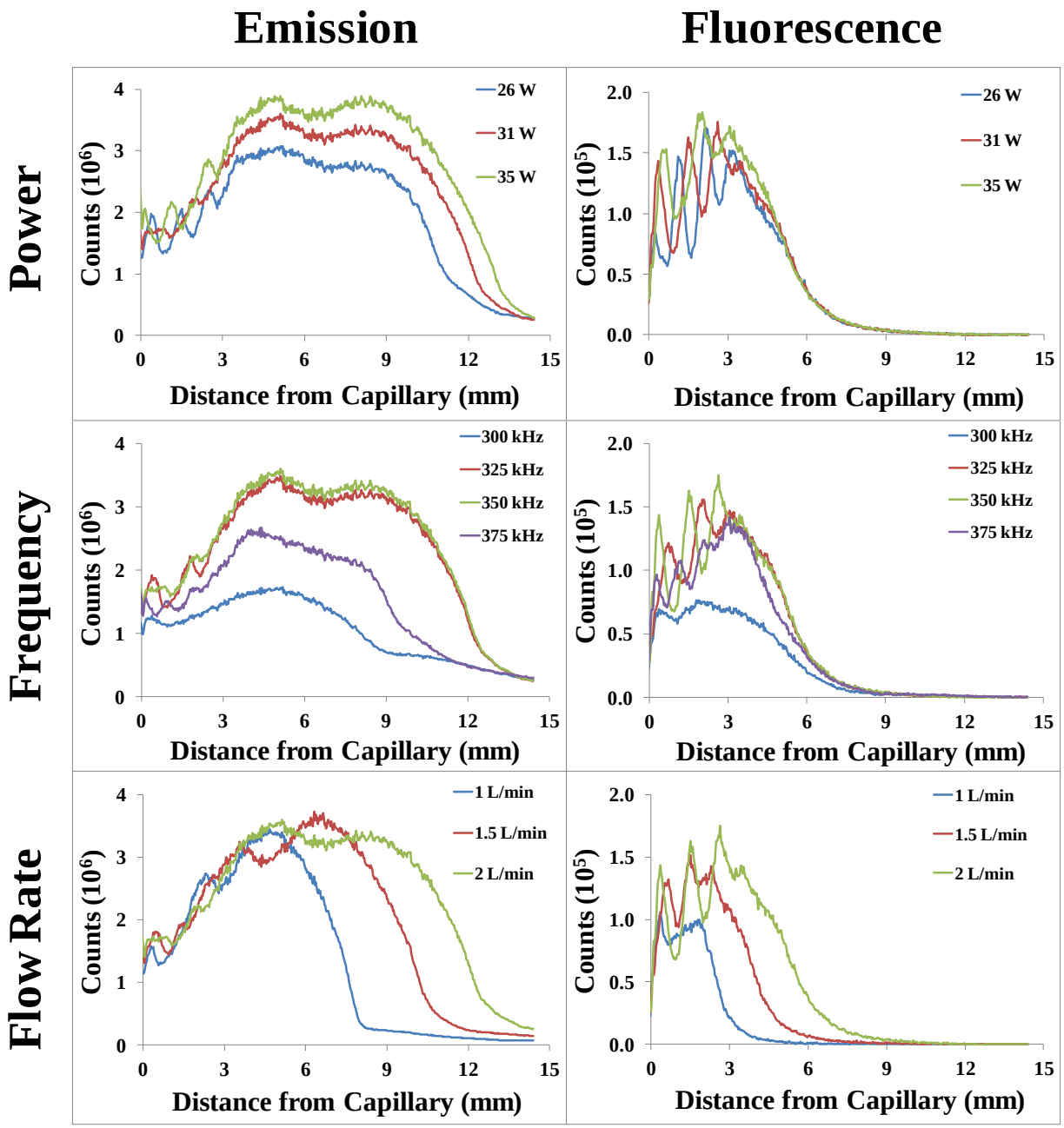

Figure 2.9: Axial variations of plasma emission and fluorescence signals at different powers, frequencies and flow rates.

key species with the air. The data indicate that the sharp drop in He_m densities seen in all curves is a result of quenching of the metastable atoms by atmospheric gases. The most likely candidates for the quenching of the He_m atoms are Penning ionization reactions with N_2, O_2, and H_2O. The Penning cross sections for the He ^3S metastables with these species are 5×10^{-20}, 14×10^{-20}, and 105×10^{-20} m^2, respectively.[13, 14] The relative contributions from the three species will vary with relative humidity, which for an ambient source is an uncontrolled variable. However, even in moist air, quenching of the He_m by nitrogen will dominate because of its high abundance in the atmosphere.

My colleagues and I attribute the He emission primarily to recombination of He atomic or molecular ions with electrons. The time-resolved data clearly indicate that applied voltage is directly affecting the plasma jet region. There may be some direct excitation of the upper He levels by electron impact downstream from the capillary tip. Regardless of the origins of the excited He atoms giving rise to the emission, it is apparent that they are less efficiently quenched by the atmosphere than are the He_m atoms that are monitored by fluorescence. Chan et al. attribute the He emission that they observed in the afterglow of an LTP to ion–electron recombination of He_2^+.[15] The response of the He emission at 587.6 nm to changes in He flow rate suggests that the species responsible for the emission, like the He_m atoms, are quenched by interactions with the atmosphere, albeit to a lesser extent.

2.3.3 Correlation of He_m Fluorescence, He Emission, and N_2^{+*} Emission

The vertical emission profile of N_2^+* at 427.8 nm was obtained by spectral imaging of the plasma. This emission band originates from the excited $B^2\Sigma_u^+$ electronic state, with an internal energy of 18.73 eV.[1] A spatial comparison of the N_2^+ emission with the He_m fluorescence and He 587.6 nm emission is plotted in Figure 2.10. As noted by Chan et al., there are several

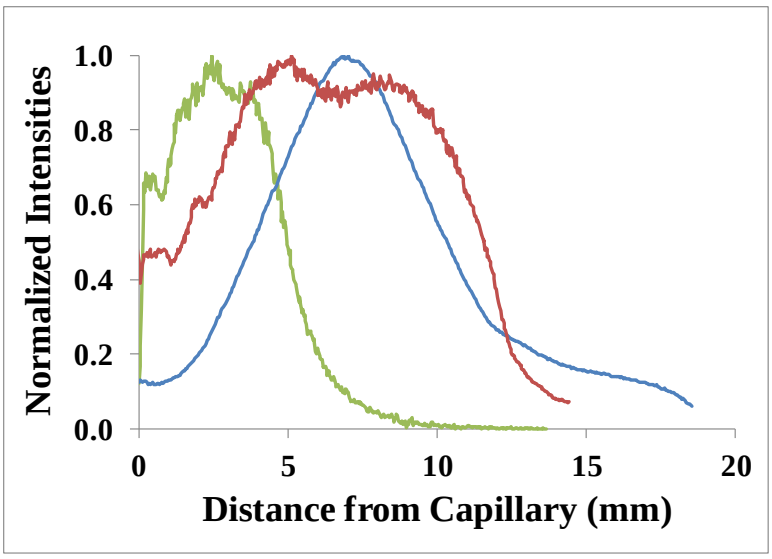

Figure 2.10: Correlation of He_m fluorescence at 587.6 nm (green) with N_2^{+*} emission at 427.8 nm (blue) and He^* emission at 587.6 nm (red).

possible collisions involving energetic helium species that are capable of populating this excited level in the N_2 ion.[15] I will consider only two of them: Penning ionization by He_m and charge transfer with He_2^+. The rapid quenching of the He_m population by the encroaching atmosphere argues that Penning ionization of nitrogen is occurring, and the coincidence of the fall in He_m density with the rise in N_2^+ emission is strong evidence that Penning ionization is contributing to the nitrogen emission. Chan et al. argue that the similarities between the shapes of the He emission profiles and the N_2^+ emission profiles are evidence that charge transfer between $He_2^+$and N_2 is making a significant contribution to the emission from N_2^+. However, unless there is a major source of He_2^+ in the plasma jet, one would expect a pronounced decrease in the emission associated with the recombination of He_2^+ as the ion is consumed by charge-transfer collisions. Instead, there is a second peak in the He emission after the peak emission from N_2^+. It is possible that a second, small peak in the N_2^+ emission is buried under the larger peak and is only evident in the tail on the large peak from N_2^+. A minor contribution of charge transfer between He_2^+ and N_2 to nitrogen ionization is consistent with the data in Figure 2.10.

As models of atmospheric-pressure He discharges are refined, they will provide important insight for the interpretation of the type of experimental data that are reported here. For example, a detailed model of this system, similar to the model recently published by Martens et al.[16] would aid in the interpretation of the axial profiles presented in Figures 2.9 and 2.10. Of course the models are only as good as the fundamental data on which they depend, and publications on helium discharges with nitrogen impurities provide a good example of some of the limitations imposed by uncertain rate constants. The published rate constants for one of the key reactions in this system

$$He_2^+ + N_2 \rightarrow N_2^+ + 2He \qquad 2.1$$

vary by an order of magnitude, even in reports that share a common author, and the version of the reaction used by Martens is energetically impossible.[16-18] The uncertainty in the rate constant for reaction 2.1 is critical, because Martens concludes that reaction 2.1 is the principal source of N_2^+ in an atmospheric-pressure helium discharge flowing into air. Given the uncertainties in rate constant data, I am not concerned that my conclusion about the relative importance of Penning ionization in the production of nitrogen ions disagrees with the prediction of the Martens model. It is a discrepancy that continued experimentation and refinement of the model will undoubtedly resolve.

The fluorescence data show a positive correlation between those parameters that produce the largest helium metastable populations and those that give the best ADI-MS signal. Optimal plasma settings for ADI-MS were around 31 W, 350 kHz, and a He gas flow rate of 2.0 L/min. At these settings, it was possible to detect 9.9 pg of coumarin 47 well above 3 times the noise of the blank. This demonstrates the ability of this source to detect a test analyte in comparable amounts to those detected by similar ionization sources.[5, 19, 20]

2.3.4 Radially-Resolved Fluorescence Images

2.3.4.1 Radial Distributions

Because the He_m fluorescence is excited by a sheet of radiation, it is possible to obtain radially resolved images of He_m distributions at fixed axial points in the plasma. Radial images were taken at 1, 4, and 7 mm downstream from the capillary. The axial resolution of these images was limited by the thickness of the intersecting sheet of radiation. The cross sections for these images are shown in Figure 2.11 (a). The relative magnitudes at the three positions are consistent with the axial cross-sectional data in Figure 2.9. The data reveal a narrowing in the radial distribution of He_m densities downstream from the capillary with full-width half-maximum

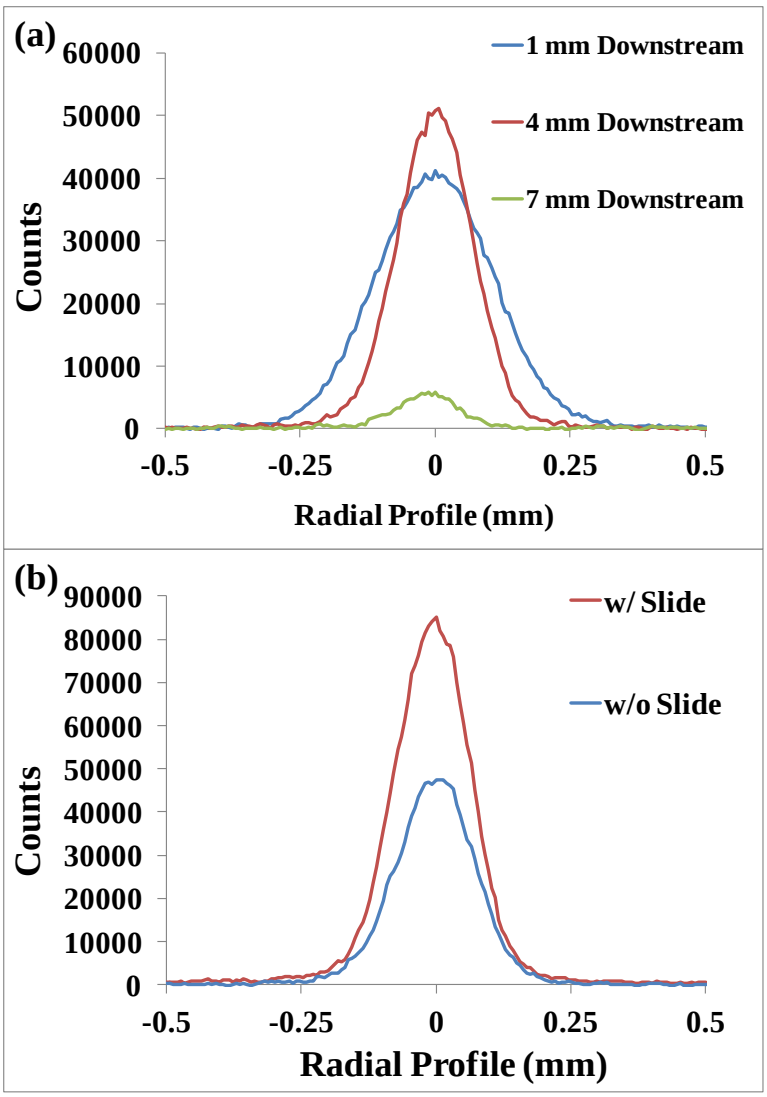

Figure 2.11: (a) Cross sections of radial images of He_m fluorescence at 1, 4, and 7 mm downstream from the capillary tip. (b) Cross sections of radial images of plasma fluorescence at 4 mm downstream from the capillary tip with and without a glass slide.

(fwhm) values of 0.25, 0.16, and 0.14 mm for cross sections taken at 1, 4, and 7 mm downstream, respectively.

2.3.4.2 Addition of a Glass Slide

It is typical in ADI-MS for the discharge source to come in contact with a surface, often a glass slide. It would, therefore, be beneficial to know the influence a glass slide has on discharge conditions. Radially resolved fluorescence images were taken of the discharge 4 mm downstream from the capillary while the glass slide was placed 10 mm downstream from the capillary tip. The plots in Figure 2.11 (b) show a significant increase in He_m population at 4 mm downstream from the capillary due to the presence of a glass slide. The fwhm values of 0.17 mm for both cross sections indicate that there is no broadening or radial redistribution of He_m. It is possible that the enhancement is the result of additional electrical pathway to ground through the glass slide. However, the reasons for the increase in He_m densities caused by the insertion of the slide are not evident from the experiments that have performed to date, but will be the subject of future studies.

2.4 Conclusions

An effective method for mapping He_m in a He-DBD under ambient conditions has been demonstrated using collisionally-assisted LIF. LIF is a powerful tool for understanding the role that He_m plays in the ion source, and it will be effective for the study of other helium-based ADI sources. The experiments presented here point to important differences between the behaviors of He* and He_m species. A limited suite of experiments on a single ion source serve to demonstrate the efficacy of LIF as a diagnostic tool for the study of helium-based ADI sources.

2.5 References

1. Olenici-Craciunescu, S. B.; Michels, A.; Meyer, C.; Heming, R.; Tombrink, S.; Vautz, W.; Franzke, J., Characterization of a capillary dielectric barrier plasma jet for use as a soft ionization source by optical emission and ion mobility spectrometry. *Spectroc. Acta Pt. B-Atom. Spectr.* **2009,** *64* (11-12), 1253-1258.
2. Cody, R. B.; Laramee, J. A.; Durst, H. D., Versatile New Ion Source for the Analysis of Materials in Open Air under Ambient Conditions. *Anal. Chem.* **2005,** *77* (8), 2297-2302.
3. Na, N.; Zhao, M.; Zhang, S.; Yang, C.; Zhang, X., Development of a Dielectric Barrier Discharge Ion Source for Ambient Mass Spectrometry. *J. Am. Soc. Mass Spectr.* **2007,** *18* (10), 1859-1862.
4. Andrade, F. J.; Shelley, J. T.; Wetzel, W. C.; Webb, M. R.; Gamez, G.; Ray, S. J.; Hieftje, G. M., Atmospheric Pressure Chemical Ionization Source. 1. Ionization of Compounds in the Gas Phase. *Anal. Chem.* **2008,** *80* (8), 2646-2653.
5. Harper, J. D.; Charipar, N. A.; Mulligan, C. C.; Zhang, X.; Cooks, R. G.; Ouyang, Z., Low-Temperature Plasma Probe for Ambient Desorption Ionization. *Anal. Chem.* **2008,** *80* (23), 9097-9104.
6. Taylor, N.; Omenetto, N.; Smith, B. W.; Winefordner, J. D., Lifetime Measurements of Several S, P, and D States of Thallium in a Glow Discharge by Single-Step and Two-Step Laser-Excited Fluorescence. *Appl. Spectrosc.* **2008,** *62*, 78-85.
7. Tsuchida, K., Density Measurement of Helium Metastable Atoms in a Plasma by the Laser-Induced Fluorescence Method. *Jpn. J. Appl. Phys.* **1984,** *23*, 338-345.
8. Den Hartog, E. A.; Doughty, D. A.; Lawler, J. E., Laser optogalvanic and fluorescence studies of the cathode region of a glow discharge. *Phys. Rev. A* **1988,** *38* (5), 2471.
9. Dzierzega, K.; Musiol, K.; Benck, E. C.; Roberts, J. R., Electron density measurement in a rf helium plasma by laser-collision induced fluorescence method. *J. Appl. Phys.* **1996,** *80* (6), 3196-3201.
10. Nersisyan, G.; Morrow, T.; Graham, W. G., Measurements of helium metastable density in an atmospheric pressure glow discharge. *Appl. Phys. Lett.* **2004,** *85* (9), 1487-1489.
11. Barnat, E. V.; Frederickson, K., Two-dimensional mapping of electron densities and temperatures using laser-collisional induced fluorescence. *Plasma Sources Sci. T.* **2010,** *19* (5), 055015.
12. Taylor, N.; Omenetto, N.; Smith, B. W.; Winefordner, J. D., Time-resolved laser-induced saturated fluorescence measurements in a thallium see-through hollow cathode discharge: Evaluation of ground state number density and quantum efficiency. *J. Quant. Spectrosc Ra.* **2008,** *109* (15), 2561-2578.
13. Bolden, R. C.; Twiddy, N. D., A flowing afterglow study of water vapour. *Faraday Discuss. Chem. S.* **1972,** *53*, 192-200.
14. Raju, G. G., *Gaeous Electronics*. CRC Press, Taylor & Francis Group, LLC: 2006.
15. Chan, G. C. Y.; Shelley, J. T.; Wiley, J. S.; Engelhard, C.; Jackson, A. U.; Cooks, R. G.; Hieftje, G. M., Elucidation of Reaction Mechanisms Responsible for Afterglow and Reagent-Ion Formation in the Low-Temperature Plasma Probe Ambient Ionization Source. *Anal. Chem.* **2011,** *83* (10), 3675-3686.
16. Martens, T.; Mihailova, D.; van Dijk, J.; Bogaerts, A., Theoretical Characterization of an Atmospheric Pressure Glow Discharge Used for Analytical Spectrometry. *Anal. Chem.* **2009,** *81* (21), 9096-9108.

17. Fehsenfeld, F. C.; Schmeltekopf, A. L.; Goldan, P. D.; Schiff, H. I.; Ferguson, E. E., Thermal Energy Ion---Neutral Reaction Rates. I. Some Reactions of Helium Ions. *J. Chem. Phys.* **1966,** *44* (11), 4087-4094.
18. Bohme, D. K.; Adams, N. G.; Mosesman, M.; Dunkin, D. B.; Ferguson, E. E., Flowing Afterglow Studies of the Reactions of the Rare-Gas Molecular Ions He_2^+, Ne_2^+, and Ar_2^+ with Molecules and Rare-Gas Atoms. *J. Chem. Phys.* **1970,** *52* (10), 5094-5101.
19. Jackson, A. U.; Garcia-Reyes, J. F.; Harper, J. D.; Wiley, J. S.; Molina-Diaz, A.; Ouyang, Z.; Graham Cooks, R., Analysis of drugs of abuse in biofluids by low temperature plasma (LTP) ionization mass spectrometry. *Analyst* **2010,** *135* (5), 927-933.
20. Wiley, J. S.; Garcia-Reyes, J. F.; Harper, J. D.; Charipar, N. A.; Zheng, O.; Cooks, R. G., Screening of agrochemicals in foodstuffs using low-temperature plasma (LTP) ambient ionization mass spectrometry. *Analyst* **2010,** *135*, 971-979.

3 Temporally and Spectrally Resolved Fluorescence and Emission Imaging of Key Reaction Species in a Dielectric-Barrier Discharge Ambient Ionization Source

3.1 Introduction

Much of the previous literature on helium-based ambient plasma jets ascribes the major role in N_2 ionization in atmospheric pressure plasmas to Penning Ionization by He_m.[1-8] Most recently, Chan et al. gave evidence of Penning ionization of N_2 by He_m in an LTP by measuring rotational temperatures of OH and N_2^+, but also discussed the possibility of a second process based on a charge transfer mechanism.[9] In the plasma physics community, discussions regarding temporally and spatially resolved emission measurements of ambient plasma jets have been in favor of the Penning ionization mechanism.[6-8] In Dr. Farnsworth's lab, spatial distributions of He_m populations were obtained by collisionally-assisted laser-induced fluorescence.[10] In that work, my colleagues and I correlated the performance of a DBD ionization source with He_m population in an ambient DBD plasma jet. A positive correlation was found between an increase in the He_m population and ADI-MS signal. Time-averaged spectral images of nitrogen ion emission lines were also obtained, allowing me to make a correlation between He_m and N_2^+ distributions in the plasma, supporting the conclusion that Penning ionization plays a prominent role in the discharge.

Although time-averaged data give compelling evidence of plasma processes, they can only give information about average distributions of key species in the plasma. Time-resolved data, however, show when certain species exist and give information about plasma processes as they relate to the time-dependent nature of the DBD plasma jet and key plasma reactions. Xiong et al. have taken temporally resolved emission measurements of an ambient helium plasma jet that provide a compelling discussion of Penning ionization and electron impact processes.[6] Time-

resolved emission data provided insights into plasma behavior that were missing in time-averaged data. In other work, Urabe et al. looked at He_m and N_2^+ distributions in a DBD with time resolution, using laser absorption and laser-induced fluorescence techniques.[7] However, in those studies, theoretical simulations, and unusual waveforms and plasma parameters were used, and the results presented were not directly applicable to the current research. In the work described in this chapter, time-resolved spectral imaging is used with laser-induced fluorescence to observe key species in a DBD ionization source as the next step to understanding plasma processes that lead to analyte ionization. He_m fluorescence images along with emission images from several nitrogen and helium species are presented once again, this time using time-resolved spectral imaging. Time-resolved axial profiles extracted from spectral images of N_2^+ fluorescence are also presented, providing me with time-resolved, axial distributions of the critical N_2^+ species in the plasma.

3.2 Experimental Section

3.2.1 Improvements in the Setup

In previous experiments, the slide and DBD source were held by aluminum mounts, and controlled using a rather bulky x-y-z-θ stage. These mounts contributed to undesirable spatial constraints that limited the range of motion for the positioning of the DBD source. Also, the aluminum mounts affected the grounding environment of the DBD, causing fluctuations in the discharge that were undesirable when taking spectroscopic images.

In order to improve range of motion and position control, and eliminate unwanted plasma phenomena, new stages were ordered, and new mounts were made by the precision machining lab (PML). The new components from the PML were made of a nonconductive material (Delrin), which helped in the elimination of fluctuations in the plasma jet. The new stages

allowed for easier motion control, larger range of motion for positioning the DBD source, and accurate measurement of plasma angles. Drawings of the custom parts and a picture of the new ADI-MS setup is shown in Figure 3.1.

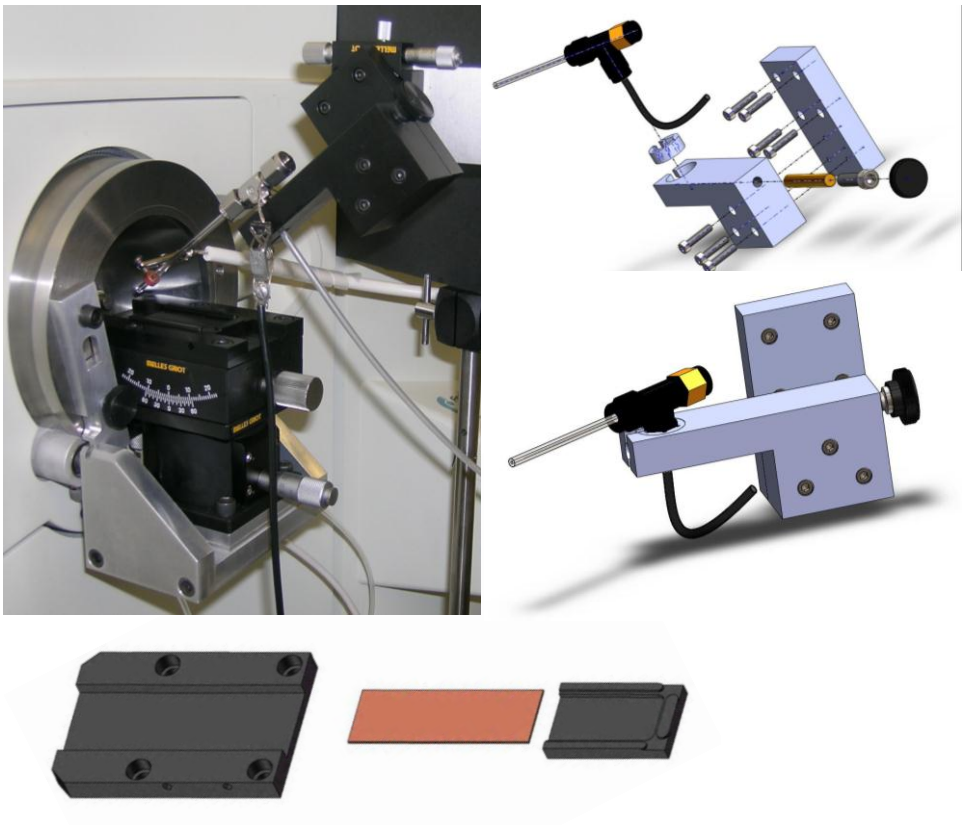

Figure 3.1: Images and drawings of the Delrin slide and DBD source mounts.

Although ADI-MS experiments are not included in the current discussion, the improvements in the ADI-MS setup carried over to the spectroscopic setup. A new Delrin mount was also made for the vertical orientation of the DBD source during spectral imaging experiments. A drawing of the vertical Delrin mount is shown in Figure 3.2. These new mounts incorporate a "pistol grip," which allows for the mounting of most sources using a 1/8 in. Swagelok helium gas inlet.

The improvements in the DBD mount allowed me to make changes to the source. Variations in source design are explained in the following section.

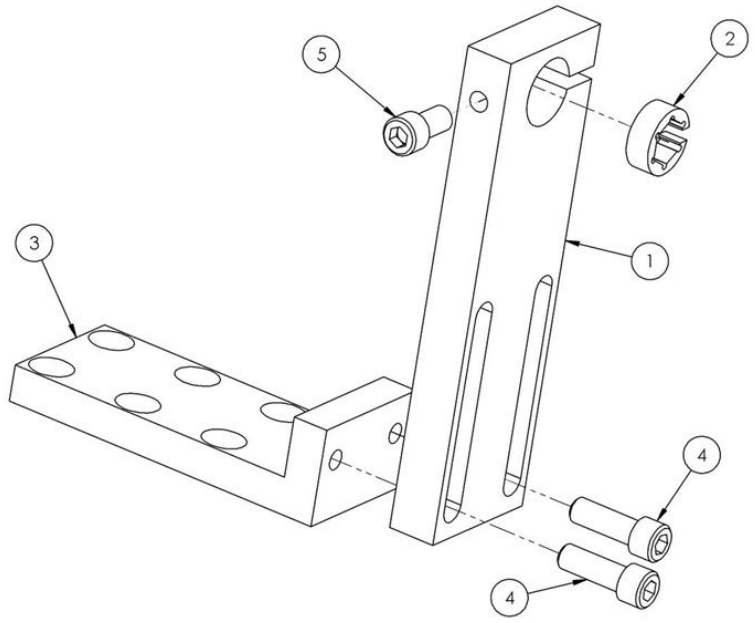

Figure 3.2: Drawing of the Delrin vertical mount.

3.2.2 Helium Dielectric-Barrier Discharge

Removal of the aluminum mounts allowed my colleagues and me to make slight alterations to the DBD source, making it more compact, and also allowing for lower power consumption. The new source was similar to the one previously described, however, a brief description is given for reference. The source consisted of a quartz capillary (3 mm o.d., 1 mm i.d., 60 mm long), an internal grounded needle electrode and an outer copper electrode (7.3 mm o.d., 3 mm i.d., and 3 mm long). The ring electrode was placed 1 cm from the tip of the capillary, and the distance between the two electrodes was 38 mm. The discharge was formed between the ring and needle electrodes. A 1/8 in Swagelok-T was used to connect the capillary, needle, and

helium gas source. Ultrahigh purity helium (99.999%) (Airgas, Radnor, PA, USA.) was used as the discharge gas at a flow rate of 2.0 L/min. The flow rate of the helium was controlled by a MKS 1170A mass flow controller and MKS 246C power supply/readout (MKS Instruments, Andover, MA, USA.). A power of 25 W was supplied to the discharge with an ENI HPG-2 rf power supply (MKS Instruments, Andover, MA, USA.). The rf frequency of about 328 kHz that was applied to the plasma was monitored with a 500 MHz digital oscilloscope (LeCroy, Chestnut Ridge, NY, USA.).

3.2.3 Timing Electronics

The voltage waveform from the RF power supply was used to trigger the laser and the iCCD for time-resolved fluorescence and emission measurements respectively. It was necessary to adjust the triggering electronics for use of the excimer laser and iCCD at rates less than 328 kHz. To accomplish this, the voltage waveform was used to trigger a pulse from an HP 8116A pulse/function generator (Hewlett Packard), which was gated by another HP 8116A function generator. The gate frequency of the second function generator was adjustable, providing me with the ability to select a desired triggering frequency that was still synchronous to the voltage waveform. The gated pulse from the function generators was then sent to a DG 535 delay generator (Stanford Research Systems, Sunnyvale, CA, USA.) allowing me to select the temporal interval of the waveform at which images would be taken.

3.2.4 Laser Induced Fluorescence

He_m and N_2^+ fluorescence were excited in the plasma using a XeCl excimer laser (Lambda Physik LPX210i) to pump a dye laser (Lambda Physic Scanmate 2) containing BBQ dye (Exciton, Dayton, OH, USA.) in dioxane. There was a slight temporal jitter associated with the triggering of the excimer laser. Several repetition rates were chosen for the excimer laser and

the temporal jitter was monitored. Temporal jitter profiles are shown in Figure 3.3. A repetition rate of 15 Hz was chosen for the excimer laser, resulting in a temporal jitter of 12 ns. This introduced a minimum jitter in the imaging experiments. Although a repetition rate of 20 Hz seemed advantageous, having a comparable jitter and a significant increase in frequency, a large amount of tailing was found below the FWHM in the jitter profile at 20 Hz. For this reason, 15 Hz was preferred.

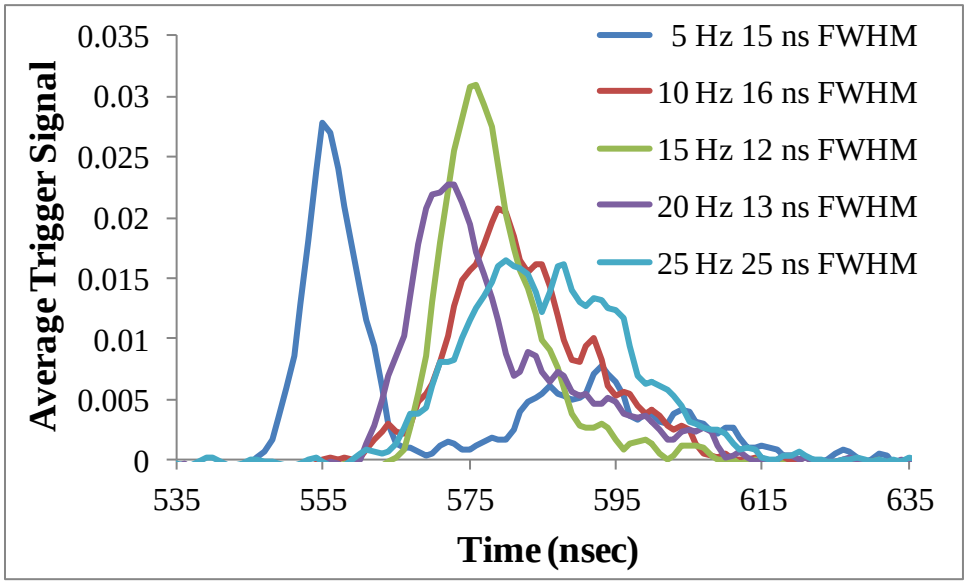

Figure 3.3: Temporal jitter of the excimer laser at various repetition rates.

As explained in previous work, excitation of the He_m-He^* transition was accomplished by tuning the dye laser to 388.865 nm. For the N_2^+ fluorescence, the $B^2\Sigma_u^+$ - $X^2\Sigma_g^+$ transition (v' = 0, v" = 0) was pumped by tuning the dye laser to 391.44 nm, and fluorescence was collected at 427.81 nm (v' = 0, v" = 1). The dye laser radiation was focused into a 400 µm diameter fiber-optic delay line. The optical delay line was necessary to match the electronic delays of the iCCD and facilitated easy delivery of the excitation radiation to the discharge. The laser radiation from

the fiber-optic was collimated with a spherical lens (diameter 25.4 mm, f = 50.8 mm) and then focused to a plane of radiation with a cylindrical lens (diameter 25.4 mm, f = 76.2 mm). The plane of radiation was perpendicular to the collection optics and was adjusted to contain the entire afterglow region of the discharge. The laser radiation was brought as close to the capillary as possible without generating any scatter off the capillary tip. At this point, it was important to determine the homogeneity of the sheet of radiation and how it affected the fluorescence imaging for He_m and N_2^+. The fluorescence response was recorded for He_m and N_2^+, while the sheet of radiation crossed the plasma as in imaging experiments, and then shifted vertically to determine any change in the fluorescence based on the position of the plasma in the laser radiation. Fluorescence profiles for normal and shifted laser induced fluorescence are shown in Figure 3.4. In the case of the He_m fluorescence, the laser was displaced above the tip of the capillary. This causes the sharp rise in the fluorescence signal associated with the position of the laser that is evident in Figure 3.4 (a). The remainder of the curve follows that of the curve associated with the normal position of the laser. For the N_2^+ fluorescence profile, the laser was displaced below the capillary. No dependence on laser position is seen in either plot, indicating that slight inhomogeneities in the planar laser radiation, particularly those at the top and bottom of the plane of radiation, have no significant effect on the fluorescence profiles seen in this work. Background images of plasma emission and laser scatter were taken with the laser detuned to 387 nm for He_m images, and 392 nm for N_2^+ images. Background images were subtracted from the fluorescence images and axial profiles were taken of the spectral images to produce the time-resolved axial profile data presented in this work.

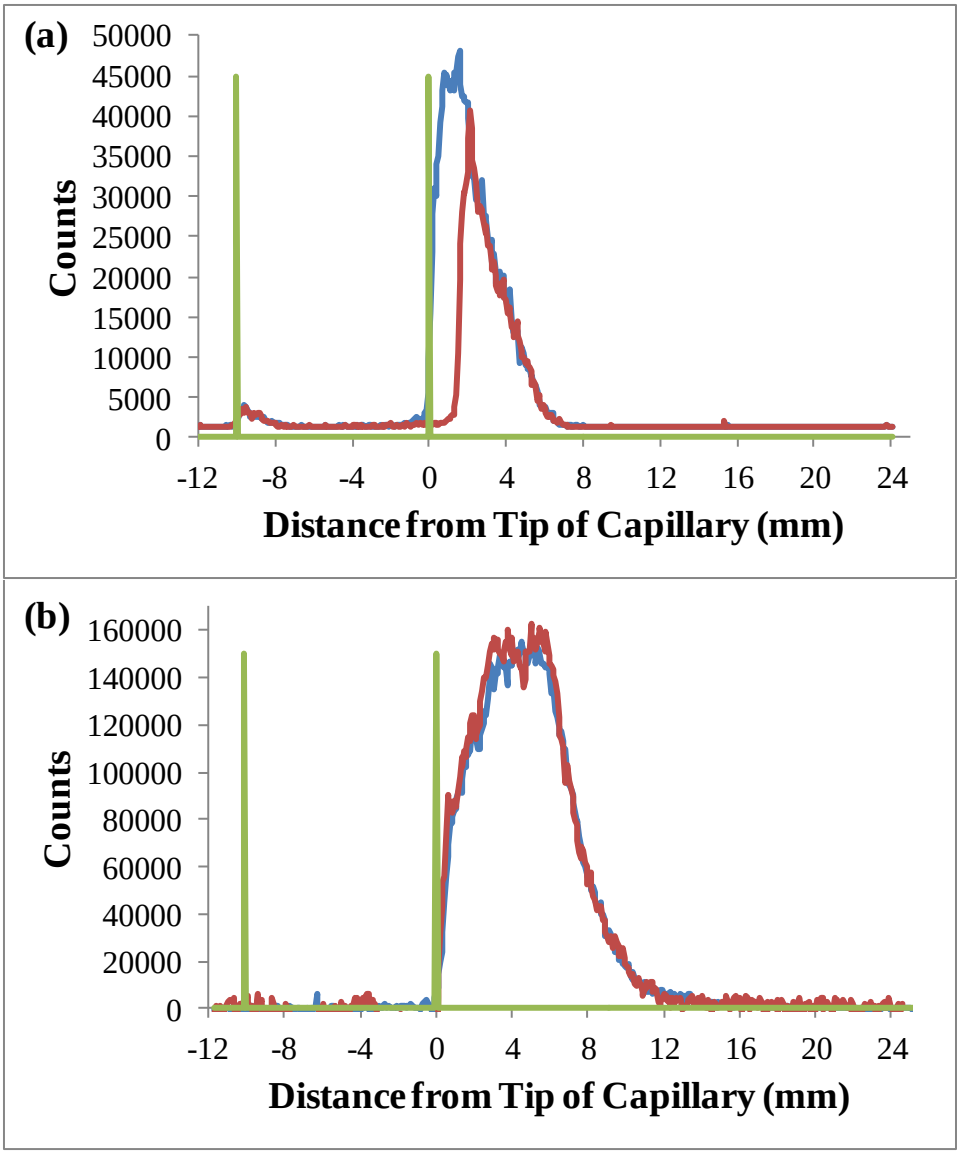

Figure 3.4: Fluorescence profiles of (a) He_m and (b) N_2^+ fluorescence at typical laser position (blue), and displaced laser position (red). The green line represents the position of the ring electrode and the capillary tip.

3.2.5 Time-Resolved Spectral Imaging of He_m and N_2^+ Fluorescence

Discharge fluorescence was collected by a pair of achromatic doublets having focal lengths of 300 mm and 100 mm, providing a 1:3 demagnified image of the discharge. The first achromatic doublet was placed at 90^o with respect to the other and separated by a MM1-311S-25.0 mirror (Semrock, Rochester, NY, USA.). This 90^o arrangement was necessary to fit the optics within the spatial constraints of the setup. The imaging optics were used to image the discharge onto the slits of a McPherson 2061, Czerny Turner monochromator (McPherson, Chelmsford, MA, USA.). Fluorescence wavelengths of 706.519 nm for He_m fluorescence and 427.81 nm for N_2^+ fluorescence were selected using the monochromator, and were focused onto an iCCD (Princeton Instruments, Trenton, NJ, USA.) at the monochromator exit port, generating an axially resolved spectral image of the plasma fluorescence. A second exit port, fitted with a PMT, was used for quick monitoring of fluorescence and emission signals. The signal was gated by a gated integrator/boxcar averager and read out by National Instruments Virtual Bench Scope or Virtual Bench Logger (National Instruments, Austin, TX, USA.).

The time-resolved fluorescence imaging consisted of 31 images, taken across the waveform from trough to trough, every 100 ns. Every fluorescence image was a single accumulation of 1500 exposures, having a gate of 100 ns. The iCCD was triggered at 15 Hz by a photodiode catching scatter from the excimer in the back of the dye laser. The images were viewed, processed and converted to ascii files by Winview 32 software (Princeton Instruments, Trenton, NJ, USA.). Axial profiles were taken of each spectral image by summing the pixels across the spectral line or band head of the emitting species. The number of pixels summed ranges from 9 to 24, producing a spectral width of 168 to 449 pm. Time-resolved data were processed as .ascii files using Matlab software (The MathWorks, Natick, MA, USA.) to produce

motion pictures of time-dependent He_m and N_2^+ fluorescence. Time-averaged images are the result of the summation of all frames from the motion pictures.

3.2.6 Time-Resolved Spectral Images of Plasma Emission

Time-resolved emission images were obtained at a much faster rate than were the fluorescence images because the timing electronics were set to trigger the iCCD at a rate of 3 kHz. The iCCD software was set up to take 31 images across the waveform every 100 ns. Each image consisted of a 100 ns gate, with 30,000 gates per exposure, and 3-5 software accumulations. Time-resolved emission measurements were taken of He^* (706.52 nm), N_2^{+*} (427.81 nm), N_2^* (357. 69 nm), and O^* (777.19 nm). In the case of the O^* emission, there were three lines at 777 nm associated with excited oxygen. The line at 777.19 nm was the most resolved line of the three and was, therefore, used to produce the axial profile for the O^* species. Emission images were processed similarly to the fluorescence images to produce time-resolved and time-averaged axial profiles of discharge emission.

3.3 Results and Discussion

3.3.1 Time-Dependent Plasma Jet

Studies have been done to show the time-dependent nature of plasma jet emission.[11, 12] The observed hypersonic wave of energy, termed "plasma bullet",[11] is said to be the result of an ionization wave.[12] The propagation of the wave of energy is not necessarily the result of the high electric field generated at the electrode, but may be due to an induced local electric field that travels at the head of the bullet.[6] Similarly in my experiments, the plasma is characterized as a traveling wave of energy, moving about 30,000 m/s, much faster than material transport. One period of the waveform is about 3.05 μs long. A representative waveform is given in Figure 3.5.

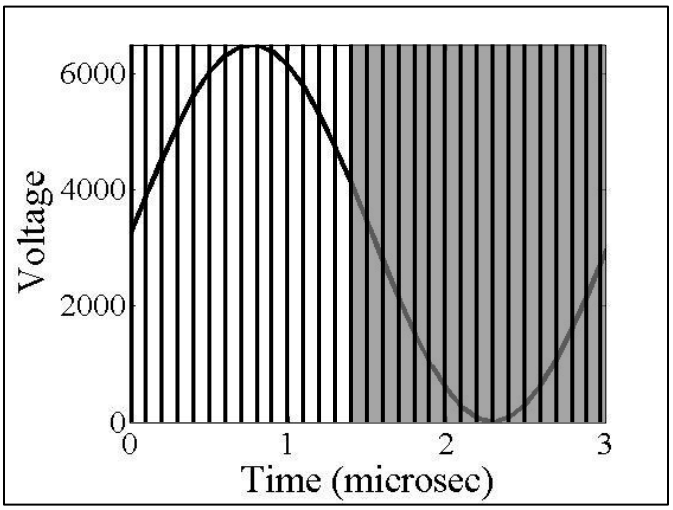

Figure 3.5: Representative image of one period of the voltage waveform.

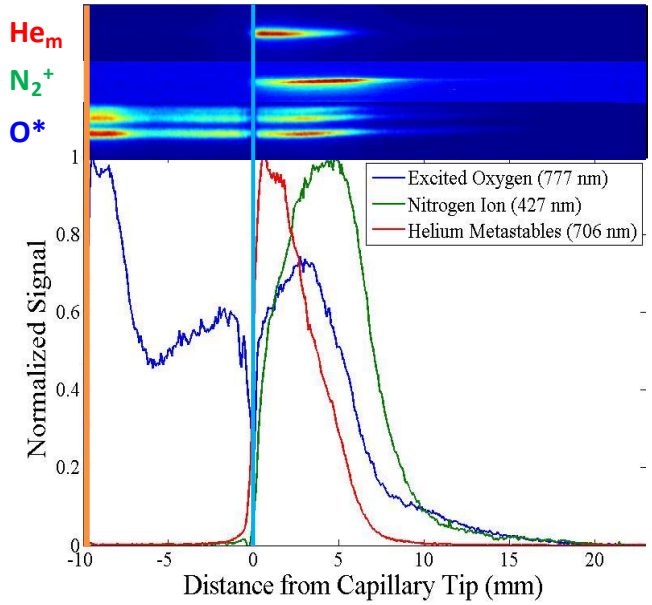

Figure 3.6: Time-averaged spectral images and corresponding axial profiles of He_m and N_2^+ fluorescence, and O^* emission. Lines drawn on the figure at -10 mm and 0 mm mark the position of the copper electrode and tip of the capillary, respectively.

Sections, representing the 31 imaging intervals, are indicated across the waveform. The light portion of the figure indicates the time in the waveform that a plasma bullet is observed beyond the tip of the capillary. Likewise, the shaded portion indicates the "dark" time in the waveform when little or no emission due to the plasma bullet is seen beyond the tip of the capillary. The emission from the plasma bullet beyond the tip of the capillary can last about 1.4 μs, resulting in a duty cycle for the plasma jet of more than 45%.

3.3.2 Time-Resolved Spectral Images of He_m and N_2^+ Fluorescence

Time-averaged images of He_m and N_2^+ fluorescence are presented in Figure 3.6. In previous work, it was shown that He_m fluorescence was generated by collisional coupling between the upper ^3P_J and ^3D_J states, only 0.067 eV separated in energy.[10] From the He_m fluorescence at 706.519 nm shown in these images, it is evident that collisional coupling can occur between the ^3P_J and $^3S_1$ states, with almost 0.3 eV difference in energy. Also, time-averaged images reveal a strong correlation between the decay of the He_m species and the rise of N_2^+ species in the plasma. These data are in agreement with previous studies.[10]

It is clear from the time-resolved frames of the He_m and N_2^+ fluorescence in Figure 3.7 that both species persist during the entire waveform cycle. Helium metastable species are the result of electron impact, which can generate the He_m species or generate He^* and He^+ species, which then undergo recombination and relaxation processes ending at metastable states. Because this excitation is the result of a time-varying application of voltage, a complete decay in He_m population across the waveform would be expected for lower-frequency sources. However, the current power supply cannot generate a discharge at a significantly lower frequency, and the time-dependent nature of He_m populations in low kHz range discharges will remain, for the time being, the subject of future work. Figure 3.7 also shows enhancement of the He_m population by

the wave of energy. Despite the enhancement, it is difficult to sustain a significant distribution of He_m beyond 6 mm from the capillary tip. Frame 16 in Figure 3.7 shows the largest projection of He_m population beyond 6 mm from the capillary tip. This is consistent with our previous observations that He_m are readily quenched by interaction with atmospheric gases like nitrogen, oxygen and water. In time-resolved images, the persistent emission of oxygen from the electrode (-10 mm) until about 6 mm past the capillary tip is also seen. Initially, it was thought that persistent oxygen emission might be more evidence of the interaction between atmospheric gases, however, Figure 3.6 shows that O^* emission is also persistent in the capillary. The dip in the emission profile at 0 mm is an artifact caused by imperfections in the end of the capillary. If the optical distortions generated by the capillary tip were removed, a smooth, consistent upward trend in the oxygen emission would be seen across the capillary boundary until about 4 mm past the capillary tip after which it decays. Figure 3.6 shows no increase in the amount of oxygen emission past the capillary tip that would indicate any significant interaction of He_m with atmospheric oxygen, and the emission that is observed is mainly that of oxygen impurities in the gas tank and lines. The interaction of O_2 with He_m is one mechanism by which O^* can be formed.[6] If the persistent emission of oxygen in the capillary is a result of interaction with He_m species, then the oxygen emission might be a good indicator of He_m populations in the capillary.

The nitrogen ion emission in Figure 3.7 shows that nitrogen ions are formed throughout the entire 20 mm of the plasma by the energy wave. However, the nitrogen ions that persist only remain in the region 1-7 mm beyond the capillary tip after the energy wave has passed. The spatial correlation and similarities in temporal fluctuation and persistence of the N_2^+ fluorescence with that of the He_m seen in Figure 3.7 indicate that these nitrogen ion populations are closely tied to the He_m activity. It is also not likely that a significant part of these ground state ions were

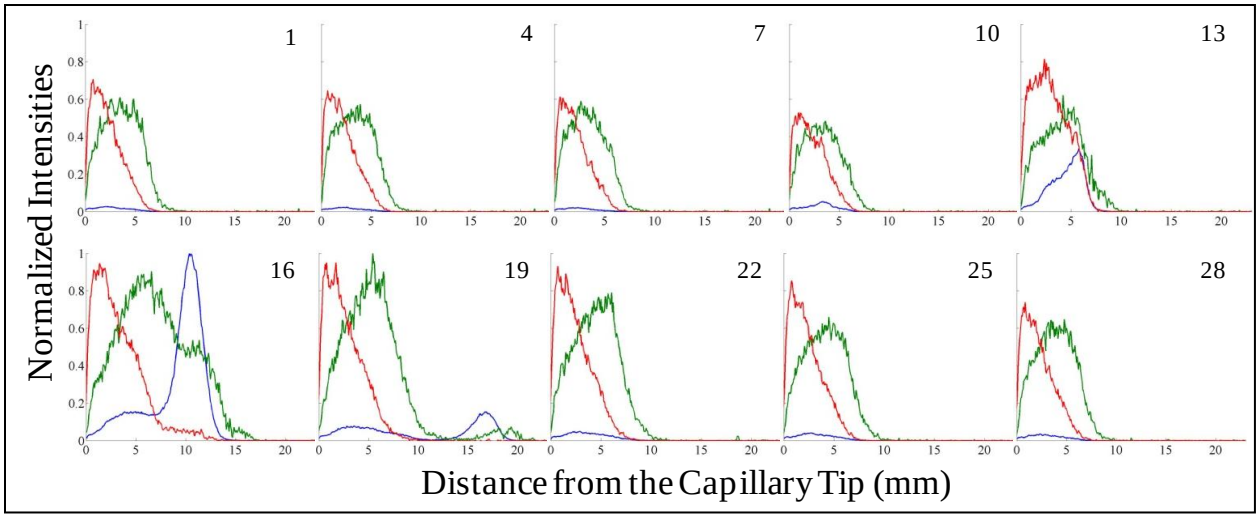

Figure 3.7: Frames taken from a time-resolved motion picture. Frame numbers are indicated in the upper right corner of each frame. Each frame contains axial profiles of He_m (red) and N_2^+ (green) fluorescence and N_2^{+*} emission (blue).

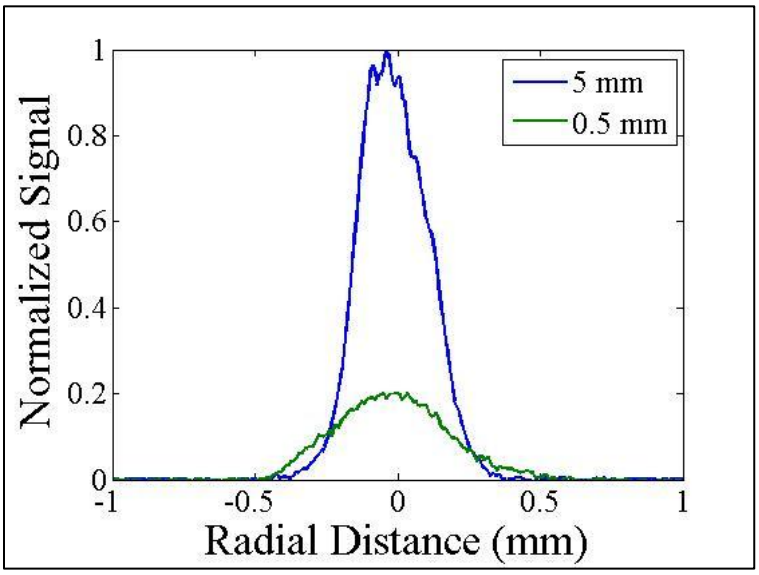

Figure 3.8: Time-averaged radial cross sections of nitrogen ion fluorescence in the plasma jet at 0.5 and 5 mm downstream from the capillary tip.

generated in the capillary or a result of excited nitrogen impurities as the N_2^+ fluorescence signal is small at the capillary tip, and a maximum of nitrogen ion fluorescence is about 5-6 mm removed from the tip of the capillary. This is in contrast to the He_m population, which is generated in the capillary and has a maximum fluorescence signal at the tip of the capillary. To verify this point, radial distributions of nitrogen ion fluorescence in the plasma jet at 0.5 and 5 mm downstream from the capillary tip were taken. The results, shown in Figure 3.8, indicate a significant increase in ground-state nitrogen ion with increasing distance from the capillary tip. Although a portion of the N_2^+ fluorescence may be the result of impurities in the discharge gas, the increase in fluorescence at 5 mm downstream suggests the creation of ground-state nitrogen ion from atmospheric nitrogen. Furthermore, the N_2^+ fluorescence profiles in Figures 3.7 and 3.8 are background subtracted, and show that many of the ions in the ground state are not a result of, or related to, the observed nitrogen ion emission.

3.3.3 Time-Resolved Spectral Images of Time-Dependent Emission

Time-averaged axial emission profiles are provided in Figure 3.9. It is clear that the low power used to produce the blue trace gives rise to a distinct bimodal emission structure, which was seen in previous work for He^* emission, but only suggested for N_2^{+*} emission. This change to a bimodal structure is the result of a lower-power plasma (25 W instead of 31 W). Axial profiles of nitrogen ion emission from the plasma jet are shown for two different powers in Figure 3.9. The higher-power plasma shows a single maximum, similar to the 31 W plasmas in previous experiments.[10] The lower power plasma clearly displays a bimodal structure. Similar bimodal distributions in the optical intensity has been reported for ambient helium plasma jets, but reasons for the double-humped profile were not given.[12] The double nature of the plasma is also seen by the unaided eye, and consists of a diffuse (~600 μm diameter) plasma in the first 0-7

mm of the plasma, which is followed by a more filament-like plasma. This observation has been explained in earlier literature describing atmospheric pressure DBDs. A filamentary portion of the discharge can be the result of gas impurities and the quenching of the He_m state.[13]

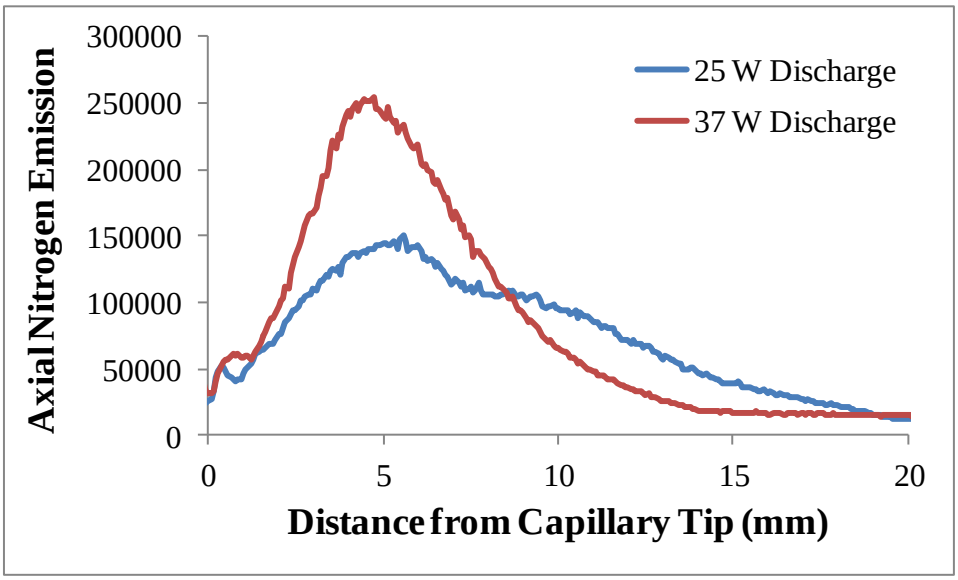

Figure 3.9: Axial profiles of nitrogen ion emission displaying single mode and bimodal plasma jet profiles.

The first 7-mm portion of the He^* and N_2^{+*} emission profiles in Figure 3.10 shows remarkable similarities to the He_m and N_2^+ fluorescence profiles shown in Figure 3.6. The relative spatial distribution of He^*, N_2^{+*}, and N_2^* profiles in the first 7 mm are consistent with those of similar plasmas that have been studied and described in the liturature.[6, 8] The He^* profile shows a maximum near the tip of the capillary and a decay in population starting at about 4 mm. The N_2^{+*} profile shows a maximum starting around 3 mm and a decay in signal starting about 5 mm from the tip of the capillary. The similarities of these first maxima to fluorescence profiles are compelling evidence that the emission in this region has some relation to the existing He_m and ground state N_2^+ species. It is not certain whether the emission is the result of the

excitation of previously existing He_m and ground state N_2^+, or the excited emitting states decay to populate the He_m and ground state N_2^+ states.

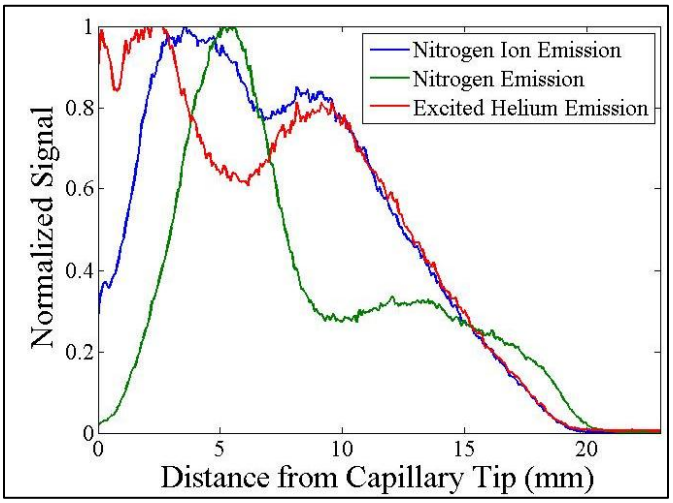

Figure 3.10: Time-averaged axial emission profiles of N_2^{+*} (427.81 nm), N_2^* (357.69 nm), and He^* (706.52 nm) species.

Each emission profile seen in Figure 3.10 also contains a second maximum. The second maxima for He^* and N_2^{+*} emission are at 9.5 mm and have the same decay trend. The second peak of the N_2^* emission has a maximum at around 14 mm which then decays a little farther downstream than the He^* and N_2^{+*} species. Comparison of the emission profiles to the fluorescence profiles suggest that the second maximum is due to a process unrelated to the persistent species seen in the fluorescence profiles. The time-resolved axial emission profiles in Figure 3.11 reveal that the second maximum of the emission is due to a large increase in emission associated with the wave of excitation. Others have attributed the temporary emission to the interaction of plasma species with high-energy or fast electrons (electron impact reactions).[6, 8] The emission in the 6-20 mm region subsides within 200 ns after the passing of the energy wave and does not correlate well with the position of the He_m or the N_2^+ ($X^2\Sigma_g^+$) species.

The emission in the 0-6 mm region, however, persists for several hundreds of nanoseconds. This persistence in emission was also observed by Xiong et al. who attribute the population of the N_2^{+*} state to an electron impact reaction, but assumed the slow decay of the emission was a result of the decay of He_m, which continues to populate the state.[6] The fluorescence profiles in Figure 3.7 show that the ground-state nitrogen ion is continually populated, most certainly, by the He_m species.

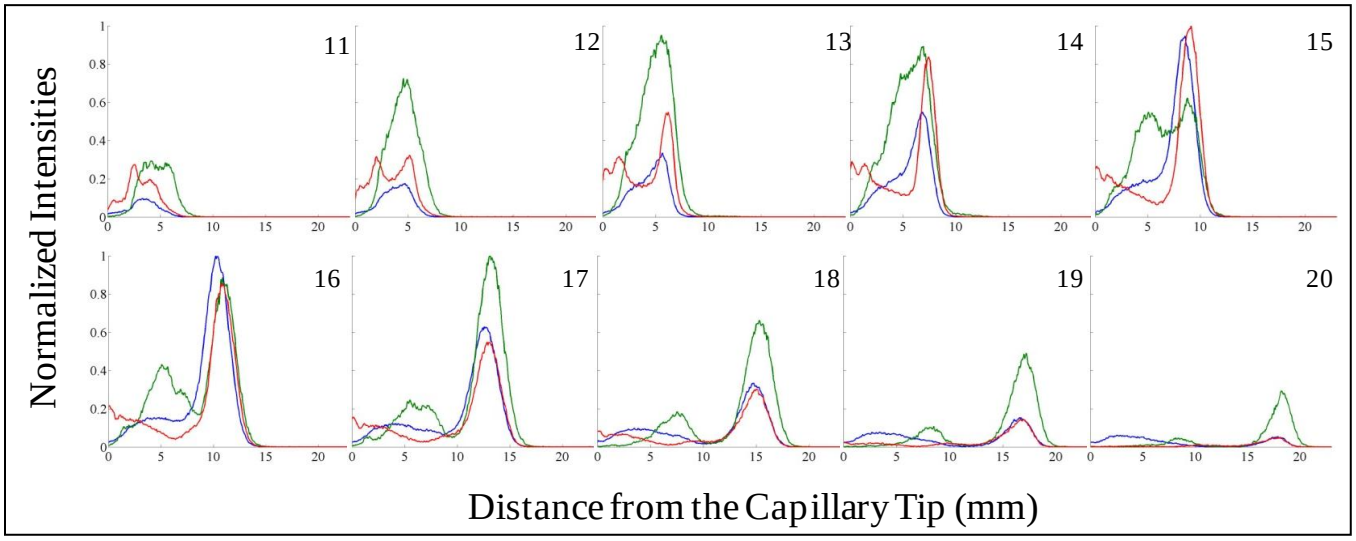

Figure 3.11: Frames 11-20 of time-resolved axial profiles of N_2^{+*} (blue), N_2^{*} (green), and He^{*} (red) emission.

3.3.4 Penning Ionization

The temporal and spatial correlation of the He_m and N_2^{+} fluorescence in Figure 3.7 is good evidence that ground-state nitrogen ions are a result of Penning ionization by He_m. Although ground-state N_2^{+} fluorescence is persistent, it shows little temporal correlation with N_2^{+*} emission beyond 7 mm downstream from the capillary tip. Furthermore, the amount of nitrogen ion emission in the first 7 mm after the capillary tip that persists, after the passing of the

plasma bullet, is relatively low compared to that of the emission associated with the energy wave in the 7 to 20 mm region. Ratios of distribution of nitrogen ion states after Penning ionization by He_m (2^3S) have been shown to favor excited $B^2\Sigma_u^+$ states 41% over X and A states having distributions of 35% and 24%, respectively.[14] However, the lack of N_2^{+*} emission during the second half cycle of the waveform, despite the existence of sustained ground state populations suggests that ionization is generating ions primarily in states other than the $B^2\Sigma_u^+$ state. It is possible that Penning ionization of atmospheric nitrogen is generating nitrogen ion in excited vibrational levels associated with the $X^2\Sigma_g^+$ or $A^2\Pi_u$ states. Unfortunately, the current emission and fluorescence data do not help in determining the actual distribution of nitrogen ion states after ionization. Furthermore, the lifetime of the ground-state nitrogen ion is unknown and may vary with the position in the plasma. More compelling evidence of Penning ionization might be obtained if a correlation could be made between the temporal decay of the He_m and N_2^+ ($X^2\Sigma_g^+$) species. Although a strong correlation is seen over the entire waveform, a decisive correlation cannot be made for the complete decay of the two species due to the high frequency nature of the discharge. Further investigations using low frequency DBD sources will allow for a comparison of the temporal lifetimes of the He_m and N_2^+ ($X^2\Sigma_g^+$) species.

The effect of He_m on nitrogen ion formation is further tested by pumping He_m to an excited state (He^*) and observing the response of the nitrogen ion emission at 427.81 nm. Although a decrease in nitrogen ion emission was expected due to a suppression of Penning ionization, an increase in signal was seen instead. An excitation scan of the $B^2\Sigma_u^+$ - $X^2\Sigma_g^+$ (v' = 0, v" = 0) transition is shown in Figure 3.12. At 388.865 nm, an increase in signal associated with the pumping of the He_m state is observed. It is also evident that this is not nitrogen ion fluorescence associated with the rotational band seen in the figure.

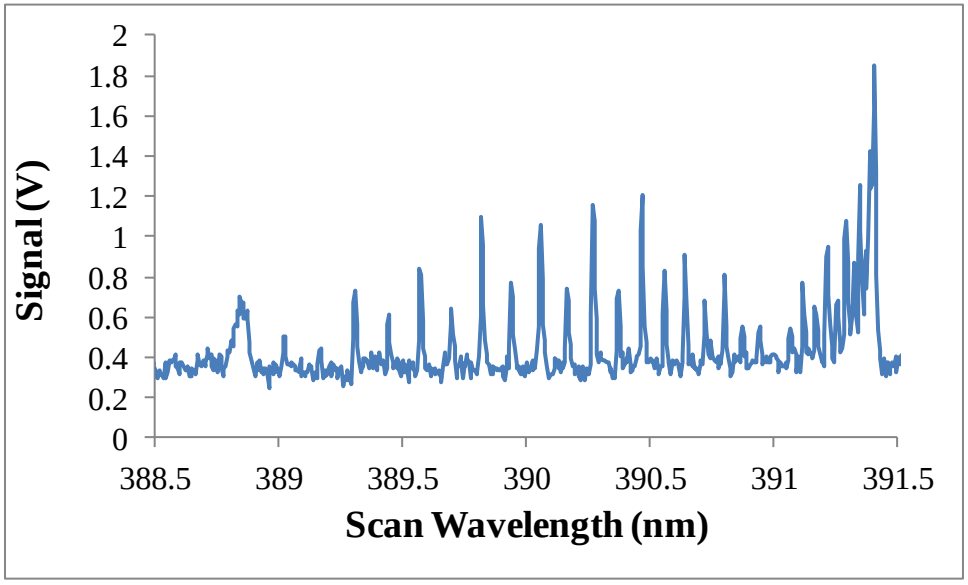

Figure 3.12: Excitation scan of N_2^+.

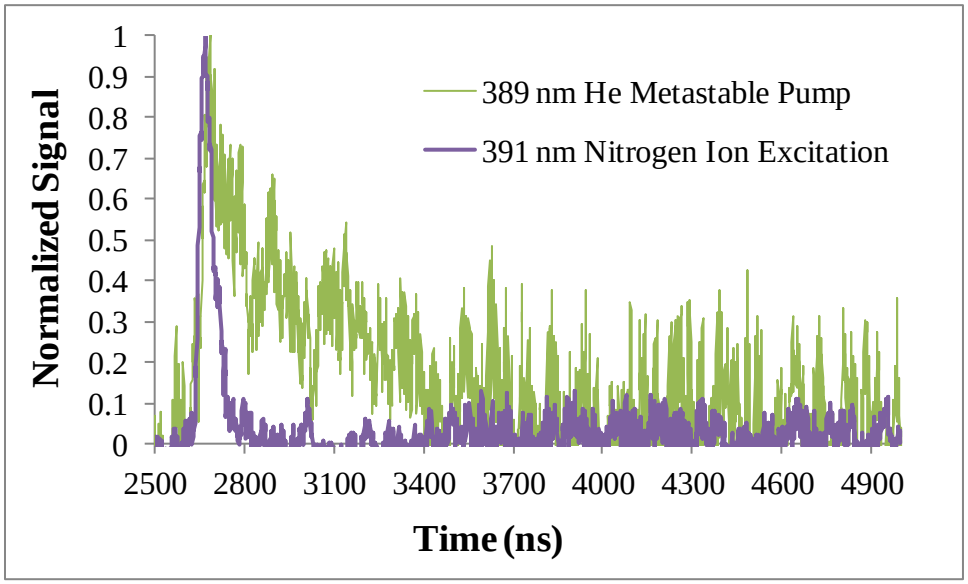

Figure 3.13: Temporal response of nitrogen ion at 427.81 nm to pumping of He_m state at 388.865 nm and excitation of N_2^+ at 391.44 nm.

The difference in the temporal decay of the signal in response to pumping of the He_m state seen in Figure 3.13 is further evidence that the nitrogen ion response seen at 388.865 nm in Figure 3.12 is not associated with the nitrogen ion band fluorescence.

Although the increase in signal does not disprove the Penning ionization process, it allows for speculation about other plasma processes. One such process is that of a charge transfer mechanism between He_2^+ species and N_2. Recall, production of He_2^+ is thought to occur by several mechanisms;[9, 15]

Three-body association reaction

$$He^+ + 2He \rightarrow He_2^+ + He \qquad 3.1$$

Metastable conversion

$$He_m + He_m \rightarrow He_2^+ + e- \qquad 3.2$$

Hornbeck-Molnar process

$$He^* (n \geq 3) + He \rightarrow He_2^+ + e- \qquad 3.3$$

According to the Hornbeck-Molnar Process, a charge transfer mechanism involving He_2^+ would be promoted by pumping He_m into excited states. This promotion of excited helium species is accomplished with the dye laser as discussed above. Of course, this is the only process of the three that could be used to explain the increase at 389 nm that is seen in Figure 3.12. The three-body reaction is not supported by the findings, and if the metastable conversion process were dominant, a decrease would be expected as metastable species are pumped away by the laser.

The increase in N_2^+ emission caused by laser pumping at 389 nm does not totally disprove the possibility of a Penning ionization reaction. The only energy requirement for Penning ionization to take place is that the energy of the excited atom be greater than that of the state of the product

ion. For this reason, it is possible for Penning ionization to be the result of interaction of He^* and N_2. This is not typically the case, as excited helium states are quickly depleted due to radiative relaxation. However, pumping the metastable state with the laser generates a significant increase in the excited state population. An excess in the He^* state may be the cause for a significant amount of Penning ionization to be occurring from this state. The additional energy in the He^* states may favor a promotion of N_2 to excited vibrational levels associated with the $B^2\Sigma_u^+$ ion state over a promotion to the ground state ion. This would also explain the increase in signal associated with pumping of the He_m state seen in Figure 3.12.

3.3.5 Nitrogen Recombination

The two maxima associated with the axial N_2^* profile in Figure 3.10 are, again, indicative of two different processes. Also, like the nitrogen ion emission, the only significant amount of N_2^* emission that persists after the passing of the energy wave is in the region from 0 to 10 mm downstream from the capillary tip. The persistence of the emission in this region suggests that N_2^* is the result of recombination of N_2^+ with an electron. The large and fast wave of N_2^* emission is more difficult to explain. It is possible that this too is the result of a recombination of N_2^+ that is formed 7 to 20 mm downstream from the capillary tip. Electron impact can also be responsible for N_2^* formation. However, in other studies, emission ratios of N_2^* were 10 times that of N_2^{+*} with electron impact.[16, 17] Accordingly, the emission ratios in this study do not support an electron impact mechanism for N_2^* formation. It would be interesting to test the temporal persistence of N_2 states with laser-induced fluorescence, as has been done with the nitrogen ion; however, experiments involving the imaging of neutral nitrogen in an ambient plasma would prove extremely difficult if not impossible.

3.4 Conclusions

Temporally-resolved measurements of He_m and N_2^+ populations in a helium DBD were made using laser-induced fluorescence. Time-resolved fluorescence images of He_m and N_2^+ reveal that the He_m and ground state N_2^+ populations persist beyond the time scale of the plasma bullet. The spatial and temporal correlation of the persistent He_m and ground N_2^+ populations is further evidence of Penning ionization of N_2 by He_m. This finding suggests that an increase in ionization efficiency would be obtained in DBD ionization sources with rf frequencies in the hundreds of kHz range compared to those that work in the single kHz range.

The emission seen from the plasma is the result of the periodic energy wave, termed plasma bullet, which seems to excite the many pre-existing species in the plasma via electron impact. These results show that N_2^{+*} emission is not mainly the result of Penning ionization of atmospheric nitrogen, and emission data alone may not provide adequate information about plasma processes.

3.5 References

1. Ricard, A.; Décomps, P.; Massines, F., Kinetics of Radiative Species in Helium Pulsed Discharge at Atmospheric Pressure. *Surf. Coat. Tech.* **1999,** *112* (1-3), 1-4.
2. Anderson, C.; Hur, M.; Zhang, P.; Mangolini, L.; Kortshagen, U., Two-Dimensional Space-Time-Resolved Emission Spectroscopy on Atmospheric Pressure Glows in Helium with Impurities. *J. Appl. Phys.* **2004,** *96* (4), 1835-1839.
3. Na, N.; Zhao, M.; Zhang, S.; Yang, C.; Zhang, X., Development of a Dielectric Barrier Discharge Ion Source for Ambient Mass Spectrometry. *J. Am. Soc. Mass Spectr.* **2007,** *18* (10), 1859-1862.
4. Zhu, Z.; Chan, G. C. Y.; Ray, S. J.; Zhang, X.; Hieftje, G. M., Microplasma Source Based on a Dielectric Barrier Discharge for the Determination of Mercury by Atomic Emission Spectrometry. *Anal. Chem.* **2008,** *80* (22), 8622-8627.
5. Hayen, H.; Michels, A.; Franzke, J., Dielectric Barrier Discharge Ionization for Liquid Chromatography/Mass Spectrometry. *Anal. Chem.* **2009,** *81* (24), 10239-10245.
6. Xiong, Q.; Lu, X.; Liu, J.; Xian, Y.; Xiong, Z.; Zou, F.; Zou, C.; Gong, W.; Hu, J.; Chen, K.; Pei, X.; Jiang, Z.; Pan, Y., Temporal and Spatial Resolved Optical Emission Behaviors of a Cold Atmospheric Pressure Plasma Jet. *J. Appl. Phys.* **2009,** *106* (8), 083302-6.

7. Urabe, K.; Morita, T.; Tachibana, K.; Ganguly, B. N., Investigation of Discharge Mechanisms in Helium Plasma Jet at Atmospheric Pressure by Laser Spectroscopic Measurements. *J. Phys. Appl. Phys.* **2010,** *43* (9), 095201.
8. Olenici-Craciunescu, S. B.; Muller, S.; Michels, A.; Horvatic, V.; Vadla, C.; Franzke, J., Spatially Resolved Spectroscopic Measurements of a Dielectric Barrier Discharge Plasma Jet Applicable for Soft Ionization. *Spectrochim. Acta B* **2011,** *66* (3-4), 268-273.
9. Chan, G. C. Y.; Shelley, J. T.; Wiley, J. S.; Engelhard, C.; Jackson, A. U.; Cooks, R. G.; Hieftje, G. M., Elucidation of Reaction Mechanisms Responsible for Afterglow and Reagent-Ion Formation in the Low-Temperature Plasma Probe Ambient Ionization Source. *Anal. Chem.* **2011,** *83* (10), 3675-3686.
10. Heywood, M. S.; Taylor, N.; Farnsworth, P. B., Measurement of Helium Metastable Atom Densities in a Plasma-Based Ambient Ionization Source. *Anal. Chem.* **2011,** *83* (17), 6493-6499.
11. Teschke, M.; Kedzierski, J.; Finantu-Dinu, E. G.; Korzec, D.; Engemann, J., High-Speed Photographs of a Dielectric Barrier Atmospheric Pressure Plasma Jet. *IEEE Transactions on Plasma Science* **2005,** *33* (2), 310-311.
12. Shi, J.; Zhong, F.; Zhang, J.; Liu, D. W.; Kong, M. G., A Hypersonic Plasma Bullet Train Traveling in an Atmospheric Dielectric-Barrier Discharge Jet. *Phys. Plamsas* **2008,** *15* (1), 013504-5.
13. Massines, F.; Rabehi, A.; Decomps, P.; Gadri, R. B.; Segur, P.; Mayoux, C., Experimental and Theoretical Study of a Glow Discharge at Atmospheric Pressure Controlled by Dielectric Barrier. *J. Appl. Phys.* **1998,** *83* (6), 2950-2957.
14. Hotop, H.; Niehaus, A., Reactions of Excited Atoms and Molecules with Atoms and Molecules: V. Comparing of Penning Electron and Photoelectron Spectra of H_2, N_2 and CO. *Int. J. Mass Spectrom.* **1970,** *5* (5-6), 415-441.
15. Martens, T.; Mihailova, D.; van Dijk, J.; Bogaerts, A., Theoretical Characterization of an Atmospheric Pressure Glow Discharge Used for Analytical Spectrometry. *Anal. Chem.* **2009,** *81* (21), 9096-9108.
16. Paris, P.; Aints, M.; Laan, M.; Valk, F., Measurement of Intensity Ratio of Nitrogen Bands as a Function of Field Strength. *J. Phys. Appl. Phys.* **2004,** *37* (8), 1179.
17. Paris, P.; Aints, M.; Valk, F.; Plank, T.; Haljaste, A.; Kozlov, K. V.; Wagner, H. E., Intensity Ratio of Spectral Bands of Nitrogen as a Measure of Electric Field Strength in Plasmas. *J. Phys. Appl. Phys.* **2005,** *38* (21), 3894.

4 Helium-Hydrogen Mixed Gas Discharge Ionization Source

4.1 Introduction

Typically, APCI processes, like those proposed for electrical-discharge-based ADI sources, involve ionic adduction of an ionized species from a reacting gas to form desired analyte-ion complexes. These processes are prevalent in plasma sources like DAPCI, which use solvent vapors to form a variety of reagent ions in the gas stream.[1-3] In ADI-MS, sources that take advantage of adduction reactions are sometimes called "reactive" sources. Reactive sources take advantage of the ability to add reagent ions that are critical to analyte ionization to the discharge gas.

Likewise, it has been hypothesized that the addition of critical reaction species to discharge gases may contribute to an enhancement of existing proton addition ionization mechanisms and subsequently an increase in analyte ionization. For proton addition, experiments where nitrogen, water, and hydrogen are added to the discharge carrier gas are of particular interest. Olenici-Craciunescu et al. added N_2 to their DBD source to determine the effect that the concentration of nitrogen had on the ionization process in IMS.[4] They found that addition of N_2 to the discharge gas caused a change in plasma conditions resulting in a loss in He_m, and they obtained optimal IMS signal with pure He.

Hydrogen, like nitrogen, plays a significant role in the proposed APCI mechanism, specifically for proton addition. In this work, a mixture of 1% H_2 in helium is used to test the effect of hydrogen on the metastable population, as well as hydrogen's effect on the ion signal in ADI-MS experiments. Spectroscopic and mass spectrometric methods are used to compare the conditions and performance of DBD APPJ ionization sources using pure helium and helium/hydrogen (He/H_2) discharge gases.

4.2 Experimental Conditions

4.2.1 ADI-MS

4.2.1.1 Setup

Experiments involving He/H_2 mixed gases were carried out over a period of several months, during which time changes were made to the ADI-MS and imaging setups. Improvements to the ADI-MS setup have been described in the preceding chapter. The initial ADI-MS setup is described in Chapter 2, and a picture of improvements made to the setup can be seen in Figure 3.1. Briefly, slides spotted with or dipped in a solution containing a target analyte were placed in front of the Finnigan LCQ Classic mass spectrometer (Thermo Scientific, West Palm Beach, FL, USA.) by means of custom-built slide mounts shown in Figures 2.3 and 3.1. The custom mounts allowed for the easy insertion and removal of the slides. The plasma was placed at a distance and angle to the glass slide by means of an x,y,z,θ stage. The plasma was allowed to come in contact with the slide and analyte. Analyte signal was monitored by Xcaliber version 2.0 software (Thermo Scientific, West Palm Beach, FL, USA.). The gas feed for the ionization source was connected to a two-way valve, allowing me to freely switch between He and He/H_2 discharge gases. Flow rates were controlled by a Brooks 5850C mass flow controller and Brooks 5876 power supply/readout (Brooks Instruments, Hatfield, PA, USA.) or a MKS 1170A mass flow controller and MKS 246C power supply/readout (MKS Instruments, Andover, MA, USA.). Ultrahigh purity helium (99.999%) (Airgas, Radnor, PA, USA.) was used for the He discharge and a tank of He with 0.998% H_2 (Air Liquide America Specialty Gases,

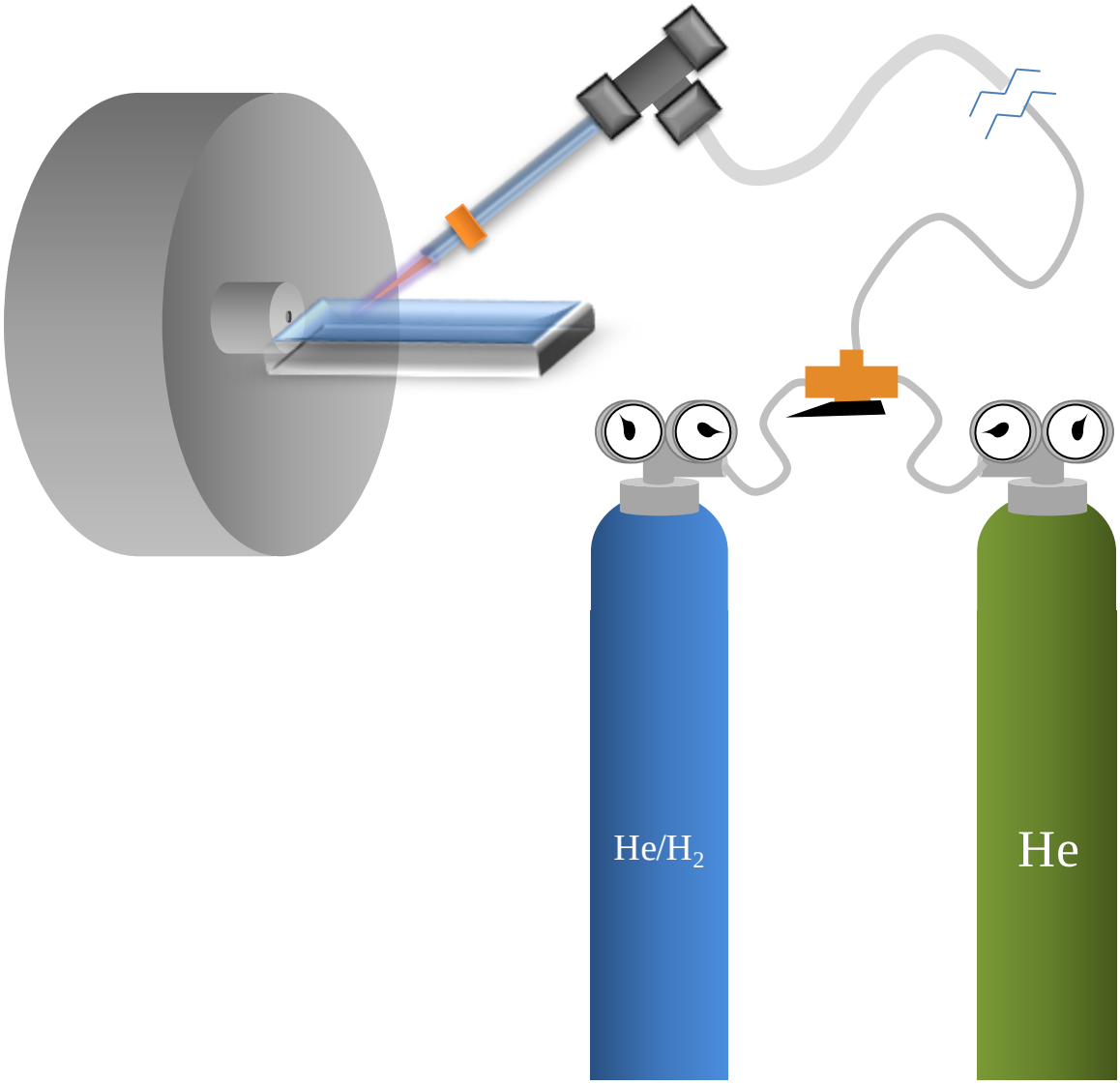

Figure 4.1: ADI-MS setup for He vs. He/H_2 discharge gas experiments.

Longmont, CO, USA.) was used for the He/H_2 discharge. Flow rates of up to 2.0 L/min were used. A drawing of the setup is shown in Figure 4.1. Mass spectra were obtained for target analytes, monitoring analyte signal for 1-2 min. Experiments also involved monitoring of analyte signal while simultaneously switching between gas types.

4.2.1.2 Determination of Optimal He/H_2 Ratios

For the determination of optimal He/H_2 ratios, the He and He/1% H_2 tanks were each fitted with a mass flow controller. The output from the mass flow controllers was mixed by a Swagelok T, and the gas mixture was used as the discharge gas. Flow rates used to generate various ratios of the gas mixture are shown in Table 4.1. Slides were dipped in a 100 ppm solution of caffeine in methanol. Optimum ratios were determined to be those that produced the best ADI-MS signal for caffeine.

Table 4.1: *Mass Flow Controller (MFC) Flow Rates and % H_2.*

MFC Reading for He/1% H_2 (%)	Volume of He/1% H_2 (L/min)	MFC Reading for He Gas (%)	Volume of He (L/min)	Total Volume (L/min)	% H_2
0	0	100	2	2	0
50	1	50	1	2	0.5
60	1.2	40	0.8	2	0.6
70	1.4	30	0.6	2	0.7
80	1.6	20	0.4	2	0.8
90	1.8	10	0.2	2	0.9
100	2	0	0	2	1

4.2.2 Imaging

4.2.2.1 Helium Species

Imaging of He_m fluorescence and He^* emission was accomplished using the setup described in Section 2.2.3 and 2.2.4. Briefly, for reference, the excimer laser (Lambda Physik

LPX 210i) operating at 25 Hz was used to pump a dye laser (Lambda Physik Scanmate 2) containing BBQ dye (Exciton, Dayton, OH, USA.) in dioxane. The dye laser was tuned to 388.865 nm for excitation of the He_m–He* transition as illustrated in Figure 2.1. The dye-laser radiation was focused into a 400 μm diameter fiber-optic/delay line. The laser radiation from the fiber was collimated with a 25.4 mm diameter spherical lens (f = 50.8 mm) and then focused with a 25.4 mm diameter cylindrical lens (f = 76.2 mm), which generated a plane of radiation that contained the plasma jet region of the discharge, which was mounted vertically using the 0^o angle aluminum mount. The plane of radiation was perpendicular to the axis of the imaging optics. For side-on imaging of the plasma jet, emission and fluorescence were collected with a pair of matched achromatic doublets having focal lengths of 100 mm and proving unit magnification. A Semrock FF01-588/21-25 band-pass filter (Semrock, Rochester, NY, USA.) was placed between the two achromatic doublets for spectral filtering of the emission and fluorescence. The emission and fluorescence were focused onto a PI-MAX intensified charge coupled device (iCCD) (Princeton Instruments, Trenton, NJ, USA.). The iCCD was run at a temperature of -20^o C. Emission images were collected in shutter mode with images consisting of 250 exposures at 500 μs/exposure. Fluorescence images were taken in gate mode with the gate set to 20 ns and triggered by the laser with a photodiode. Each fluorescence image was an accumulation of 50 images with 100 exposures/image. All imaging data were collected and processed using Winview 32 software (Princeton Instruments, Trenton, NJ, USA.). A diagram of the experimental setup for obtaining He_m fluorescence and He^* emission images is shown in Figure 2.5. Background images of plasma emission and laser scatter, collected with the laser detuned to 390 nm, were subtracted from the raw fluorescence images to produce the images. Cross sections of these images are presented in this work.

4.2.2.2 Spectral Imaging

4.2.2.2.1 Time-Averaged Spectral Images

Time-averaged spectral images were obtained with the setup described in Section 2.2.5. Briefly, the plasma emission was collected using a combination of achromatic doublets to produce a 1:3 image of the plasma. The emission was focused on the entrance slit of a Shamrock SR-303i spectrograph (Andor Technology, Belfast, Northern Ireland). A slit width of 25 μm was used to capture the emission from the central 75 μm of the plasma. Emission was dispersed by the grating onto an iDus CCD (Andor Technology, Belfast, Northern Ireland). The CCD was run at a temperature of -80^{o} C to minimize dark current contributions. Spectral images were taken with an exposure time of 1 s. The images were viewed and recorded using Solis (s) Software (Andor Technology, Belfast, Northern Ireland).

4.2.2.2.2 Time-Resolved Spectral Images

Time-resolved spectral images were obtained as described in Sections 3.2.5 and 3.2.6. Briefly, discharge emission was collected by a pair of achromatic doublets having focal lengths of 300 mm and 100 mm, providing a 1:3 magnified image of the discharge. The first achromatic doublet was placed at 90^{o} with respect to the other and separated by a MM1-311S-25.0 mirror (Semrock, Rochester, NY, USA.). The imaging optics were used to image the discharge onto the slits of a McPherson 2061, Czerny Turner monochromator (McPherson, Chelmsford, MA, USA.). Emission wavelengths were selected using the monochromator and were focused onto an iCCD (Princeton Instruments, Trenton, NJ, USA.) at the monochromator exit port, generating an axially resolved spectral image of the plasma emission. The time-resolved emission imaging consisted of 31 images, taken across the waveform from trough to trough, every 100 ns. Each image consisted of a 100 ns gate, with 30,000 gates per exposure, and 1-5 software

accumulations. Time-resolved emission measurements were taken of He^* (706.52 nm), N_2^{+*} (391.44 nm), N_2^* (357. 69 nm), and O^* (777.19 nm), and H^* (α line at 656.28 nm). The iCCD was triggered at 3 kHz by the timing electronics. The images were viewed, processed and converted to ascii files by Winview 32 software (Princeton Instruments, Trenton, NJ, USA.). Axial profiles were taken of each spectral image by summing the pixels across the spectral line or band head of the emitting species. Time-resolved data were processed as .ascii files using Matlab software (The MathWorks, Natick, MA, USA.).

4.3 Results and Discussion

4.3.1 Imaging Studies

4.3.1.1 Imaging Helium Species

Images were taken of the He_m fluorescence and He^* emission from a He and He/H_2 discharge. Axial profiles, taken from the images, are compared in Figure 4.2. The results show that hydrogen causes a significant loss in He^* emission and a nearly complete quenching of the He_m population. This experiment provides further evidence that He^* emission is a poor indicator of He_m densities. The quenching of excited helium states is expected with the addition of hydrogen. This is similar to the results seen by Olenici-Craciunescu et al. when adding N_2 to the plasma gas.[4]

4.3.1.2 Spectral Imaging

Spectral imaging was also used to compare the two different plasma jets. Excited nitrogen ion, helium and oxygen emission are seen in the spectral image of a He plasma jet in Figure 4.3 (a). Comparison of spectral images of the He plasma jet with that of the He/H_2 plasma seen in Figure 4.3 (b) indicates a quenching of excited helium states. Spectral images

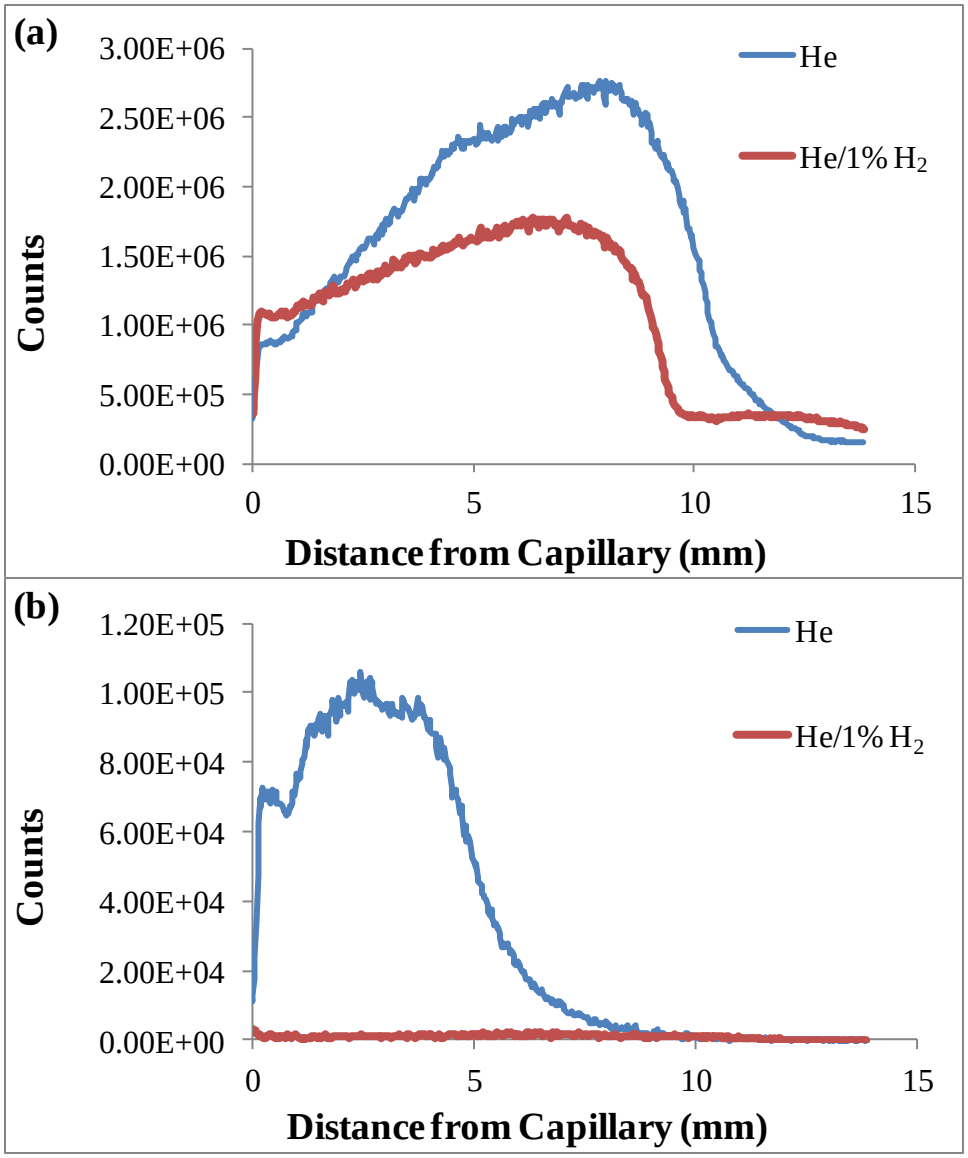

Figure 4.2: Axial cross sections of (a) He^* emission and (b) He_m fluorescence from the plasma jet run with He and He/H_2 as the discharge gas.

also reveal quenching of nitrogen ion emission and a significant quenching of excited oxygen emission at 777 nm. The quenching, seen in Figure 4.3 (b) seems to be isolated to the bottom or initial portion of the plasma jet from 0 to 9 mm downstream from the capillary tip. Also, in this region of the plasma jet, there is a significant increase in helium alpha (H_α) emission at 656.28 nm. Further downstream, the hydrogen emission dies and there is an increase in excited state nitrogen and helium emission. Both spectral images indicate a bimodal nature of the plasma. The region from 0 to 10 mm downstream from the tip of the capillary shows a broad series of emission bands throughout the spectrum. These spectral images are an indication of the diffuse nature of this region of the plasma. Conversely, the region of the plasma beyond 10 mm downstream consists of mainly the typically observed atomic lines and molecular bands. This bimodal nature is consistent with the data presented in Chapter 3.

Time-resolved data confirm what is seen in Figure 4.3. They also show that the reappearance of the downstream excited nitrogen ion and helium emission is due to a fast and intense emission, similar to that seen downstream in the He plasma jet in Chapter 3. It is, therefore, proposed that this reappearance of the He^* and N_2^{+*} emission, after having been quenched, is the result of electron impact ionization by the ionization wave.

4.3.2 ADI-MS

4.3.2.1 Comparative Ionization Experiments

If helium metastable atoms are playing a direct role in analyte ionization, one would expect the quenching of the He_m population illustrated in Figure 4.2 (b) to result in a decrease in analyte ion production. In practice, the opposite effect is observed. The signal of the $[M+H]^+$ peak of coumarin 47 was recorded as a function of time while switching the gas supply between the pure helium and the 1% hydrogen mixture. The time-dependent signal is shown in Figure

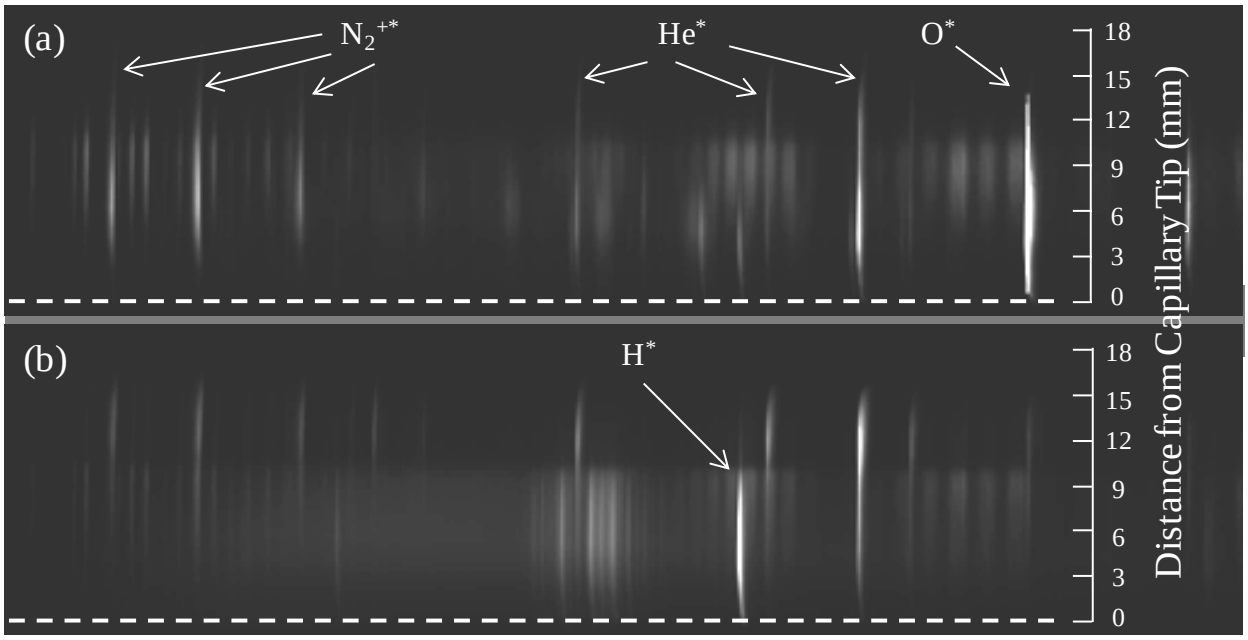

Figure 4.3: Spectral image across the UV-Vis of (a) the He discharge and (b) the He/H_2 discharge. The dotted line represents the position of the tip of the capillary.

4.4. The times when the plasma was turned on and when the gas was switched are indicated by vertical lines in the plot. The delay from the time the gas was switched to an observed change in signal was about 1 s. Note that there was no significant signal at the M^+ peak, and there was minimal fragmentation. The removal of the dye can be seen over a period of two minutes in the general decrease in both signals. On top of the general desorption curve, an increase in signal by nearly a factor of two accompanies the switch to the He/H_2 mixture. Similar results have been obtained and presented for caffeine.[5]

Despite the substantial loss of excited plasma species and the significant quenching of the He_m population, ADI-MS signal was enhanced. These results suggest that an ionization process other than the previously proposed Penning ionization-initiated APCI mechanism is at work.

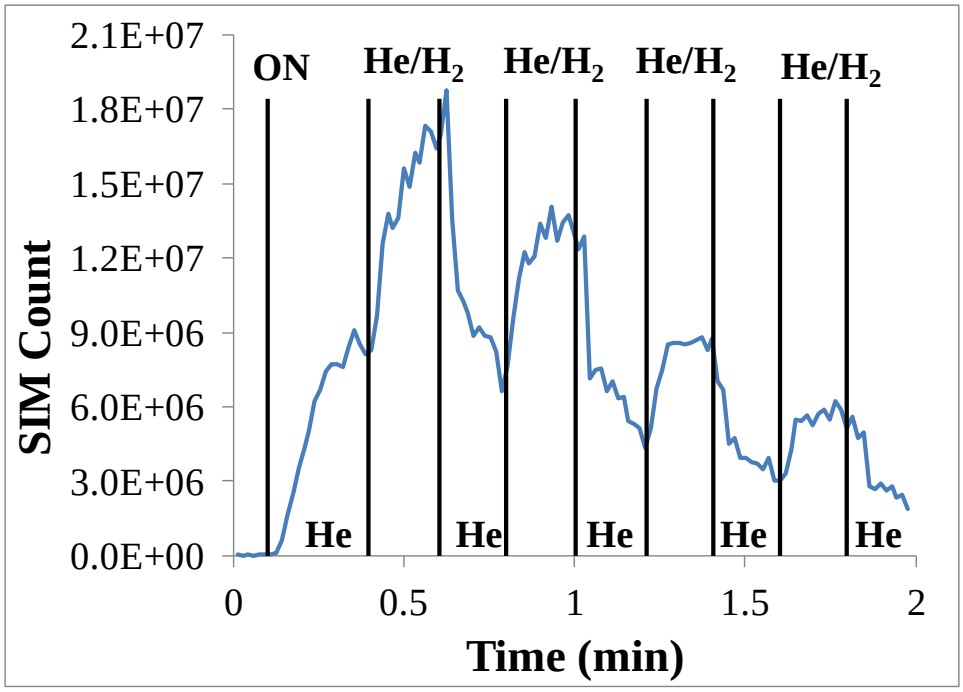

Figure 4.4: Time-dependent ADI-MS signal of coumarin 47 dye $[M+H]^+$ peak.

4.3.2.2 Optimal He/H_2 Ratios

It is clear that the addition of hydrogen to the plasma gas causes a quenching of excited plasma species. This quenching effect is also observed in ADI-MS experiments. When experimenting with lower-power DBDs for ADI-MS, it is difficult to light the plasma when using He/1% H_2 gas. This is problematic when switching from He to He/H_2 gas in comparative experiments. To make comparisons between a He and He/H_2 plasma, it is necessary to run a He/H_2 DBD source and a comparable He-only source at the same relatively high powers, typically 35 W. This prevents the plasma from cutting out altogether when switching from He to He/H_2 gas. Lower-power plasmas can also cause a loss in signal when switching to a He/H_2 plasma, and the desired increase demonstrated in Figure 4.4 is not observed. Because the plasma is quenched by the addition of hydrogen, it is necessary to determine the optimum amount of hydrogen that would allow for an increase in ionization without extensive quenching

and subsequent loss of ADI-MS signal. The optimal He/H_2 ratio for DBDs at 35 W is shown in Figure 4.5. The rise in signal when comparing He with the He/1% H_2 is less visible due to the more substantial increase when using a He/0.9% H_2 mix. The increase in signal when using a He/0.9% H_2 mixture provides encouragement for more comparative ADI-MS tests with the He discharge at this ratio. Future experiments will also include the testing of various He/H_2 ratios for lower power plasmas. Results from these studies will be correlated with spectroscopic measurements.

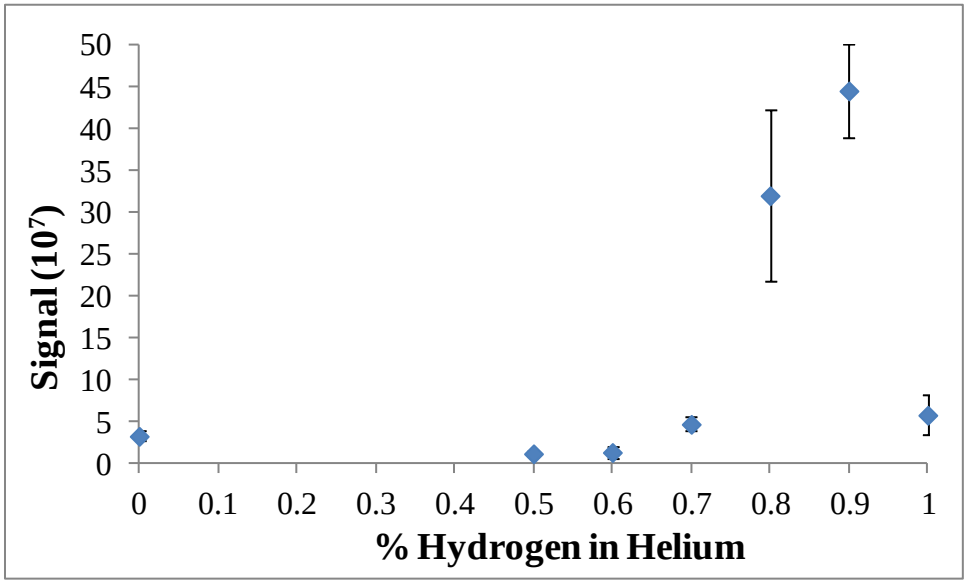

Figure 4.5: ADI-MS signal of caffeine $[M+H]^+$ peak for various ratios of H_2 added to the discharge gas.

4.3.3 Potential Mechanisms

With the He_m state being quenched so significantly by the addition of the hydrogen to the discharge gas, it is not likely that increase in signal is the result of an enhancement of the

previously proposed mechanisms initiated by Penning ionization of atmospheric nitrogen. The above results suggest that other mechanisms involving proton addition should be explored.

When considering the protonation of analytes, the most acidic species to be considered is the proton (H^+) itself. Studies have been carried out that explore the reactions of hydrogen and helium in plasmas at varying pressures and ratios of He and H_2.[6-9] Products of these reactions include H^+. These products are thought to mainly be the result of Penning ionization and charge transfer processes

$$He_m + H_2 \rightarrow \text{Products} \qquad 4.1$$

$$He_2^+ + H_2 \rightarrow \text{Products} \qquad 4.2$$

where products include H_2^+, HeH^+, He_2H^+, HeH_2^+, and H^+ ions. Although the production of H^+ is considered in these reactions, it was found to be a minor product.[9] Other sources of H^+ can be found in the HeH^+ species, which may also facilitate proton addition. This cationic complex is also considered to be a major product of the above reactions. It is also proposed that HeH^+ may be the product of ionic molecular hydrogen reacting with helium.

$$H_2^+ + He \rightarrow HeH^+ + H \qquad 4.3$$

The above reactions also produce free hydrogen (H). It is also possible that this product may subsequently be ionized via electron impact reaction to produce H^+.

Although reactions involving He_m are favored in the literature, it is unclear at this time which processes dominate in this plasma. It is possible for multiple reactions to play a significant role in proton production, but plasma processes involving He and H_2 will need to be studied before any significant conclusions can be made.

4.4 Conclusions

Spectroscopic and mass spectrometric studies have been carried out on a He/H_2 mixed gas plasma. Although it was shown that the addition of hydrogen to the discharge gas quenches excited plasma species, including critical He_m species, an enhancement in ADI-MS signal was observed. This improvement in ionization is thought to be due to an alternate ionization mechanism involving the production of H^+. Enhanced signal production by using a He/H_2 gas mixture points to possible benefits of using He/H_2 to improve ionization via proton addition for plasma-based ADI sources.

4.5 References

1. Song, Y.; Cooks, R. G., Atmospheric Pressure Ion/Molecule Reactions for the Selective Detection of Nitroaromatic Explosives Using Acetonitrile and Air as Reagents. *Rapid Commun. Mass Sp.* **2006,** *20* (20), 3130-3138.
2. Chen, H.; Liang, H.; Ding, J.; Lai, J.; Huan, Y.; Qiao, X., Rapid Differentiation of Tea Products by Surface Desorption Atmospheric Pressure Chemical Ionization Mass Spectrometry. *J. Agr. Food Chem.* **2007,** *55* (25), 10093-10100.
3. Cotte-Rodriguez, I.; Hernandez-Soto, H.; Chen, H.; Cooks, R. G., In Situ Trace Detection of Peroxide Explosives by Desorption Electrospray Ionization and Desorption Atmospheric Pressure Chemical Ionization. *Anal. Chem.* **2008,** *80* (5), 1512-1519.
4. Olenici-Craciunescu, S. B.; Michels, A.; Meyer, C.; Heming, R.; Tombrink, S.; Vautz, W.; Franzke, J., Characterization of a Capillary Dielectric Barrier Plasma Jet for Use as a Soft Ionization Source by Optical Emission and Ion Mobility Spectrometry. *Spectroc. Acta Pt. B-Atom. Spectr.* **2009,** *64* (11-12), 1253-1258.
5. Wright, J. P.; Heywood, M. S.; Farnsworth, P. B. *Optical and Mass Spectrometric Studies of a Helium Dielectric-Barrier Discharge Used as an Ambient Ionization Source*, American Society for Mass Spectrometry, Denver, Colorado, 2011.
6. Hotop, H.; Niehaus, A., Reactions of Excited Atoms and Molecules with Atoms and Molecules: V. Comparing of Penning Electron and Photoelectron Spectra of H_2, N_2 and CO. *International J. Mass Spectrom. and Ion Physics* **1970,** *5* (5-6), 415-441.
7. Veatch, G. E.; Oskam, H. J., Collision Processes Occurring in Decaying Plasmas Produced in Helium-Hydrogen Mixtures. *Phys. Rev. A* **1973,** *8* (1), 389-396.
8. Motret, O.; Pouvesle, J. M.; Stevefelt, J., Spectroscopic Study of the Afterglow Excited by Intense Electrical Discharges in High-Pressure Helium Hydrogen Mixtures. *J. Chem. Phys.* **1985,** *83* (3), 1095-1100.
9. Adams, N. G.; Bohme, D. K.; Ferguson, E. E., Reactions of He_2^+, Ne_2^+, Ar_2^+, and Rare-Gas Hydride Ions with Hydrogen at 200°K. *J. Chem. Phys.* **1970,** *52* (10), 5101-5105.

5 Future Studies of Helium-Based Discharges as ADI Sources

5.1 Introduction

As the field of ADI-MS develops, much of the research surrounding this field will be focused on applications of the ADI-MS technique and improvement of ADI sources. Improvements to ADI sources will require a fundamental understanding of desorption processes, and ionization mechanisms, including pathways that lead to negative ion formation, and how matrix effects influence these processes. Therefore, the focus for future work with an APPJ will be three fold; development, improvement, and fundamental characterization of the ionization source. Experiments will include studies that compare the APPJ to other plasma-based ADI sources.

5.2 Work in Progress

5.2.1 Time-Resolved Plasma Studies

Although my current work emphasizes the importance of Penning ionization, it does not provide a comprehensive understanding of this plasma process as it relates to ambient ionization. In the time-resolved studies, it was demonstrated that nitrogen ion emission is the result of a propagating ionization wave. The resulting emission showed a bimodal nature, indicating two distinct plasma regions. The nature of these regions and how they affect the plasma bullet and plasma processes are unclear at this time. Additional time-resolved studies of the ionization wave of energy, and the relation it has to plasma emission will be conducted.

The time-resolved studies also reveal a strong correlation between the temporal and spatial fluctuations of He_m and N_2^+ species. However, these images do not prove that nitrogen ions are formed by Penning ionization, as the lifetime of the ground state nitrogen ion is

unknown. More definitive evidence of Penning ionization can be obtained by comparing the decay of He_m and N_2^+ species after being excited in the plasma. This will require the construction of a new APPJ that functions at single kHz frequencies. A lower frequency will provide hundreds of microseconds between plasma bullets, allowing for the determination of the decay rates of the He_m and N_2^+ species. A comparable decay rate between the two species would be convincing evidence of Penning ionization.

5.2.2 He/H_2 Studies

One of the drawbacks of using a He/H_2 mixed gas for improving analyte detection using a plasma-based discharge is that it requires a high power plasma. Therefore, it is likely that other, low power, helium plasma-based ADI sources, like the LTP, will experience a decrease in ADI-MS signal instead of the increase that I observe when using a 0.9% mixture of hydrogen. It is suggested that low power plasma-based ADI sources might take advantage of this enhancement in ionization by adding smaller percentages of hydrogen to the helium gas mixture. A lower hydrogen concentration would counter the effects of quenching that generate a loss instead of an increase in ionization.

This idea can be tested by determining the optimum ratios of He/H_2 for the DBD APPJ source at lower powers. Initial results for a 25 W plasma are shown in Figure 5.1. A shift in optimum ADI-MS signal for 100 ppm caffeine is observed for a He/H_2 ratio of 0.5% H_2. Similar tests will be performed for lower power settings for the DBD APPJ to determine what point the addition of hydrogen becomes disadvantageous.

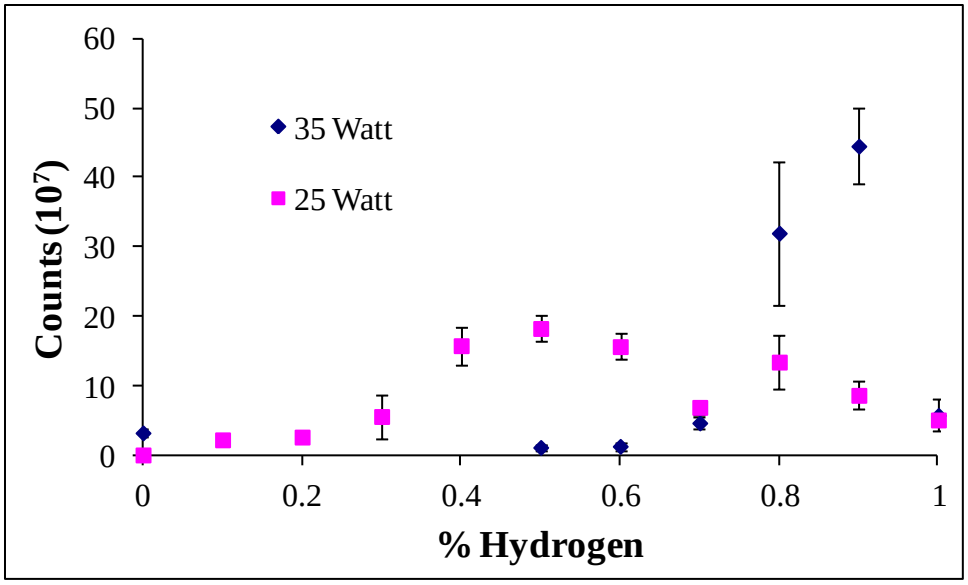

Figure 5.1: ADI-MS signal of caffeine $[M+H]^+$ peak for various ratios of H_2 added to the discharge gas taken at plasma powers of 25 and 35 W.

The main question that arises in research involving He/H_2 mixed gas plasmas is how a plasma source, which quenches many of the excited helium and nitrogen ion species, improves ionization and detection. For further understanding, time-averaged spectral images will be taken of the He/H_2 plasma jet and be compared to those of a He plasma jet at various powers and He/H_2 ratios. Particular attention will be paid to the quenching of excited helium, nitrogen ion, and oxygen emission, and the increase in excited hydrogen emission lines as concentrations of hydrogen are increased in the gas mixture. It is expected that these emission images may give an idea about where certain species exist in the plasma. For example, the quenching of He^* species and the appearance of H^* species could be the result of the formation of HeH^+ and H^*. These products are the result of several reactions that have been previously discussed. It is hoped that evidence supporting any such reactions is obtained.

It is also important that this novel plasma be tested on a variety of analytes, to determine if the enhancement observed in Chapter 4 can be expected for various analytes having a range of

proton affinities. Although the He/H_2 plasma provides a desired enhancement for proton addition mechanisms, it is not known if any enhancements will be seen for ionization mechanisms that rely on electron capture, dissociative electron capture or anion adduction, the results of which can be seen in the negative ion mode.[1] In my limited experience with the negative ion mode, I have observed significant oxidation for cyclic aromatic hydrocarbons. This observation has been made elsewhere in the literature.[2] As the He/H_2 plasma is effective at quenching excited oxygen, it may reduce the observed oxidation of select compounds and result in detection of molecular ions.

5.2.3 Surface Effects

Previously, it has been shown that the presence of a glass slide can cause an increase in He_m populations in a DBD APPJ.[3] The increase was thought to be the result of grounding effects caused by the glass slide. This change in the plasma constitutes a matrix effect caused by the presence of a surface. In typical ADI-MS, there is always a sample surface present. Under laboratory conditions, most studies use a single surface or single type of surface, like a Teflon belt to sample blood spots or glass slides where analyte has been deposited. For in-field detection, a single analyte (i.e., illegal drug, or explosive precursors) may need to be sampled from a variety of surfaces. Currently, it is not understood how various sample surfaces affect desorption and ionization.

In order to test the effect various surfaces have on analyte desorption and ionization, several microscope slide-sized sample surfaces have been made from different materials. At present, Delrin, Teflon, and copper surfaces have been made to be compared to the typical glass sampling surface. Sample surfaces such as paper and cloth still need to be made. The sample

surfaces were made to be the same size as a microscope slide so they can fit into the slide holder and mount, allowing for an easy switch between surface types during ADI-MS experiments.

ADI-MS experiments with various sample surfaces can be correlated with spectroscopic measurements of He_m in the plasma jet in the presence of the same surfaces. It is expected that surfaces like copper will enhance He_m populations due to grounding effects, and grounding of the plasma to the copper surface will also cause the copper surface to heat up significantly. Despite these observations that would suggest an enhancement in desorption and ionization, initial results show that ADI-MS with a copper sample surface gives no analyte signal. This is because the plasma jet grounds directly to the copper slide, preventing plasma-sample interaction. Similar observations still need to be made for the other surfaces mentioned.

Surface-related ADI-MS experiments should be conducted with a variety of analytes having a range of vapor pressures to test how thermal conductivity relates to desorption. Also, the effects of surfaces on ADI-MS using a He/H_2 plasma jet should be tested.

5.2.4 Direct Current Discharge

Previously, the time-dependent nature of the plasma jet has allowed me to observe plasma processes as they relate to the temporal wave of emission or plasma bullet. The wave of emission is thought to be the result of electron impact ionization that seems to excite the preexisting species in the plasma.[4-6] In some respects, the complex, time-dependent behavior associated with plasma bullets masks the fundamental processes that need to be studied. The time-varying nature of the plasma is, of course, the result of the radio frequency voltage waveform used to generate the plasma. It is possible to study plasma processes without the interference of temporal fluctuations by generating a similar plasma using a DC power supply. Most DC ADI sources only produce small afterglows or hot gas like the FAPA or the DART.

For detailed spectroscopic studies, it would be convenient to have a plasma that extends more than a centimeter into the air. The DCBI is a good example of a DC plasma that extends several centimeters into the air that could be studied using LIF and emission spectroscopy.[7] The Farnsworth lab has been working to create a DC discharge on which spectroscopic and ADI-MS measurements can be performed.

The DC discharge is housed in a 1/4 in. Swagelok T. A high voltage needle is inserted into the housing through a Teflon ferrule. A Teflon ferrule is needed to insulate the body of the T from the applied high voltage. Plastic sleeves, highlighted in the bottom picture of Figure 5.2, are also used in the chamber to prevent unwanted arcing to the chamber walls. A perforated ceramic sleeve is used to keep the needle centered throughout the chamber without disturbing the flow of helium. The helium is introduced by a 1/4 in to 1/8 in NPT-to-Swagelok reducer, allowing for the new source to be mounted with the same 1/8 in Swagelok grip mount used for the DBD source. The gas flows through a 1/4 in. pipe fitting and cap with a 1 mm diameter orifice. The discharge is formed between the needle and the cap.

The high voltage is applied with a BHK 1000-0.2 MG high voltage power supply (Kepco Flushing, NY, USA.). A 2.2 kΩ resistor is placed in series with the cathode to compensate for negative resistance. The resistor is rated for 10 W, limiting the discharge current to less than 67 mA. In constant current mode at 60 mA, we can generate a plasma at around 300 V (~13 W) which protrudes more than a centimeter from the orifice.

Unfortunately, the plasma is not stable over a usable time period and tends to leave a black buildup on the needle. This development is suggests that the tungsten needle is oxidizing or that residue from the plastic sleeves is depositing on the needle surface. This plasma is likely very dirty and will be the source of complicated and messy background mass spectra. Improvements

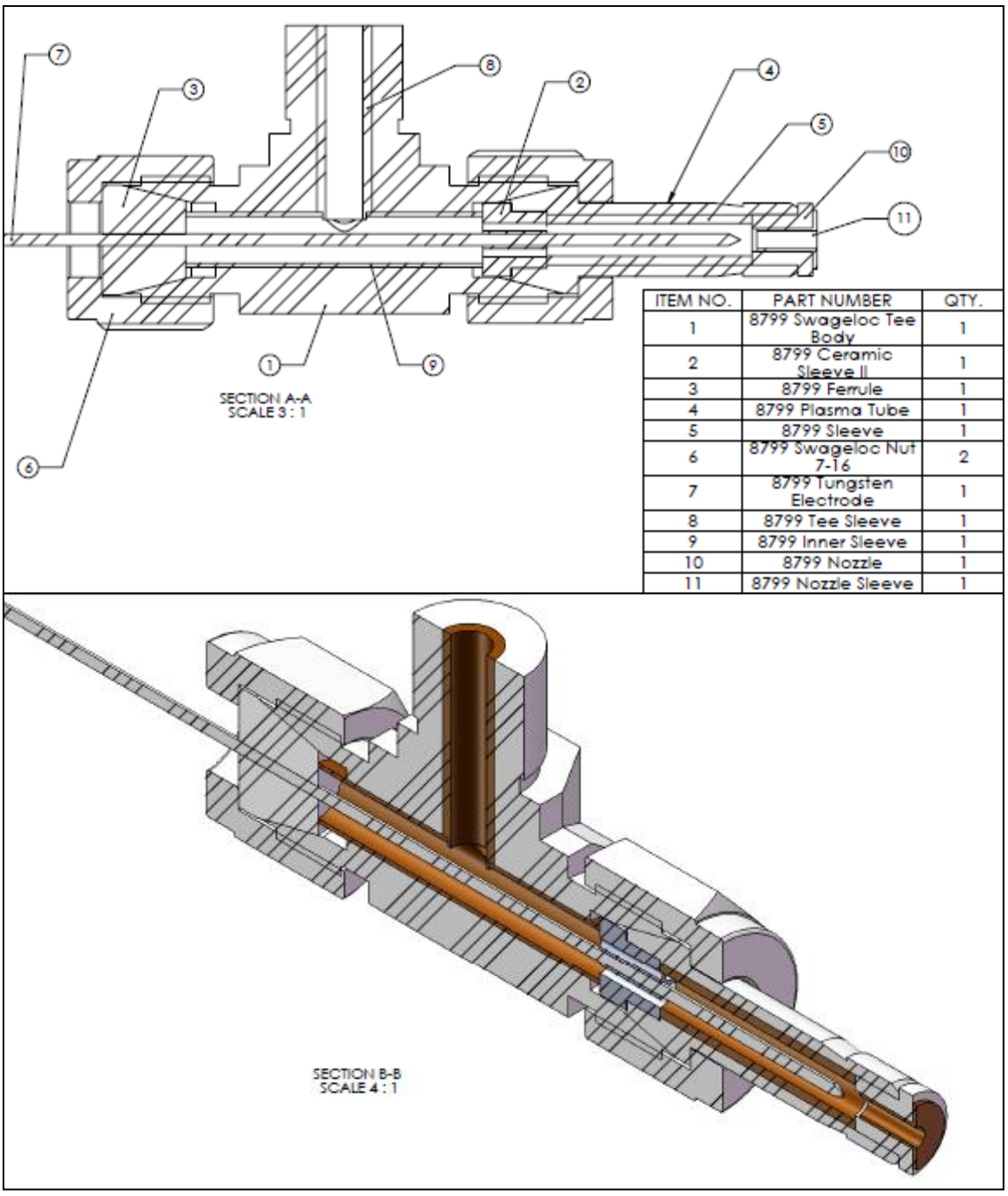

ITEM NO.	PART NUMBER	QTY.
1	8799 Swageloc Tee Body	1
2	8799 Ceramic Sleeve II	1
3	8799 Ferrule	1
4	8799 Plasma Tube	1
5	8799 Sleeve	1
6	8799 Swageloc Nut 7-16	2
7	8799 Tungsten Electrode	1
8	8799 Tee Sleeve	1
9	8799 Inner Sleeve	1
10	8799 Nozzle	1
11	8799 Nozzle Sleeve	1

Figure 5.2: Schematic cross sections of the DC discharge source.

need to be made until the discharge proves useful as an ADI source. Then comparative spectroscopic measurements can be made.

5.2.5 Discharge Characterization by Tunable Diode Laser Absorption Spectroscopy

Future research involving helium-based discharge ADI sources should include comparative studies as a major area of focus. In comparative studies, ADI sources should be characterized not only by their performance as ADI sources, but also their physical properties. Such characterization would require physical measurements that relate to fundamental processes that govern desorption and ionization. Generally, it is accepted that ambient desorption by electrical discharge-based sources is the result of thermal processes. It is also generally accepted that He_m play a critical role in ionization for these sources. Therefore, when characterizing a helium-based discharge ionization source, it would be important to know gas temperatures and absolute He_m number densities. These measurements would provide potential information about desorption and ionization processes and could be correlated with ADI-MS experiments. Gas temperature and He_m number density measurements can be made using a single technique: diode laser absorption spectroscopy. Previously, measurements of He_m distributions in APPJs have been made using diode laser absorption spectroscopy. Currently, progress is being made in the Farnsworth lab to make such measurements for our ADI source. Collaborative efforts that would allow my colleagues to make He_m absorption measurements on DART, FAPA and LTP sources are being arranged.

5.2.6 Negative Ion APPJ-MS

The detection of explosives has been a major application for ADI-MS.[1, 2, 8-17] Detection of various explosives-related compounds has been accomplished with several electrical discharge-based sources.[2, 8, 12, 13, 15, 17] In each case, detection was accomplished in the negative ion mode.

Detection in the negative ion mode with DART and LTP reveals that negatively charged analyte species are being formed by the following APCI-related processes:[1, 15, 17]

Electron capture (EC)

$$M + e^- \rightarrow M^- \quad 5.1$$

Dissociative electron capture (dissociative EC)

$$M + e^- \rightarrow [M - X]^- + X \quad 5.2$$

Proton transfer

$$M + O_2^- \rightarrow [M - H]^- + HO_2 \quad 5.3$$

Anion attachment

$$M + X^- \rightarrow MX^- \quad 5.4$$

In working with the APPJ, it is anticipated that the mass spectra that are collected in the negative ion mode will be indicative of the same ionization mechanisms. In the case of explosives, the oxidation of aromatic hydrocarbons is an undesired mechanism that dominates negative ion spectra. For the FAPA, the oxidation reaction is said to be generated from atmospheric oxygen mixing with the plasma.[2] However, no report of unwanted oxidation is given when detecting explosives via LTP-MS, despite the significant interaction between the plasma jet and the air.[17] How this mechanism has been avoided by some ionization sources remains a question that needs to be addressed.

Improvements have been made in the detection of explosives by reactive-LTP. In that work, trifluoroacetic acid vapor was added to the carrier gas to affect the ionization and improve detection of several explosive compounds.[17] In work by Zhang et al., the anionic adduction of chlorine was observed when HCl was used in the solvent matrix.[15] Similarly, it would be interesting to test the effect that HCl vapor would have on detection in the negative ion mode.

The effects of the vapor on plasma conditions and ionization mechanisms would be studied using spectroscopic and mass spectrometric measurements and observations.

5.3 Conclusions

In recent months, several studies have been published that have contributed to a better understanding of potential mechanisms that lead to ionization when using plasma-based ADI sources.[3, 18, 19] However, not everything about the ionization process is understood. Research should continue that would allow for a full understanding of desorption and ionization processes. While future research will continue to improve understanding about desorption and ionization processes, it will also contribute to the development and improvement of ADI sources. Spectroscopic methods, including LIF, are reliable tools that can aid in the understanding of these processes. Spectroscopic methods are also useful for characterizing and comparing electrical discharge-based ADI sources. Fundamental studies will play a critical role in the growth of the field of ADI-MS as it becomes a useful analytical tool.

5.4 References

1. Song, L.; Dykstra, A. B.; Yao, H.; Bartmess, J. E., Ionization Mechanism of Negative Ion-Direct Analysis in Real Time: A Comparative Study with Negative Ion-Atmospheric Pressure Photoionization. *J. Am. Soc. Mass Spectr.* **2009,** *20* (1), 42-50.
2. Shelley, J. T.; Wiley, J. S.; Hieftje, G. M., Ultrasensitive Ambient Mass Spectrometric Analysis with a Pin-to-Capillary Flowing Atmospheric-Pressure Afterglow Source. *Anal. Chem.* **2011,** *83* (14), 5741-5748.
3. Heywood, M. S.; Taylor, N.; Farnsworth, P. B., Measurement of Helium Metastable Atom Densities in a Plasma-Based Ambient Ionization Source. *Anal. Chem.* **2011,** *83* (17), 6493-6499.
4. Xiong, Q.; Lu, X.; Liu, J.; Xian, Y.; Xiong, Z.; Zou, F.; Zou, C.; Gong, W.; Hu, J.; Chen, K.; Pei, X.; Jiang, Z.; Pan, Y., Temporal and Spatial Resolved Optical Emission Behaviors of a Cold Atmospheric Pressure Plasma Jet. *J. Appl. Phys.* **2009,** *106* (8), 083302-6.
5. Urabe, K.; Morita, T.; Tachibana, K.; Ganguly, B. N., Investigation of Discharge Mechanisms in Helium Plasma Jet at Atmospheric Pressure by Laser Spectroscopic Measurements. *J. Phys. Appl. Phys.* **2010,** *43* (9), 095201.

6. Olenici-Craciunescu, S. B.; Muller, S.; Michels, A.; Horvatic, V.; Vadla, C.; Franzke, J., Spatially Resolved Spectroscopic Measurements of a Dielectric Barrier Discharge Plasma Jet Applicable for Soft Ionization. *Spectrochim. Acta B* **2011,** *66* (3-4), 268-273.
7. Wang, H.; Sun, W. J.; Zhang, J. S.; Yang, X. H.; Lin, T.; Ding, L., Desorption Corona Beam Ionization Source for Mass Spectrometry. *Analyst* **2010,** *135* (4), 688-695.
8. Cody, R. B.; Laramee, J. A.; Durst, H. D., Versatile New Ion Source for the Analysis of Materials in Open Air under Ambient Conditions. *Anal. Chem.* **2005,** *77* (8), 2297-2302.
9. Popov, I. A.; Chen, H.; Kharybin, O. N.; Nikolaev, E. N.; Cooks, R. G., Detection of Explosives on Solid Surfaces by Thermal Desorption and Ambient Ion/Molecule Reactions. *Chem. Commun.* **2005**, 1953-1955.
10. Takáts, Z.; Cotte-Rodriguez, I.; Talaty, N.; Chen, H.; Cooks, R. G., Direct, Trace Level Detection of Explosives on Ambient Surfacaes by Desorption Electrospray Ionization Mass Spectrometry. *Chem. Commun.* **2005**, 1950-1952.
11. Cotte-Rodríguez, I.; Cooks, R. G., Non-Proximate Detection of Explosives Ande Chemical Warfare Agent Simulants by Desorption Electrospray Ionization Mass Spectrometry. *Chem. Commun.* **2006**, 2968-2970.
12. Song, Y.; Cooks, R. G., Atmospheric Pressure Ion/Molecule Reactions for the Selective Detection of Nitroaromatic Explosives Using Acetonitrile and Air as Reagents. *Rapid Commun. Mass Sp.* **2006,** *20* (20), 3130-3138.
13. Na, N.; Zhang, C.; Zhao, M.; Zhang, S.; Yang, C.; Fang, X.; Zhang, X., Direct Detection of Explosives on Solid Surfaces by Mass Spectrometry with an Ambient Ion Source Based on Dielectric Barrier Discharge. John Wiley & Sons, Ltd.: 2007; Vol. 42, pp 1079-1085.
14. Cotte-Rodriguez, I.; Hernandez-Soto, H.; Chen, H.; Cooks, R. G., In Situ Trace Detection of Peroxide Explosives by Desorption Electrospray Ionization and Desorption Atmospheric Pressure Chemical Ionization. *Anal. Chem.* **2008,** *80* (5), 1512-1519.
15. Zhang, Y.; Ma, X.; Zhang, S.; Yang, C.; Ouyang, Z.; Zhang, X., Direct Detection of Explosives on Solid Surfaces by Low Temperature Plasma Desorption Mass Spectrometry. *Analyst* **2009,** *134* (1), 176-181.
16. Gu, H. W.; Yang, S. P.; Li, J. Q.; Hu, B.; Chen, H. W.; Zhang, L. L.; Fei, Q., Geometry-Independent Neutral Desorption Device for the Sensitive Eesi-MS Detection of Explosives on Various Surfaces. *Analyst* **2010,** *135* (4), 779-788.
17. Garcia-Reyes, J. F.; Harper, J. D.; Salazar, G. A.; Charipar, N. A.; Ouyang, Z.; Cooks, R. G., Detection of Explosives and Related Compounds by Low-Temperature Plasma Ambient Ionization Mass Spectrometry. *Anal. Chem.* **2011,** *83* (3), 1084-1092.
18. Chan, G. C. Y.; Shelley, J. T.; Wiley, J. S.; Engelhard, C.; Jackson, A. U.; Cooks, R. G.; Hieftje, G. M., Elucidation of Reaction Mechanisms Responsible for Afterglow and Reagent-Ion Formation in the Low-Temperature Plasma Probe Ambient Ionization Source. *Anal. Chem.* **2011,** *83* (10), 3675-3686.
19. Shelley, J.; Chan, G.; Hieftje, G., Understanding the Flowing Atmospheric-Pressure Afterglow (Fapa) Ambient Ionization Source through Optical Means. *J. Am. Soc. Mass Spectr.* **2012,** *23* (2), 407-417.

6 Appendix

6.1 Processing Spectral Images with Matlab

6.1.1 Conversion of .SPE Files to .TXT Files

Click on the Tools tab in the WinView/32 software. Select the Convert to ASCII option. The box in Figure A.1 will appear. You may choose an image from an active window or choose any number of files to convert. Choose the output directory. Set the file extension to txt. Set the delimiter to comma. For output file options, select one file per frame. This setting allows you to convert a single fluorescence image to a single .txt file. It also separates the multi-frame emission images (31 frames per acquisition for the current work) and creates a single .txt file for each frame. Choose multiple columns (no header). Convert to ASCII.

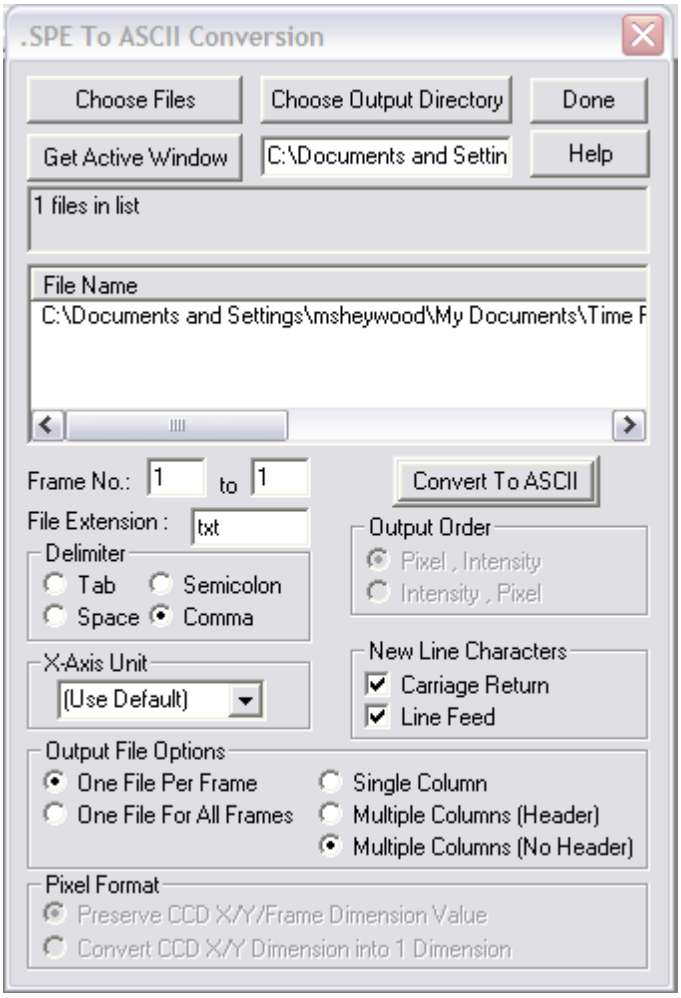

Figure 6.1: Dialog box and options for .SPE to ASCII file conversion.

This should produce a 512 x 513 array. The first column provides the number for each row. Each subsequent number is a value for the intensity for each pixel in the CCD.

6.1.2 .TXT File Processing in Matlab

The code for converting these txt files into axial profiles is shown below. The code works if emission and fluorescence images were saved with the same general name with only a change in number to specify a temporal delay. For example, helium metastable files were saved as HeMetaPosx_1.txt, where x was 0-30 for the 31 temporal positions across the waveform.

6.1.2.1 Temporally-Resolved Spectral Images to Time-Averaged Profiles

```
clean;
maxFiles = 31; %Enter 31 for this directory%
k = 0;

maxFiles = maxFiles - 1;

x = 1:512;
X = (x'-180).*.025./0.35;   %converts pixels to mm from tip of capillary%
X2 = (x'-162).*.025./0.35;

SFCHeM = zeros(512,1);      %variables used to accumulate summed profiles%
SFCNIE = zeros(512,1);
SFCHeE = zeros(512,1);
SFCNIF = zeros(512,1);
SFCNN = zeros(512,1);
SFCO = zeros(512,1);
SFCH = zeros(512,1);
SFCHHHe = zeros(512,1);
SFCHHO = zeros(512,1);
SFCHHH = zeros(512,1);
SFCHHNN = zeros(512,1);
SFCHHNIE = zeros(512,1);

for j=0:maxFiles                          %for loop 30 times%
HeMfileHeader = 'HeMetaPos';               %He metastable file extraction%
HMfilename =strcat(HeMfileHeader, num2str(k), '_1.txt');
HMD = importdata(HMfilename);               %import data%
HMD(:,1) = [];                              %blank out first row%
CutHMD = HMD(:,240:255);                    %Select number of rows ie:16%
TCutHMD = CutHMD';                          %Transpose before summing%
SCutHMD = sum(TCutHMD);                     %Sum selected rows%
CHeM = SCutHMD';                            %Transpose summed data%
SFCHeM = SFCHeM + CHeM;                     %Sum profile for 30 frames%

NIFfileHeader = 'NI FLUOR 427 nm'; %Nitrogen ion fluorescence file
extraction%
NIFfilename = strcat(NIFfileHeader, num2str(k), '_1.txt');
NIFD = importdata(NIFfilename);
NIFD(:,1) = [];
CutNIFD = NIFD(:,262:285);
TCutNIFD = CutNIFD';
SCutNIFD = sum(TCutNIFD);
CNIF = SCutNIFD';                           %Fluorescence measurements are%
SFCNIF = SFCNIF + CNIF;                     %background subtracted%

NNfileHeader = '31 frames of N2 357 nm Emission';  %Neutral Nitrogen Emission
file extraction
```

```
NNfilename =strcat(NNfileHeader, num2str(k+1), '_1.txt');
NND = importdata(NNfilename);
NND(:,1) = [];
CutNND = NND(:,240:252);
TCutNND = CutNND';
SCutNND = sum(TCutNND);
CNN = SCutNND'-4377;                          %Emission data need to be%
SFCNN = SFCNN + CNN;                          %background subtracted%

NIEfileHeader = 'NI 427 Emission Pos';  %Nitrogen ion emission file
extraction%
NIEfilename = strcat(NIEfileHeader, num2str(k), '_1.txt');
NIED = importdata(NIEfilename);
NIED(:,1) = [];
CutNIED = NIED(:,232:247);
TCutNIED = CutNIED';
SCutNIED = sum(CutNIED');
CNIE = SCutNIED'-5686;
SFCNIE = SFCNIE + CNIE;

HeEfileHeader = 'He 706 Emission Pos';       %He emission file extraction%
HEfilename = strcat(HeEfileHeader, num2str(k), '_1.txt');
HED = importdata(HEfilename);
HED(:,1) = [];
CutHED = HED(:,235:250);
TCutHED = CutHED';
SCutHED = sum(CutHED');
CHeE = SCutHED'-9224;
SFCHeE = SFCHeE + CHeE;

HfileHeader = '31 frames of H 656 nm Emission';     %Hydrogen emission file
extraction%
Hfilename =strcat(HfileHeader, num2str(k+1), '_1.txt');
HD = importdata(Hfilename);
HD(:,1) = [];
CutHD = HD(:,268:276);
TCutHD = CutHD';
SCutHD = sum(CutHD');
CH = (SCutHD'-5169);
SFCH = SFCH + CH;

OfileHeader = '31 frames of O 777 nm Emission';     %Oxygen emission file
extraction%
Ofilename =strcat(OfileHeader, num2str(k+1), '_1.txt');
OD = importdata(Ofilename);
OD(:,1) = [];
CutOD = OD(:,252:262);
TCutOD = CutOD';
SCutOD = sum(CutOD');
CO = (SCutOD'-1227);
SFCO = SFCO + CO;

HHHefileHeader = 'Helium 706 nm Emission HeH2 Plasma';  %Hydrogen emission in
He/H plasma file extraction%
HHHefilename =strcat(HHHefileHeader, num2str(k+1), '_1.txt');
HHHeD = importdata(HHHefilename);
```

```
HHHeD(:,1) = [];
CutHHHeD = HHHeD(:,225:240);
TCutHHHeD = CutHHHeD';
SCutHHHeD = sum(CutHHHeD');
CHHHe = (SCutHHHeD'-9490);
SFCHHHe = SFCHHHe + CHHHe;

HHNNfileHeader = 'Nitrogen 357 nm Emission HeH2 Plasma';
HHNNfilename =strcat(HHNNfileHeader, num2str(k+1), '_1.txt');
HHNND = importdata(HHNNfilename);
HHNND(:,1) = [];
CutHHNND = HHNND(:,234:248);
TCutHHNND = CutHHNND';
SCutHHNND = sum(CutHHNND');
CHHNN = (SCutHHNND'-5308);
SFCHHNN = SFCHHNN + CHHNN;

HHHfileHeader = 'Hydrogen 656 nm Emission HeH2 Plasma';
HHHfilename =strcat(HHHfileHeader, num2str(k+1), '_1.txt');
HHHD = importdata(HHHfilename);
HHHD(:,1) = [];
CutHHHD = HHHD(:,260:270);
TCutHHHD = CutHHHD';
SCutHHHD = sum(CutHHHD');
CHHH = (SCutHHHD'-6420);
SFCHHH = SFCHHH + CHHH;

HHOfileHeader = 'Oxygen 777 nm Emission HeH2 Plasma';
HHOfilename =strcat(HHOfileHeader, num2str(k+1), '_1.txt');
HHOD = importdata(HHOfilename);
HHOD(:,1) = [];
CutHHOD = HHOD(:,248:255);
TCutHHOD = CutHHOD';
SCutHHOD = sum(CutHHOD');
CHHO = (SCutHHOD'-970);
SFCHHO = SFCHHO + CHHO;

HHNIEfileHeader = 'Nitrogen Ion 391 nm Emission HeH2 Plasma';
HHNIEfilename = strcat(HHNIEfileHeader, num2str(k+1), '_1.txt');
HHNIED = importdata(HHNIEfilename);
HHNIED(:,1) = [];
CutHHNIED = HHNIED(:,269:284);
TCutHHNIED = CutHHNIED';
SCutHHNIED = sum(CutHHNIED');
CHHNIE = (SCutHHNIED'-9416);
SFCHHNIE = SFCHHNIE + CHHNIE;

k = k+1;
end
load chirp                              %Lets me know when it is done%
Sound (y, Fs)

NSFCHeM = SFCHeM/max(SFCHeM);           %Profiles are normalized%
NSFCNIE = SFCNIE/max(SFCNIE);
NSFCHeE = 4*SFCHeE/max(SFCHeE);
NSFCNIF = SFCNIF/max(SFCNIF);
```

```
NSFCNN = SFCNN/max(SFCNN);
NSFCO = SFCO/max(SFCO);
NSFCH = SFCH/max(SFCH);
NSFCHHHe = SFCHHHe/max(SFCHHHe);
NSFCHHO = SFCHHO/max(SFCHHO);
NSFCHHH = SFCHHH/max(SFCHHH);
NSFCHHNN = SFCHHNN/max(SFCHHNN);
NSFCHHNIE = SFCHHNIE/max(SFCHHNIE);

plot(X,SFCNIE,X,SFCNN,'linewidth',2)        %Plot time averaged profiles%
legend('FontName','Times New Roman','FontSize',12);
hleg = legend('NI (427 nm)','Nitrogen (357 nm)');
xlabel('Distance from Capillary Tip (mm)','FontSize',24,'FontName','Times New
Roman');
ylabel('Normalized Signal','FontSize',24,'FontName','Times New Roman');
set(gca,'FontName','Times New Roman','FontSize',18);
axis([-10 23 0 Max(SFCNN)]);
```

6.1.2.2 Temporally-Resolved Spectral Images to Axial Profile Motion Picture

This code converts multiple spectral images into axial profile plots, turns them into individual frames and creates a motion picture.

```
clean;
maxFiles = 31;                              %Enter 31 for this directory%
k = 0;

maxFiles = maxFiles - 1;

x = 1:512;
X = (x'-178).*.025./0.35;                    %mm from tip of capillary%
X2 = (x'-162).*.025./0.35;

for j=0:maxFiles
HHHefileHeader = 'Helium 706 nm Emission HeH2 Plasma';
HHHefilename =strcat(HHHefileHeader, num2str(k+1), '_1.txt');
HHHeD = importdata(HHHefilename);
HHHeD(:,1) = [];
CutHHHeD = HHHeD(:,225:240);
TCutHHHeD = CutHHHeD';
SCutHHHeD = sum(CutHHHeD');
CHHHe = (SCutHHHeD'-9490)./371307;

HHNNfileHeader = 'Nitrogen 357 nm Emission HeH2 Plasma';
HHNNfilename =strcat(HHNNfileHeader, num2str(k+1), '_1.txt');
HHNND = importdata(HHNNfilename);
HHNND(:,1) = [];
CutHHNND = HHNND(:,234:248);
TCutHHNND = CutHHNND';
SCutHHNND = sum(CutHHNND');
CHHNN = (SCutHHNND'-5308)./93584;

HHHfileHeader = 'Hydrogen 656 nm Emission HeH2 Plasma';
HHHfilename =strcat(HHHfileHeader, num2str(k+1), '_1.txt');
```

```
HHHD = importdata(HHHfilename);
HHHD(:,1) = [];
CutHHHD = HHHD(:,260:270);
TCutHHHD = CutHHHD';
SCutHHHD = sum(CutHHHD');
CHHH = (SCutHHHD'-6420)./68632;

HHOfileHeader = 'Oxygen 777 nm Emission HeH2 Plasma';
HHOfilename =strcat(HHOfileHeader, num2str(k+1), '_1.txt');
HHOD = importdata(HHOfilename);
HHOD(:,1) = [];
CutHHOD = HHOD(:,248:255);
TCutHHOD = CutHHOD';
SCutHHOD = sum(CutHHOD');
CHHO = (SCutHHOD'-970)./3634;

HHNIEfileHeader = 'Nitrogen Ion 391 nm Emission HeH2 Plasma';
HHNIEfilename = strcat(HHNIEfileHeader, num2str(k+1), '_1.txt');
HHNIED = importdata(HHNIEfilename);
HHNIED(:,1) = [];
CutHHNIED = HHNIED(:,269:284);
TCutHHNIED = CutHHNIED';
SCutHHNIED = sum(CutHHNIED');
CHHNIE = (SCutHHNIED'-9416)./806083;

HeMfileHeader = 'HeMetaPos';          %He metastable file extraction%
HMfilename =strcat(HeMfileHeader, num2str(k), '_1.txt');
HMD = importdata(HMfilename);
HMD(:,1) = [];
CutHMD = HMD(:,240:255);
TCutHMD = CutHMD';
SCutHMD = sum(CutHMD');
CHeM = SCutHMD'./78764;

NNfileHeader = '31 frames of N2 357 nm Emission';
NNfilename =strcat(NNfileHeader, num2str(k+1), '_1.txt');
NND = importdata(NNfilename);
NND(:,1) = [];
CutNND = NND(:,248:253);
TCutNND = CutNND';
SCutNND = sum(CutNND');
CNN = 5.*(SCutNND'-4377)./(3.*836868);

HfileHeader = '31 frames of H 656 nm Emission';
Hfilename =strcat(HfileHeader, num2str(k+1), '_1.txt');
HD = importdata(Hfilename);
HD(:,1) = [];
CutHD = HD(:,268:276);
TCutHD = CutHD';
SCutHD = sum(CutHD');
CH = (SCutHD'-5169);

OfileHeader = '31 frames of O 777 nm Emission';
Ofilename =strcat(OfileHeader, num2str(k+1), '_1.txt');
OD = importdata(Ofilename);
OD(:,1) = [];
```

```
CutOD = OD(:,252:262);
TCutOD = CutOD';
SCutOD = sum(CutOD');
CO = (SCutOD'-1227)./26013;

NIFfileHeader = 'NI FLUOR 427 nm'; %Nitrogen ion fluorescence file
extraction%
NIFfilename = strcat(NIFfileHeader, num2str(k), '_1.txt');
NIFD = importdata(NIFfilename);
NIFD(:,1) = [];
CutNIFD = NIFD(:,262:285);
TCutNIFD = CutNIFD';
SCutNIFD = sum(CutNIFD');
CNIF = SCutNIFD'./45600 ;   %fluorescence measurements need no background
                            %subtraction because they have already had an
                            %off resonance background subtracted from them.
NIBGfileHeader = 'NI BGE Pos';                    %Nitrogen ion fluorescence
file extraction%
NIBGfilename = strcat(NIBGfileHeader, num2str(k), '_1.txt');
NIBGD = importdata(NIBGfilename);
NIBGD(:,1) = [];
CutNIBGD = NIBGD(:,262:285);
TCutNIBGD = CutNIBGD';
SCutNIBGD = sum(TCutNIBGD);
CNIBG = (SCutNIBGD'-3001);     %./33878

NIEfileHeader = 'NI 427 Emission Pos';   %Nitrogen ion emission file
extraction%
NIEfilename = strcat(NIEfileHeader, num2str(k), '_1.txt');
NIED = importdata(NIEfilename);
NIED(:,1) = [];
CutNIED = NIED(:,232:247);
TCutNIED = CutNIED';
SCutNIED = sum(CutNIED');
CNIE = (SCutNIED'-5686)./836868;

HeEfileHeader = 'He 706 Emission Pos';     %He emission file extraction%
HEfilename = strcat(HeEfileHeader, num2str(k), '_1.txt');
HED = importdata(HEfilename);
HED(:,1) = [];
CutHED = HED(:,235:250);
TCutHED = CutHED';
SCutHED = sum(CutHED');
CHeE = (SCutHED'-9224)./505677;

plot(X,CNIE,X,CNN,'Linewidth',2)        %Plot single frame profiles%
axis([-10 23 0 1]);
%hleg = legend('Excited Oxygen (777 nm)','Nitrogen Ion (427 nm)','Helium
Metastables (706 nm)');
xlabel('Distance from Capillary Tip (mm)','Fontsize',24,'FontName','Times New
Roman');
ylabel('Normalized Intensity','Fontsize',24,'FontName','Times New Roman');
set(gca,'FontSize',24,'FontName','Times New Roman','box','off');
%,'YTickLabel',''
Savename = strcat('Fluorescence Movie Frame', num2str(k));
%saveas(figure(1),Savename,'jpeg');
```

```
k = k+1;
H(k) = getframe; %gets the plotted profile and makes it a frame for Movie
(H)%

end
load gong
sound(y, Fs)       %means the movie is done%
movie(H,5)          %You can also control the speed of the movie.%
                    %An example: movie(M,5,3) will play the movie 5 times at 3
                    frames a sec.)%
```

6.1.2.3 Temporally-Resolved Radial Nitrogen Ion Fluorescence

```
clean;
maxFiles = 31; %Enter 31 for this directory%
k = 0;

maxFiles = maxFiles - 1;

x = 1:512;
X = (x'-261)./126;                  %Radial distance in mm
X2 = (x'-245)./126;                 %This variable accounts for the 200 micron
shift between .5 and 5 mm.
SFCRNIF5 = zeros(512,1);            %This shift is due to a 2.54 degree tilt
in the plasma which is negligible and within the range of the 600 micron
plasma.
SFCRNIFH = zeros(512,1);            % For the whole length of the plasma there
is a discrepancy of 1 mm drift from 0 to 23 mm.

for j=0:maxFiles

RNIF5fileHeader = '5 mm Fluorescence 427 nm';
RNIF5filename = strcat(RNIF5fileHeader, num2str(k), '_1.txt');
RNIF5D = importdata(RNIF5filename);
RNIF5D(:,1) = [];
CutRNIF5 = RNIF5D(:,228:243);
TCutRNIF5 = CutRNIF5';
SCutRNIF5 = sum(TCutRNIF5);
CRNIF5 = (SCutRNIF5')./24601;
SFCRNIF5 = SFCRNIF5 + CRNIF5;

RNIFHfileHeader = 'Half mm Fluorescence 427 nm';
RNIFHfilename = strcat(RNIFHfileHeader, num2str(k), '_1.txt');
HED = importdata(RNIFHfilename);
HED(:,1) = [];
CutHED = HED(:,235:250);
TCutHED = CutHED';
SCutHED = sum(CutHED');
CRNIFH = (SCutHED')./24601;
SFCRNIFH = SFCRNIFH + CRNIFH;
```

```
plot(X,CRNIF5,X2,CRNIFH,'Linewidth',2)
axis([-1 1 0 1]);
hleg = legend('5 mm','0.5 mm');
xlabel('Radail Distance (mm)','Fontsize',24,'FontName','Times New Roman');
ylabel('Normalized Intensity','Fontsize',24,'FontName','Times New Roman');
set(gca,'FontSize',24,'FontName','Times New Roman','box','off');
Savename = strcat('Fluorescence Movie Frame', num2str(k));
%saveas(figure(1),Savename,'jpeg');

k = k+1;
H(k) = getframe;     %Makes the time resolved movie (H)%

end
load gong
sound(y, Fs)  %means the movie is done%
movie(H,5)    %You can also control the speed of the movie.%
              %An example: movie(M,5,3) will play the movie 5 times at 3
frames a sec.)%

NSFCRNIF5 = SFCRNIF5/max(SFCRNIF5); %Normalized, time-averaged nitrogen ion
NSFCRNIFH = SFCRNIFH/max(SFCRNIF5); %distributions%
%Plots the normalized, time-averaged radial nitrogen ion distributions%
plot(X,NSFCRNIF5,X2,NSFCRNIFH,'linewidth',2)
legend('FontName','Times New Roman','FontSize',12);
hleg = legend('5 mm','0.5 mm');
xlabel('Radial Distance (mm)','FontSize',24,'FontName','Times New Roman');
ylabel('Normalized Signal','FontSize',24,'FontName','Times New Roman');
set(gca,'FontName','Times New Roman','FontSize',18);
axis([-1 1 0 1]);
```